Global Estimation of Precipitation Using Opaque Microwave Bands

by

Frederick Wey-Min Chen

S.B. Electrical Science and Engineering
Massachusetts Institute of Technology (1998)
M.Eng. Electrical Engineering and Computer Science
Massachusetts Institute of Technology (1998)

Submitted to the Department of Electrical Engineering and Computer Science
in partial fulfillment of the requirements for the degree of

Doctor of Philosophy in Electrical Engineering

at the

MASSACHUSETTS INSTITUTE OF TECHNOLOGY

June 2004

Author .....
Department of Electrical Engineering and Computer Science
May 20, 2004

Certified by .....
David H. Staelin
Professor of Electrical Engineering
Thesis Supervisor

Accepted by .....
Arthur C. Smith
Chairman, Department Committee on Graduate Students

Global Estimation of Precipitation Using Opaque Microwave Bands

by

Frederick Wey-Min Chen

Submitted to the Department of Electrical Engineering and Computer Science
on May 20, 2004, in partial fulfillment of the
requirements for the degree of
Doctor of Philosophy in Electrical Engineering

Abstract

This thesis describes the use of opaque microwave bands for global estimation of precipitation rate. An algorithm was developed for estimating instantaneous precipitation rate for the Advanced Microwave Sounding Unit (AMSU) on the NOAA-15, NOAA-16, and NOAA-17 satellites, and the Advanced Microwave Sounding Unit and Humidity Sounder for Brazil (AMSU/HSB) aboard the NASA Aqua satellite. The algorithm relies primarily on channels in the opaque 54-GHz oxygen and 183-GHz water vapor resonance bands. Many methods for estimating precipitation rate using surface-sensitive microwave window channels have been developed by others.

The algorithm involves a set of signal processing components whose outputs are fed into a neural net to produce a rain rate estimate for each 15-km spot. The signal processing components utilize techniques such as principal component analysis for characterizing groups of channels, spatial filtering for cloud-clearing brightness temperature images, and data fusion for sharpening images in order to optimize sensing of small precipitation cells. An effort has been made to make the algorithm as blind to surface variations as possible.

The algorithm was trained using data over the eastern U.S. from the NEXRAD ground-based radar network, and was validated through numerical comparisons with NEXRAD data and visual examination of the morphology of precipitation from over the eastern U.S. and around the world. It performed reasonably well over the eastern U.S. and showed potential for detecting and estimating falling snow. However, it tended to overestimate rain rate in summer Arctic climates.

Adjustments to the algorithm were made by developing a neural-net-based estimator for estimating a multiplicative correction factor based on data from the Advanced Microwave Sounding Radiometer for the Earth Observing System (AMSR-E) on the Aqua satellite. The correction improved estimates in the Arctic to more reasonable levels. The final estimator was a hybrid of the NEXRAD-trained estimator and the AMSR-E-corrected estimator.

Climatological metrics were computed over one year during which all AMSU-A/B instruments on NOAA-15, NOAA-16, and NOAA-17 were working. Annual mean

rain rates appear to agree morphologically with those from the Global Precipitation Climatology Project. Maps of precipitation frequencies and the diurnal variations of precipitation rate were produced.

Thesis Supervisor: David H. Staelin
Title: Professor of Electrical Engineering

Acknowledgments

I would like to thank Prof. David H. Staelin for giving me the privilege of working on global estimation of precipitation and for his guidance. I am grateful for the many professional opportunities he has given me such as working as part of the Aqua Mission Team.

Several people have helped me by providing data. I thank Steve P.L. Maloney, Charles Lebell, and Marilyn M. Wolfson (Lincoln Laboratory) for providing me with NEXRAD precipitation data, Michael Chalfant (NOAA) for providing me with several years of AMSU-A/B data from the NOAA-15, NOAA-16, and NOAA-17 satellites, and Walter Wolf (NOAA) for providing me with several months of AMSU/HSB data from the NASA Aqua satellite.

I would like to thank the people of the Remote Sensing and Estimation Group (RSEG) for helpful discussions and an enjoyable working environment. Specifically, I would like to thank Antonio Fuentes-Loyola for his contribution to the precipitation estimation research during its early stages and Amanda Leckman for her assistance with studies on midlatitude snow and polar precipitation. I also thank Seth Hall for faithfully and reliably maintaining the RSEG computers and addressing our growing computational needs.

I would like to thank my parents, Shih-Yew and Mei-Ying Chen, and my brother, Michael, for their unconditional love and generous support.

I would like to thank my grandparents, Wang Chih-Hsiang and Wang Yue-Hua, for generously blessing me throughout my life from many thousand of miles away.

I would like to thank the many brothers and sisters in Christ at the Chinese Bible Church of Greater Boston for their encouragement and guidance as I have gone through the past 11 years at MIT.

I thank my Lord and Savior Jesus Christ for His faithfulness as I have gone through graduate school. I also thank Him for helping me to see research as not merely an intellectual exercise but also a devotional experience. I have seen His wisdom and glory in 54-GHz and 183-GHz brightness temperature images.

AMSR-E data and images are produced by Remote Sensing Systems, Santa Rosa, CA, and sponsored by NASA's Earth Science Enterprise (ESE).

This research was supported by the National Aeronautics and Space Administration under Grant NAG5-7487, Grant NAG5-13652, Grant NAG5-11390, and Contract NAS5-31376.

Permission has been granted by the IEEE to include content from the following papers:

- F.W. Chen and D.H. Staelin, "AIRS/AMSU/HSB Precipitation Estimates," *IEEE Transactions on Geoscience and Remote Sensing*, vol. 41, no. 2, pp. 410-417, Feb. 2003.

- F.W. Chen, A.M. Leckman, and D.H. Staelin, "Passive Microwave Signatures of Arctic Snowstorms Observed from Satellites," *Proceedings of the 2003 IEEE International Geoscience and Remote Sensing Symposium*, vol. 5, pp. 3139-3141, July 2003.

And God said, "Let there be light," and there was light. God saw that the light was good.

Genesis 1:3-4a[1]

Who cuts a channel for the torrents of rain,
and a path for the thunderstorm,
to water a land where no man lives,
a desert with no one in it,
to satisfy a desolate wasteland
and make it sprout with grass?

Job 38:25-27[1]

[1]Scripture taken from the HOLY BIBLE, NEW INTERNATIONAL VERSION. ©1973, 1978, 1984 by International Bible Society. Used by permission of Zondervan. All rights reserved.

Contents

1 Introduction **21**

1.1 Problem Statement 21

1.1.1 Precipitation-Rate Retrievals 22

1.1.2 Precipitation Climatology 23

1.2 Thesis Outline 23

2 Physical Basis of Passive Microwave Remote Sensing of Precipitation 25

2.1 Thermal Radiation and Radiative Transfer 25

2.2 Passive Microwave Remote Sensing of the Atmosphere 30

2.2.1 Temperature and Water Vapor Profiles 30

2.2.2 Clouds and Precipitation 32

2.3 Description of the Relevant Instruments 36

2.3.1 AMSU on the NOAA-15, NOAA-16, and NOAA-17 Satellites . 36

2.3.2 AMSU/HSB on the Aqua Satellite 38

3 Signal Processing and Estimation Techniques **41**

3.1 Principal Component Analysis (PCA) 41

3.1.1 Basic PCA 42

3.1.2 Constrained PCA 43

3.2 Neural Nets 44

3.2.1 Structure of Neural Net 44

3.2.2 Training Neural Nets 47

3.3 Data Fusion 47

4 The Precipitation Retrieval Algorithm **49**

4.1 Structure of the Algorithm 49

4.2 Signal Processing Components 50

4.2.1 Limb-and-Surface Corrections 50

4.2.2 Precipitation Detection 54

4.2.3 Cloud Clearing by Regional Laplacian Interpolation 57

4.2.4 Temperature-Profile and Water-Vapor-Profile Principal Components 62

4.2.5 Image Sharpening 63

4.3 Development of the Algorithm 65

4.4 Retrieval Performance Evaluation 68

4.4.1 Image Comparisons of NEXRAD and AMSU/HSB 69

4.4.2 Numerical Comparisons of NEXRAD and AMSU/HSB Retrievals 71

4.4.3 Global Retrievals of Rain and Snow 74

4.5 Post-Development Changes to the Algorithm 75

5 Snow and Polar Precipitation **77**

5.1 Examples of Polar Precipitation 78

5.1.1 Example 1 78

5.1.2 Example 2 78

5.1.3 Example 3 79

5.2 Weaknesses of the Algorithm 80

6 Precipitation Climatology **85**

6.1 Climatology-Based Correction of the Algorithm 85

6.2 Precipitation Means and Frequencies 92

6.3 Diurnal Cycle 98

7 Conclusions **107**

7.1 Summary of the Thesis 107

7.1.1 Main Contributions 108

7.1.2 Secondary Contributions 108
7.2 Future Work 109
7.2.1 Minor Improvements to the Algorithm 109
7.2.2 Major Improvements to the Algorithm 110
7.2.3 Future Studies 111

A Improved Cloud-Clearing at Image Corners **113**

List of Figures

2-1 The major components of the radiative transfer equation (NOTE: $\theta \neq \phi$ since the surface of the earth is spherical) 26

2-2 Zenith opacity for the microwave spectrum 31

2-3 Weighting functions of AMSU-A and AMSU-B channels 31

2-4 Mie scattering coefficients for 54 GHz and 183.31 GHz at a temperature of $-55°$ C 34

2-5 Orbital patterns of the NOAA-15, NOAA-16, NOAA-17, and Aqua satellites 38

2-6 Scan patterns of (a) Aqua AMSU/HSB and (b) AMSU-A/B on NOAA-15, NOAA-16, and NOAA-17. AMSU and AMSU-A spots are labeled with blue +'s and HSB and AMSU-B spots with red dots 39

3-1 The structure of a perceptron 44

3-2 A 2-layer feedforward neural net with one output node 45

3-3 Neural net transfer functions 46

4-1 Basic structure of the algorithm 50

4-2 Block diagram of the algorithm, part 1 51

4-3 Block diagram of the algorithm, part 2 51

4-4 NOAA-15 AMSU-A 54.4-GHz brightness temperatures for a northbound track on 13 Sept 2000. (a) Uncorrected, and (b) Limb-and-surface corrected 53

4-5 NOAA-15 AMSU-B brightness temperatures for northbound tracks on 13 Sept 2000 at (a) 150 GHz, and (b) 183 ± 7 GHz 56

4-6 NOAA-15 AMSU-B 183±7-GHz brightness temperatures, 20 Jan 2000, 1339 to 1349 UTC 57

4-7 NOAA-15 AMSU-B 183 ± 1-GHz brightness temperatures over a dry hole on 14 Feb 2002, 0754 UTC (left), and 15 Feb 2002, 0731 UTC (right) 58

4-8 NOAA-15 AMSU-A 52.8-GHz brightness temperatures for a northbound track on 13 Sept 2000 (a) before cloud-clearing, and (b) after cloud-clearing using Laplacian interpolation. AMSU-A pixels within potentially precipitating regions are marked with x's. 59

4-9 Types of regions encountered by the cloud clearing method. Boundary pixels are shaded in red. 60

4-10 Salvaging pixels in a complete-edge region. Eliminating the bottom two rows of the image on the left leaves a portion that can be treated as an edge region. 62

4-11 Frontal system on 13 Sept 2000, 0130 UTC. (a) Brightness temperatures (K) near 183 ± 7-GHz. (b) Brightness temperatures (K) near 183 ± 3-GHz. (c) Brightness temperature perturbations (K) near 52.8 GHz. (d) Inferred 15-km-resolution brightness temperature perturbations (K) near 52.8 GHz. 65

4-12 Precipitation rates (mm/h) above 0.5 mm/h observed on 13 Sept 2000, 0130 UTC. (a) 15-km-resolution NEXRAD retrievals, (b) 15-km-resolution AMSU retrievals, (c) 50-km-resolution NEXRAD retrievals, and (d) 50-km-resolution AMSU retrievals. 70

4-13 Comparison of AMSU and NEXRAD estimates of rain rate at 15-km resolution. 71

4-14 Comparison of AMSU and NEXRAD estimates of rain rate at 50-km resolution. 72

4-15 AMSU precipitation-rate retrievals (mm/h) with 15-km resolution. (a) Philippines, April 16, 2000, (b) Indochina, July 5, 2000, (c) Canada, August 2, 2000, and (d) New England snowstorm, March 5, 2001. Precipitation rate retrievals exceed 0.5 mm/h in the shaded regions, and contours are drawn for 0.5, 2, 8, 32, and 128 mm/h. The peak retrieved values are 47, 143, 30, and 1.5 mm/h in (a), (b), (c), and (d), respectively. 76

5-1 NOAA-16 AMSU-B data over the Kara Sea (Northern Russia) on 1 July 2002, 0005 to 0008 UTC, at (a) 150 GHz and (b) 183 ± 7 GHz. . 79

5-2 NOAA-15 AMSU-B data over the Greenland Sea on 1 Jan 2002, 0816 to 0819 UTC, at (a) 150 GHz and (b) 183 ± 7 GHz. 80

5-3 Aqua AMSU/HSB rain rate retrievals for four consecutive overpasses by Aqua on 20 July 2002 around (a) 1122 UTC, (b) 1300 UTC, (c) 1438 UTC, and (d) 1615 UTC 81

5-4 Aqua AMSU/HSB precipitation-induced perturbations in the 52.8-GHz channel for four consecutive overpasses by Aqua on 20 July 2002 around (a) 1122 UTC, (b) 1300 UTC, (c) 1438 UTC, and (d) 1615 UTC. The perturbations seen near 75° W are likely to be the result of surface effects 82

5-5 MM5 prediction of rain rate (mm/h), 20 July 2002, 1000-1100 UTC. The blue curves over ocean are pressure (mbar) contours, and the black curves are precipitation (mm/h) contours. Precipitation contours are drawn for multiples of 0.1 mm/h. Peak rain rate is ∼1 mm/h. (This image was provided by L. Bai and D.H. Bromwich) 83

6-1 Scatter plot of $5° \times 5°$ uncorrected AMSU/HSB rain rates and AMSR-E rain rates. $5° \times 5°$ boxes for which the AMSU/HSB rain rate was less than 0.1 mm/h were excluded from the training, validation, and testing sets 88

6-2 Scatter plot of 5° × 5° AMSR-E-adjusted AMSU/HSB rain rates and AMSR-E rain rates 88

6-3 Cumulative distribution curves of 5° × 5° AMSU/HSB and AMSR-E rain rates between 50° N and 50° S 89

6-4 Cumulative distribution curves of 5° × 5° AMSU/HSB and AMSR-E rain rates between 50° N and 70° N and between 50° S and 70° S . . 89

6-5 Latitude-dependent weights for AMSR-E-adjusted precipitation estimates 90

6-6 Scatter plot of AMSU estimates [(a) NEXRAD-trained and (b) hybrid] vs. NEXRAD estimates for the NEXRAD-based testing set of Chapter 4 91

6-7 Scatter plot of AMSU estimates [(a) NEXRAD-trained and (b) hybrid] vs. AMSR-E estimates for the AMSR-E-based testing set of Sec. 6.1 . 91

6-8 Corrected NOAA-16 AMSU-A/B rain rates for descending segments, 1 July 2003, ∼2 AM local time 93

6-9 Corrected NOAA-16 AMSU-A/B rain rates for descending segments, 19 Feb. 2003, ∼2 AM local time 93

6-10 15-km 1-year mean rain rate (mm/h) (July 2002 to June 2003) estimated using AMSU-A/B aboard NOAA-15, NOAA-16, and NOAA-17 94

6-11 15-km 1-year rain frequency (July 2002 to June 2003) estimated using AMSU-A/B aboard NOAA-15, NOAA-16, and NOAA-17 95

6-12 Diurnal variations of 10° × 10° precipitation rate over one year (July 2002 to June 2003) of AMSU-A/B data from NOAA-15, NOAA-16, and NOAA-17. The length of an arrow is proportional to the mean-normalized diurnal amplitude values of up to 0.5. The direction of the arrows represent local solar times for maximum rain rate. The background is an image of the annual mean rain rate. 102

6-13 Diurnal variations of 10°×10° precipitation rate (as in Fig. 6-12) during summer months (June 2003, July 2002, and August 2002) of AMSU-A/B data from NOAA-15, NOAA-16, and NOAA-17 103

6-14 Diurnal variations of $10^\circ \times 10^\circ$ precipitation rate (as in Fig. 6-12) during fall (Sept. to Nov. 2002) of AMSU-A/B data from NOAA-15, NOAA-16, and NOAA-17 104

6-15 Diurnal variations of $10^\circ \times 10^\circ$ precipitation rate (as in Fig. 6-12) during winter (Dec. 2002 to Feb. 2003) of AMSU-A/B data from NOAA-15, NOAA-16, and NOAA-17 105

6-16 Diurnal variations of $10^\circ \times 10^\circ$ precipitation rate (as in Fig. 6-12) during spring (March to May 2003) of AMSU-A/B data from NOAA-15, NOAA-16, and NOAA-17 106

A-1 Corner region and methods for salvaging pixels. 114

List of Tables

2.1 AMSU-A Channels 37

2.2 AMSU-B Channels 37

4.1 Data used in limb-and-surface correction of AMSU-A channels 52

4.2 List of rainy orbits used for training, validation, and testing 66

4.3 RMS AMSU/NEXRAD discrepancies (mm/h) at 15-km and 50-km resolution for pixels in the ranges 30-110 km and 110-230 km of NEXRAD radar sites 73

6.1 AMSU/NEXRAD comparisons at 15-km resolution for pixels in the range 30-110 km from NEXRAD radar sites. Pixels are categorized by NEXRAD rain rate 96

6.2 AMSU/NEXRAD comparisons at 15-km resolution for pixels in the range 30-110 km from NEXRAD radar sites. Pixels are categorized by AMSU rain rate 97

6.3 AMSU/HSB vs. AMSR-E comparisons for $5^\circ \times 5^\circ$ averages over ocean. Boxes are categorized by AMSR-E rain rate 97

6.4 AMSU/HSB vs. AMSR-E comparisons for $5^\circ \times 5^\circ$ averages over ocean. Boxes are categorized by AMSU/HSB rain rate 98

Chapter 1

Introduction

Precipitation is an important part of the global energy cycle since moisture is an important channel of atmospheric heat transport. When water evaporates, heat is absorbed from the environment. When water vapor condenses to form water or ice particles, this latent heat is released, warming the surrounding air. The released heat can affect the motion of the surrounding air and can result in convective precipitation. Accurate global estimates of precipitation rate will lead to a better understanding of atmospheric circulation and to improved climatology, weather forecasting, and climate change studies [85].

Ground-based methods for measuring precipitation include rain gauges and radars. However, using such methods for global observation of precipitation is impractical since they are expensive to install and operate over all land masses and certainly over ocean. Satellites, on the other hand, are able to make observations all over the world.

1.1 Problem Statement

This thesis is an effort to show that opaque microwave frequency bands are useful for estimating precipitation. (In this thesis, a microwave frequency band [in the range of 1 to 300 GHz] is called *opaque* if channels that measure thermal radiation in that band are not predominantly sensitive to surface variations. Otherwise, it is called *transparent*. A channel measuring within a *transparent* band is called a *window*

channel.) This will be demonstrated in two ways: the development of an algorithm for estimating instantaneous precipitation rates, and climatological studies based on the resulting algorithm.

1.1.1 Precipitation-Rate Retrievals

An algorithm has been developed for data taken by the Advanced Microwave Sounding Unit (AMSU) aboard the National Oceanographic and Atmospheric Administration NOAA-15 satellite, a sun-synchronous polar-orbiting satellite. AMSU has channels in the 54-GHz and 183-GHz opaque bands, and window channels near 23.8, 31.4, 89.0, and 150.0 GHz [71]. The 54-GHz and 183-GHz opaque bands are due to oxygen and water vapor resonance lines, respectively [87]. AMSU has also been launched aboard the NOAA-16 and NOAA-17 satellites, and a nearly identical instrument has been launched aboard the NASA Aqua satellite [51]. The algorithm has been applied to data from all of these satellites.

Previous attempts to do satellite-based remote sensing of precipitation have involved exclusively window channels. Some of these attempts have involved instruments such as the Electrically Scanning Microwave Radiometer (ESMR) aboard the Nimbus-5 satellite [91] and the Scanning Multichannel Microwave Radiometer (SMMR) aboard the Nimbus-7 satellite [79]. Some recent and ongoing attempts have involved the Tropical Rainfall Measurement Mission (TRMM) coordinated by the U.S. National Aeronautics and Space Administration (NASA) and the National Space Development Agency (NASDA) of Japan [13, 43], the Special Sensor Microwave Imager (SSM/I) [49, 84], and the Advanced Microwave Sounding Radiometer for the Earth Observing System (AMSR-E) [92].

An important aspect of the development of the algorithm is the analysis of information content in single channels or groups of channels. The physics of the remote sensing of precipitation is extremely complex and no adequate models exist, so a retrieval using direct inversion is very difficult. However, single channels or groups of channels can yield useful information about properties of precipitating clouds or the surrounding atmosphere that are important determinants of precipitation.

Another important aspect of the algorithm involves resolution sharpening through data fusion. AMSU consists of two modules, AMSU-A and AMSU-B, which provide data at 50-km and 15-km nominal resolution, respectively. If possible, one would prefer to do precipitation retrievals at 15-km instead of 50-km resolution because small convective rain cells might not have significant signatures at 50-km resolution. AMSU-A results have to be sharpened to 15-km resolution in order for the algorithm to estimate rain rates at 15-km resolution.

1.1.2 Precipitation Climatology

The precipitation-rate retrieval algorithm is then used to develop a climatological model for seasonal, diurnal, and spatial variations of rain rate. Previous attempts to estimate global precipitation typically have involved multiple data sources of varying types, i.e. radar and rain gauges over land, and satellites over ocean. For example, Bellerby et al. developed a rain rate estimation method using data from TRMM and the Geostationary Operational Environmental Satellite (GOES) [7], and Gruber et al. compare two global precipitation data sets, the Global Precipitation Climatology Project (GPCP) and the CPC (Climate Prediction Center) Merged Analysis of Precipitation (CMAP), which were derived by merging satellite and rain gauge data [31]. The climatological results presented in this thesis resulted from only the algorithm developed for this thesis.

1.2 Thesis Outline

Chapter 2 addresses the physical basis of passive microwave remote sensing of precipitation. AMSU measures thermal radiation. Its measurements can be described by the radiative transfer equation and depend on factors such as temperature profile, water vapor profile, surface emissivity, and the electromagnetic properties of any hydrometeors present in its field of view. The radiative transfer equation and the complex nature of precipitation rule out the possibility of retrieving precipitation by direct inversion. However, the opaque microwave bands have properties that allow

them to reveal useful information about precipitation.

Chapter 3 addresses the signal processing techniques used in this thesis. Although retrieving precipitation rate by direct inversion is very difficult, one can still process the data in a way that reveals information about some of the most important factors that contribute to precipitation. Some of the important signal processing methods used in the algorithm include principal component analysis, neural nets, and data fusion.

Chapter 4 addresses the algorithm developed for this thesis. The components of the algorithm are described. The training, validation, and testing of the neural net will also be described. Qualitative and quantitative evaluations of the algorithm will also be presented.

Chapter 5 addresses polar precipitation and snow. During the course of the research described in this thesis, the algorithm demonstrated the ability to detect and estimate snow. This chapter will discuss why this is possible and how one can detect polar precipitation and snow in other regions of the world.

Chapter 6 addresses precipitation climatology studies. First, climatology-based validation and adjustments of the algorithm will be presented. Then, other climatological studies involving rain rate averages, rain frequencies, and diurnal variations will also be presented.

Chapter 7 provides a summary of this thesis.

Chapter 2

Physical Basis of Passive Microwave Remote Sensing of Precipitation

2.1 Thermal Radiation and Radiative Transfer

Matter radiates thermal energy depending on its physical temperature and characteristic properties. When a spaceborne radiometer makes an observation for a location on the earth, the amount of energy it receives depends on contributions from the various atmospheric and topographical constituents within its field of view (Fig. 2-1). One useful quantity describing the amount of thermal radiation emitted by a body is *spectral brightness*. Spectral brightness is a measure of how much energy a body radiates at a specified frequency per unit receiving area, per transmitting solid angle, per unit frequency. The spectral brightness of a blackbody[1] ($\mathrm{W \cdot ster^{-1} \cdot m^{-2} \cdot Hz^{-1}}$) is a function of its physical temperature T (K) and frequency f (Hz) and is given by the following formula:

[1] A blackbody is a body that absorbs all of the energy it receives [87]

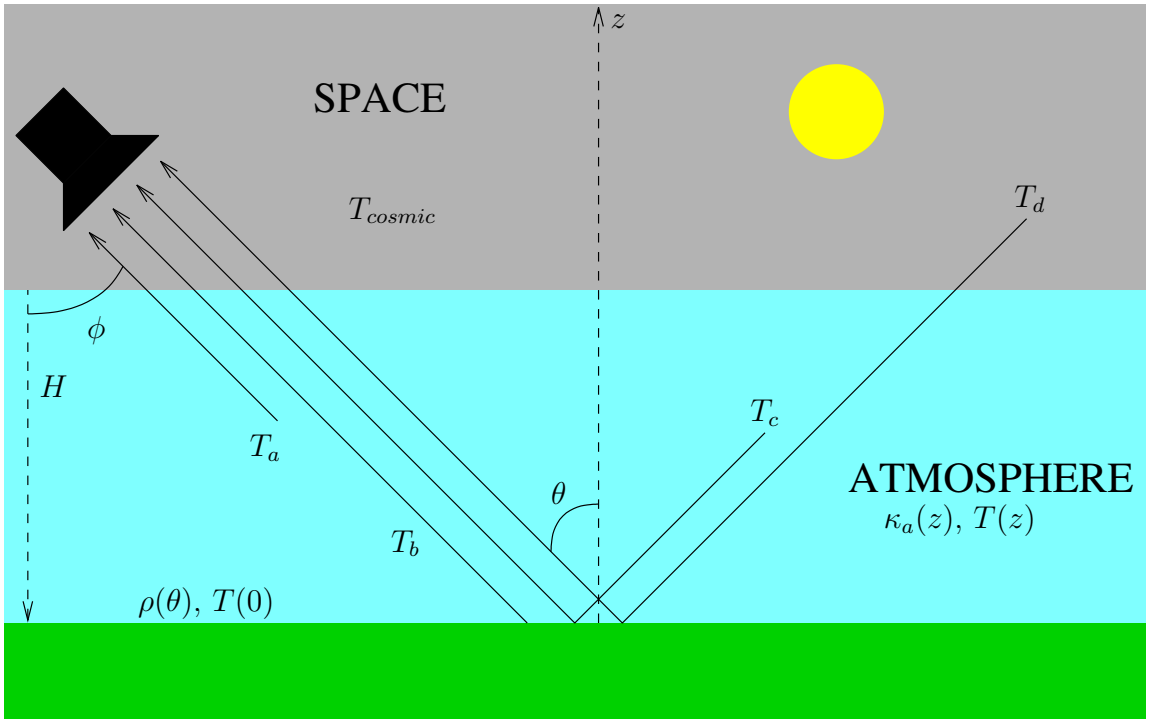

Figure 2-1: The major components of the radiative transfer equation (NOTE: $\theta \neq \phi$ since the surface of the earth is spherical)

$$B(f,T) = \frac{2hf^3}{c^2(e^{hf/kT}-1)} \tag{2.1}$$

where h is Planck's constant (J·s), c is the speed of light (m/s), and k is Boltzmann's constant (J/K). For this thesis, f never exceeds 200 GHz, and T never falls below 100 K, so $hf/kT < 0.1$. Then, the Taylor series expansion for exponential functions can be used to simplify Eq. 2.1.

$$e^{hf/kT} - 1 = \left[1 + \frac{hf}{kT} + \frac{1}{2!}\left(\frac{hf}{kT}\right)^2 + \cdots\right] - 1 \tag{2.2}$$

$$\approx \frac{hf}{kT} \tag{2.3}$$

$$B(f,T) \approx \frac{2kT}{\lambda^2} \tag{2.4}$$

where λ is the wavelength (m) associated with the frequency f.

For blackbodies, given an observation of spectral brightness, one can calculate the physical temperature of a blackbody:

$$T = \frac{B(f,T)\lambda^2}{2k} \tag{2.5}$$

Unlike blackbodies, grey bodies reflect some of the energy incident upon them, so the intrinsic spectral brightness of a grey body is not equal to that of a blackbody. For a grey body,

$$B(f,T) = \epsilon\frac{2kT}{\lambda^2} \tag{2.6}$$

where ϵ is the emissivity of the grey body. This equation can be rewritten as follows:

$$B(f,T) = \frac{2k}{\lambda^2}\epsilon T \tag{2.7}$$

The quantity ϵT is called the *brightness temperature* of an unilluminated grey body, i.e. the temperature of a blackbody radiating the same brightness. Another useful property of a grey body is its reflectivity ρ, the fraction of incident energy that is reflected. A body in thermal equilibrium will emit the same amount of energy that it absorbs. Therefore, $\rho + \epsilon = 1$. For a blackbody, $\epsilon = 1$, and $\rho = 0$.

In an atmosphere without hydrometeors, the brightness temperature observed by an earth-observing spaceborne radiometer can be divided into four components (Fig. 2-1):

- T_a, the brightness temperature due to radiation emitted by atmospheric gases that is not reflected off of the surface

- T_b, the brightness temperature due to radiation emitted by the surface

- T_c, the brightness temperature due to radiation that is emitted by atmospheric gases that is reflected off the surface

- T_d, the brightness temperature due to cosmic background radiation which passes through the atmosphere twice and is reflected off of the surface

Thermal radiation can be attenuated through absorption or reflected off of the surface before being received by a radiometer. The observed brightness temperature is, therefore, a function of several variables such as the atmospheric temperature profile, water vapor profile, the emissivity of the surface (as a function of satellite zenith angle), and the absorption coefficients of atmospheric gases (as a function of altitude z). Given the atmospheric absorption coefficients $\kappa_a(z)$ (in Np per unit length)[2], the reflectivity of the surface $\rho(\theta)$, the altitude of the satellite H, the cosmic background temperature T_{cosmic} (in K), and the satellite zenith angle θ, the brightness temperature components can be computed as follows (assuming specular surface reflection and the absence of hydrometeors):

$$T_a = \sec\theta \int_{z_0}^{H} T(z')\kappa_a(z')e^{-\tau(z',H)\sec\theta}dz' \tag{2.8}$$

$$T_b = [1-\rho(\theta)]T(z_0)e^{-\tau(z_0,H)\sec\theta} \tag{2.9}$$

$$T_c = \rho(\theta)\sec\theta \cdot e^{-\tau(z_0,H)\sec\theta} \int_{z_0}^{\infty} T(z')\kappa_a(z')e^{-\tau(z_0,z')\sec\theta}dz' \tag{2.10}$$

$$T_d = \rho(\theta)T_{cosmic}e^{-2\tau(z_0,H)\sec\theta} \tag{2.11}$$

Then, the brightness temperature T_B measured by the radiometer is the sum of T_a, T_b, T_c, and T_d.

[2]A neper (Np) represents a factor of e. 10 dB = 2.303 Np

$$
\begin{aligned}
T_B &= \sec\theta \int_{z_0}^{H} T(z')\kappa_a(z')e^{-\tau(z',H)\sec\theta}dz' \\
&\quad +[1-\rho(\theta)]T(z_0)e^{-\tau(z_0,H)\sec\theta} \\
&\quad +\rho(\theta)\sec\theta \cdot e^{-\tau(z_0,H)\sec\theta}\int_{z_0}^{\infty} T(z')\kappa_a(z')e^{-\tau(z_0,z')\sec\theta}dz' \\
&\quad +\rho(\theta)T_{cosmic}e^{-2\tau(z_0,H)\sec\theta}
\end{aligned} \tag{2.12}
$$

where z_0 is the altitude of the surface and $\tau(z_1, z_2)$ is the integrated atmospheric absorption of the atmosphere between altitudes z_1 and z_2.

$$
\tau(z_1, z_2) = \int_{z_1}^{z_2} \kappa_a(z)dz \tag{2.13}
$$

Eq. 2.12 can be rewritten as follows (assuming that the contribution of thermal radiation from altitudes above H to T_c is negligible):

$$
T_B = \int_{z_0}^{H} T(z')W(z')dz' + [1-\rho(\theta)]T(z_0)e^{-\tau(z_0,H)\sec\theta} + \rho(\theta)T_{cosmic}e^{-2\tau(z_0,H)\sec\theta} \tag{2.14}
$$

where

$$
W(z) = \sec\theta \cdot \kappa_a(z)e^{-\tau(z,H)\sec\theta} + \rho(\theta)\sec\theta \cdot e^{-\tau(z_0,H)\sec\theta}\kappa_a(z)e^{-\tau(z_0,z)\sec\theta} \tag{2.15}
$$

$W(z)$ is called the *weighting function*.

Eq. 2.12 shows that the relationship between the thermal energy radiated and the physical temperature of a body is linear, i.e. the brightness temperature can be expressed as a linear integral of physical temperatures in the field of view, where these radiated signals are uncorrelated and superimpose [87].

2.2 Passive Microwave Remote Sensing of the Atmosphere

The previous section shows that the brightness temperatures seen by a satellite-borne radiometer depends on many variables in a highly complex and nonlinear fashion, so retrievals of temperature and water vapor profiles by direct inversion would be very difficult. However, the physics of the atmosphere still allows one to extract useful information about the atmosphere from microwave frequency bands.

2.2.1 Temperature and Water Vapor Profiles

Two of the most important determinants of precipitation rate are the temperature and water vapor profiles. The presence of oxygen and water vapor resonance frequencies in the microwave spectrum and the presence of oxygen and water vapor in the atmosphere results in frequency bands that are sensitive primarily to a specific range of altitudes. Fig. 2-2 shows the zenith opacity as a function of frequency for the range from 10 to 500 GHz for a ground-based zenith-observing radiometer. There are absorption spikes around oxygen resonance frequencies such as those in the neighborhood of 54, 118.75, and 424.76 GHz and at water vapor resonance frequencies such as 183.31 GHz. A satellite-borne radiometer observing at these frequencies would sense only the highest layers of the atmosphere. On the other hand, a satellite-borne radiometer observing at frequencies away from the spikes would be sensitive to the surface. By observing at frequency bands that are near the resonance frequencies but still on the sides of the spikes, one can capture information on conditions at specific layers of the atmosphere.

The Advanced Microwave Sounding Unit (AMSU) focuses primarily on the 54-GHz oxygen band and the 183-GHz water vapor band. Fig. 2-3 shows the weighting functions of the channels on AMSU.

Opaque microwave channels have been used with great success to retrieve atmospheric conditions. Rosenkranz has used AMSU-A and AMSU-B data from NOAA

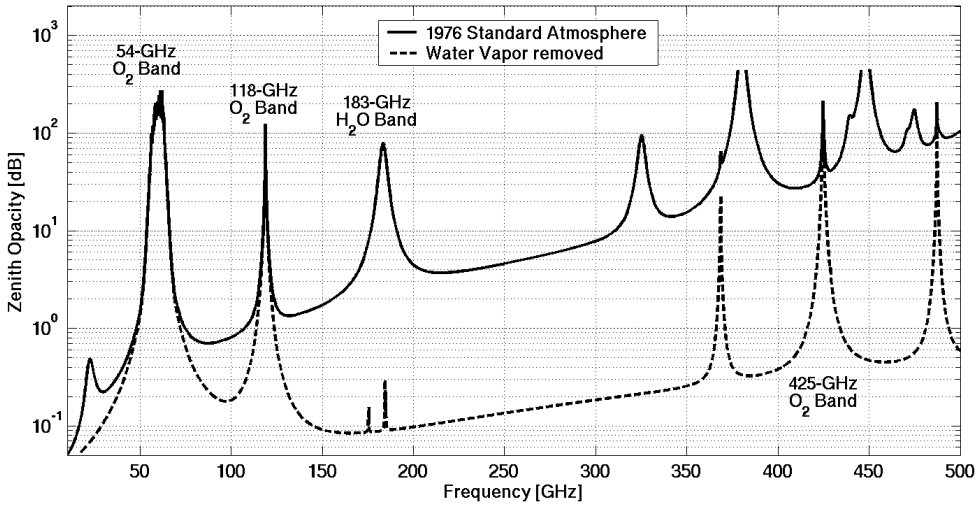

Figure 2-2: Zenith opacity for the microwave spectrum

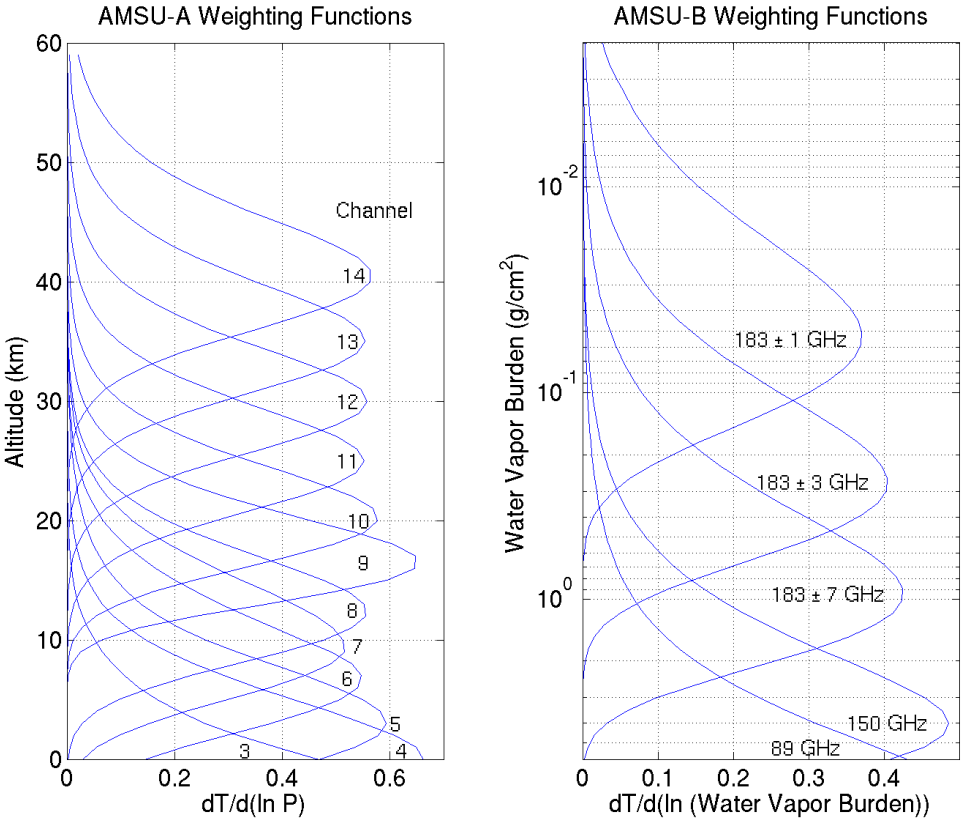

Figure 2-3: Weighting functions of AMSU-A and AMSU-B channels

satellites to estimate temperature and water vapor profiles [72, 73]. Shi has used AMSU-A to estimate temperature profiles [75]. Blackwell et al. used the 54-GHz and 118-GHz bands aboard the NPOESS (National Polar-Orbiting Environmental Satellite System) Aircraft Sounder Testbed-Microwave (NAST-M) [9]. Leslie et al. have since then added the 183-GHz and 425-GHz bands to NAST-M [54, 55, 56].

2.2.2 Clouds and Precipitation

Clouds and precipitation result from humid air that rises, cools, and condenses. Precipitation typically occurs in two forms: convective and stratiform. Stratiform precipitation occurs when one air mass slides under or over another as in a cold or warm front causing the upper air mass to cool and the water vapor within it to condense. Such precipitation can be spread out. Convective precipitation is initiated by instabilities in the atmosphere caused by cold, dense air being supported by warm, humid, and less dense air. Such an instability results in the warm, humid air escaping upward and cooling. Water vapor in this ascending air mass condenses and releases latent heat. The latent heat warms the surrounding air which pushes the air mass and the water and ice particles that have formed futher upward. This cycle continues until the original warm humid air mass has cooled to the temperature of the surrounding cooler air [37, 85]. The tops of convectives clouds spew forth ice particles and can reach more than 10 km above sea level [38]. It is possible for convective precipitation to occur within stratiform precipitation.

Several factors can affect precipitation rate. Higher degrees of instability caused by large vertical temperature gradients can force ice particles higher in the atmosphere causing such particles to pick up more moisture and grow. Precipitation amounts are limited by the water vapor available in the atmosphere, so higher concentrations of water vapor can result in higher precipitation rates. Warmer surface air also can contribute to higher precipitation rates because warmer air can hold more water vapor.

Remote Sensing Using Opaque Channels

Channels in the 54-GHz and 183-GHz bands can provides important clues about factors such as cloud-top altitude, temperature profile, water vapor profile, and particle size distribution. Because each channel is sensitive to a specific layer of the atmosphere (Fig. 2-3), it is possible to extract information about cloud-top altitude. Precipitating clouds will exhibit perturbations in channels whose weighting functions have significant values in the range of altitudes occupied by the cloud. For example, one would not expect to detect low-lying clouds below 3 km in AMSU-A channel 14 since the weighting function of channel 14 peaks at ∼40 km, far above the tops of nearly all precipitating clouds.

The 54-GHz and 183-GHz together provide information about particle size distribution through their sensitivities to different ranges of ice particle diameters. The scattering of electromagnetic waves by spherical ice particles can be described by Mie scattering coefficients. For a single spherical particle with radius r, given the power scattered by the particle P_s and the power density of the incident plane wave S_i, the scattering cross-sectional area Q_s of the particle is defined as follows:

$$Q_s = \frac{P_s}{S_i} \tag{2.16}$$

Then, the Mie scattering coefficient is defined as as the ratio of Q_s of the particle to the geometric cross-sectional area of the particle:

$$\xi_s = \frac{Q_s}{\pi r^2} \tag{2.17}$$

where r is the radius of the particle. Fig. 2-4 shows the Mie scattering coefficients for fresh-water ice spheres at 54 GHz and 183.31 GHz as a function of diameter. The permittivities of ice were calculated using formulas developed by Hufford [39], and the Mie scattering coefficients were calculated using an iterative computational procedure developed by Deirmendjian [22, 87]. At 183.31 GHz, the diameter of a particle can increase to about 0.7 mm before its diameter can no longer be uniquely determined by the Mie scattering coefficient curve. At 54 GHz, this limit is about 2.4

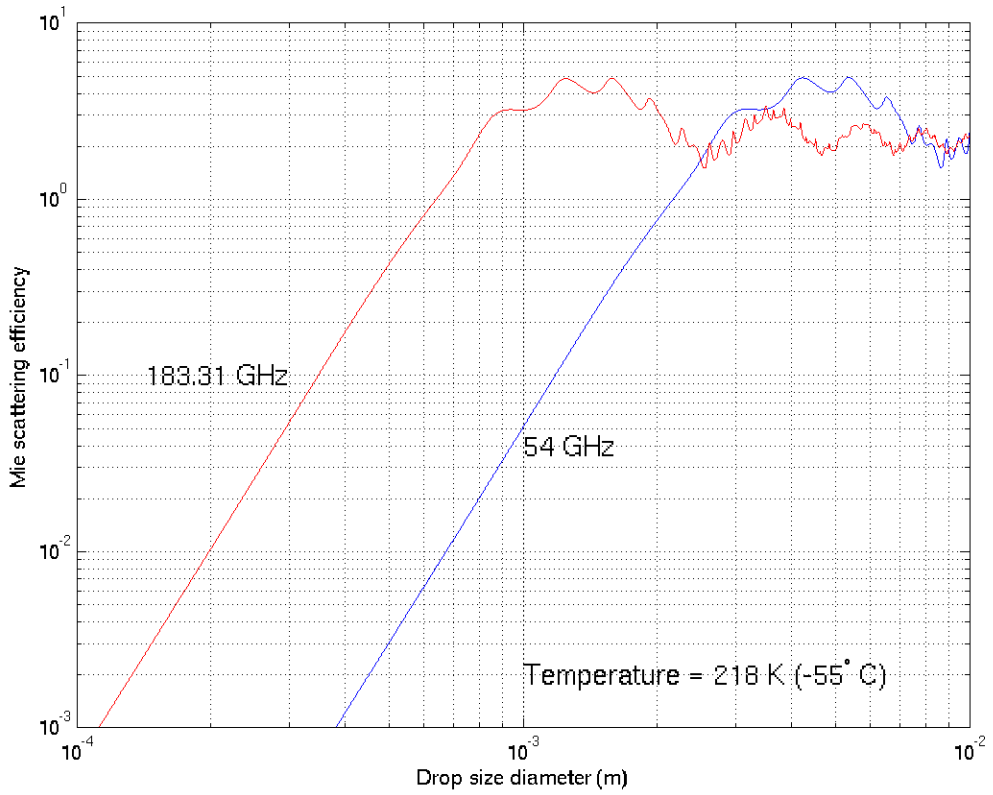

Figure 2-4: Mie scattering coefficients for 54 GHz and 183.31 GHz at a temperature of −55° C

mm. For diameters less than 0.7 mm, ξ_s for 54 GHz is smaller than that for 183.31 GHz by a factor of at least 100. These differences make it possible to use both bands together to extract information about particle size distributions. The Mie scattering coefficients in Fig. 2-4 were calculated for a temperature of −55° C (218 K), near the temperature at an altitude of 10 km for the 1962 U.S. Standard Atmosphere [87]. Corresponding values for −10° C (263 K) were also calculated but did not differ from those for −55° C by more than 7.2 percent.

In addition to particle size distribution, the 54-GHz and 183-GHz bands can also provide information about particle abundance. While the particle size distribution can be sensed from a comparison of the Mie scattering efficiencies in both bands, particle abundance can be sensed from absolute scattering over volumes.

Another important variable in precipitation is cloud-top altitude. This is cor-

related with particle size density because only higher updraft velocities are able to support larger particles and reach higher altitudes. The sensitivities of the 54-GHz and 183-GHz channels to specific layers of the atmosphere suggest that these channels will be able to provide information about cloud-altitude. Spina et al. used data from the opaque 118-GHz band to estimate cloud-top altitudes [80].

Gasiewski showed that the 54-GHz and 118-GHz bands together could be used to estimate cell-top altitude and hydrometeor density (in terms of mass per volume) [25, 26].

Remote Sensing Using Window Channels

Window channels contribute information about precipitation through their sensitivity to the warm emission signatures of precipitating clouds against a sea background and their sensitivity to scattering. In addition to opaque channels, AMSU also includes window channels at 23.8, 31.4, 89.0, and 150 GHz. Weng et al. and Grody et al. have developed a precipitation-retrieval algorithm for AMSU that relies primarily on these channels [30, 89]. Some of the recent passive microwave instruments that have focused on windows channels and have been used to study precipitation include the following:

- The Special Sensor Microwave Imager (SSM/I) for the Defense Meteorological Satellite Program (DMSP) [36, 49, 84]
- The Advanced Microwave Sounding Radiometer for the Earth Observing System (AMSR-E) abord the NASA Aqua satellite [45, 92]
- The Tropical Rainfall Measurement Mission (TRMM) Microwave Imager (TMI) aboard the TRMM satellite [43, 50]

One weakness of window channels is that they tend to be sensitive to the surface. Over land, surface signatures can obscure the emission signatures of precipitation. Also, window-channel-based precipitation-rate retrieval algorithms tend to use one method over ocean and another over land [49, 92]. The opaque channels aboard

AMSU enable the development of an algorithm that uses the same method over both land and sea.

2.3 Description of the Relevant Instruments

2.3.1 AMSU on the NOAA-15, NOAA-16, and NOAA-17 Satellites

The Advanced Microwave Sounding Unit (AMSU) is a radiometer aboard the NOAA-15, NOAA-16, and NOAA-17 satellites launched in May 1998, September 2000, and June 2002, respectively. They are each equipped with the instruments AMSU-A and AMSU-B. AMSU-A has 15 channels: one each at 23.8 GHz, 31.4 GHz, and 89.0 GHz, and 12 channels in the 54-GHz oxygen absorption band (Table 2.1). AMSU-B has 5 channels at the following frequencies: 89.0 GHz, 150 GHz, 183.31±1 GHz, 183.31±3 GHz, and 183.31±7 GHz (Table 2.2). AMSU-A and AMSU-B measure brightness temperatures at 50-km and 15-km nominal resolutions at nadir, respectively. AMSU-A has a 3.33°-diameter 3-dB beamwidth and observes at 30 angles spaced at 3.33° intervals up to 48.33° from nadir every 8.00 seconds. AMSU-B has a 1.1°-diameter beamwidth and observes at 90 angles spaced at 1.1° intervals up to 48.95° from nadir every 2.67 seconds (Fig. 2-6(b)) [35, 61, 71]. AMSU covers a swath width of ∼2200 km. NOAA-15, NOAA-16, and NOAA-17 are sun-synchronous polar orbiting satellites with equatorial crossing times of about 7 AM/PM, 2 AM/PM, and 10 AM/PM, respectively, so together they observes most locations approximately six times a day (Fig. 2-5).

The 15-km 89.0-GHz channel on AMSU-B was not used in this research because this channel is not available on the Humidity Sounder for Brazil (HSB) described in Sec. 2.3.2.

Channel	Channel Frequencies (MHz)	Bandwidth (MHz)
1	23,800±72.5	2×125
2	31,400±50	2×80
3	50,300±50	2×80
4	52,800±105	2×190
5	53,596±115	2×168
6	54,400±105	2×190
7	54,940±105	2×190
8	55,500±87.5	2×155
9	57,290.344±87.5	2×155
10	57,290.344±217	2×77
11	57,290.344±322.2±48	4×35
12	57,290.344±322.2±22	4×15
13	57,290.344±322.2±10	4×8
14	57,290.344±322.2±4.5	4×3
15	89,000±1000	2×1000

Table 2.1: AMSU-A Channels

Channel	Center Frequencies (GHz)	Bandwidth (GHz)
1	89±0.9	2×1
2	150±0.9	2×1
3	183.31±1	2×0.5
4	183.31±3	2×1
5	183.31±7	2×2

Table 2.2: AMSU-B Channels

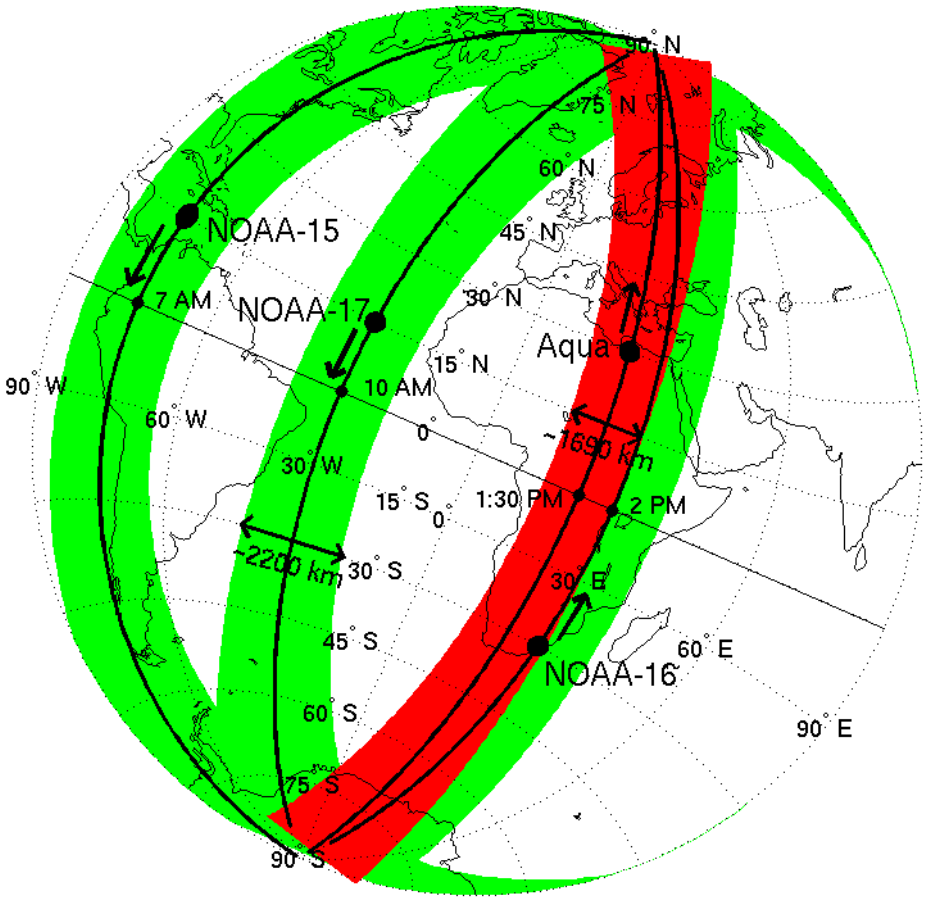

Figure 2-5: Orbital patterns of the NOAA-15, NOAA-16, NOAA-17, and Aqua satellites

2.3.2 AMSU/HSB on the Aqua Satellite

We also use data from the NASA Aqua satellite which was launched in May 2002. It is equipped with AMSU and which is identical to AMSU-A aboard the NOAA satellites, and the Humidity Sounder Brazil (HSB) which is identical to AMSU-B but without the 89.0-GHz channel [51]. The nominal resolutions of AMSU and HSB are 40.5 and 13.5 km, respectively. Aqua has an equatorial crossing time of about 1:30 AM/PM (Fig. 2-5) [3, 51, 66]. The scan pattern of AMSU/HSB is slightly different from that of AMSU-A/B on the NOAA satellites in that the path traced by one AMSU swath is more parallel to that traced by a nearly coincident HSB swath (Fig. 2-6).

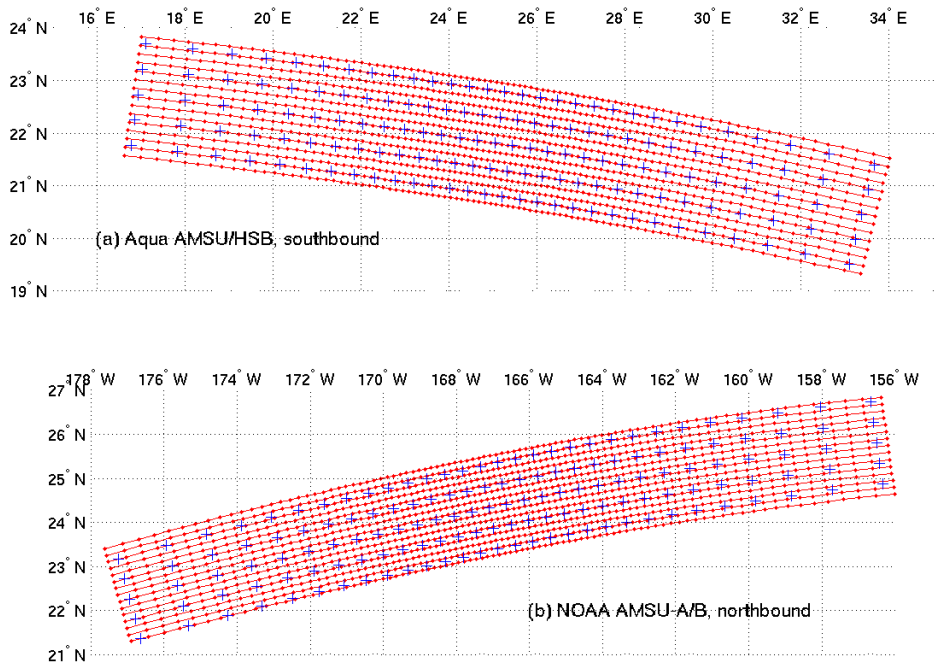

Figure 2-6: Scan patterns of (a) Aqua AMSU/HSB and (b) AMSU-A/B on NOAA-15, NOAA-16, and NOAA-17. AMSU and AMSU-A spots are labeled with blue +'s and HSB and AMSU-B spots with red dots

Chapter 3

Signal Processing and Estimation Techniques

This chapter describes some of the important signal processing and estimation concepts involved in this thesis. The physics of precipitation is extremely complicated and nonlinear to the extent that developing an adequate model would be extremely difficult. However, signal processing techniques can be used to reveal useful information about some important degrees of freedom in precipitation. The retrieval method described in this thesis is based on statistical methods.

3.1 Principal Component Analysis (PCA)

One important concept in this thesis is signal separation. Although precipitation is very complex, nonstationary, and sporadic, one can process the data in a way that adequately separates the different degrees of freedom that affect precipitation.

Principal Component Analysis (PCA) is a linear method for reducing the dimensionality of a data set of interrelated variables. PCA transforms the data into a set of uncorrelated random variables that captures all of the variance of the original data set and assigns as much variance as possible to the fewest number of variables. PCA is also known by other names such as singular value decomposition (SVD) and Karhunen-Loève transform (KLT).

PCA is useful for data compression. This feature can be critical in problems related to the compression of satellite data where a large amount of data must be downloaded from a satellite using a communications link with limited bandwidth and in situations where computational resources are limited. Blackwell used projected principal component transform, a variant of PCA, to compress data for use in estimating atmospheric temperature profiles. This reduced the number of inputs and, as a result, simplified the neural net, created a more stable neural net, and reduced the training time [8, 10]. Cabrera-Mercader used Noise-Adjusted Principal Components (NAPC) to compress simulated NASA Atmospheric Infrared Sounder (AIRS) data [11].

PCA can also be used to filter out noise in data. Several different versions or extensions of PCA have been used to eliminate various types of noise. A variant of PCA has been used to remove signatures of the surface from passive microwave data for the purpose of detecting and characterizing precipitating clouds [14]. PCA is also an important part of blind multivariate noise estimation and filtering algorithms such as Iterative Order and Noise estimation (ION) and an extension of ION that is capable of estimating mixing matrices [52, 53, 62, 63].

3.1.1 Basic PCA

Here, a definition of basic PCA is presented. For a random vector $\mathbf{x}$ of p random variables, the *principal components* of $\mathbf{x}$ can be defined inductively. The first principal component is the product $\alpha_1^T\mathbf{x}$ where α_1 is a unit-length vector that maximizes the variance of $\alpha_1^T\mathbf{x}$.

$$\alpha_{\mathbf{1}} = \text{argmax}_{\|\alpha\|=1} Var(\alpha^T\mathbf{x}) \tag{3.1}$$

where Var denotes the variance of a random variable. Each of the other principal components are defined as follows: the nth principal component is the product $\alpha_n^T\mathbf{x}$ where α_n is a unit-length vector that is orthogonal to α_1, ..., α_{n-1} that maximizes the variance of $\alpha_n^T\mathbf{x}$.

$$\alpha_n = \text{argmax}_{\|\alpha\|=1, \alpha \perp \alpha_i \forall i=1,\ldots,n-1} Var(\alpha^T \mathbf{x}) \tag{3.2}$$

α_1, ..., α_p are derived in [44]. The nth principal component is the product $\alpha_n^T \mathbf{x}$ where α_n is the eigenvector associated with the nth highest eigenvalue of the covariance matrix $\mathbf{\Lambda_x}$ of $\mathbf{x}$.

In this thesis, the definitions of PCA and the term *principal component* follow the convention of [44].

3.1.2 Constrained PCA

In addition to basic PCA, the algorithm developed in this thesis uses a variation of PCA known as *constrained PCA*. This form of PCA finds principal components that are constrained to be orthogonal to a given subspace [44]. It can be used to filter out noise in remote sensing data. Constrained PCA has been used to filter out signatures of surface variations from microwave remote sensing data [14].

Filtering out unwanted signatures might involve the following steps:

1. Select a set of data that captures a good representation of the type of noise to be filtered without capturing too much of the variation of the signal of interest

2. Apply basic PCA to the resulting subset of data

3. Examine the resulting principal components for sensitivity to the type of noise to be filtered out

4. Project the data onto the subspace orthogonal to the noise-sensitive principal components

5. Apply basic PCA to the data resulting from the projection

The principal components resulting from steps 2 and 5 will be called *pre-constraint principal components* and *post-constraint principal components*, respectively, as in [14].

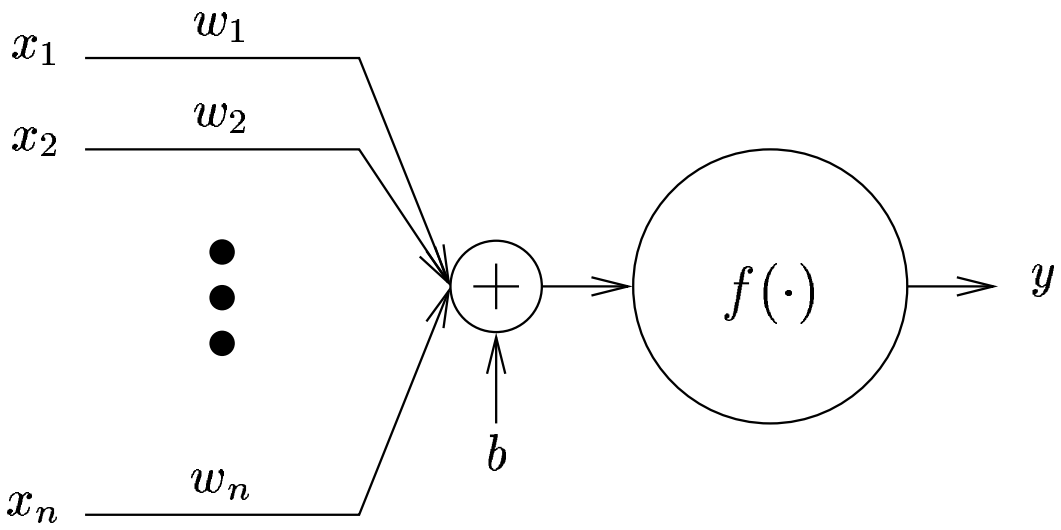

Figure 3-1: The structure of a perceptron

3.2 Neural Nets

Neural nets are computational structures that were developed to mimic the way biological neural nets learn from their environment and are useful for pattern recognition and classification. Neural nets can be used to learn and compute functions for which the relationships between inputs and outputs are unknown or computationally complex.

There are a variety of neural nets such as feedforward neural nets (sometimes called multilayer perceptrons [58]), Kohonen self-organizing feature maps, and Hopfield nets [34, 58]. The type of neural net used in this thesis is the feedforward neural net.

3.2.1 Structure of Neural Net

The basic structural element of feedforward neural nets is called a *perceptron*. It computes a function of the weighted sum of inputs and a bias as shown in Fig. 3-1.

$$y = f\left(\sum_{i=1}^{n} w_i x_i + b\right) \tag{3.3}$$

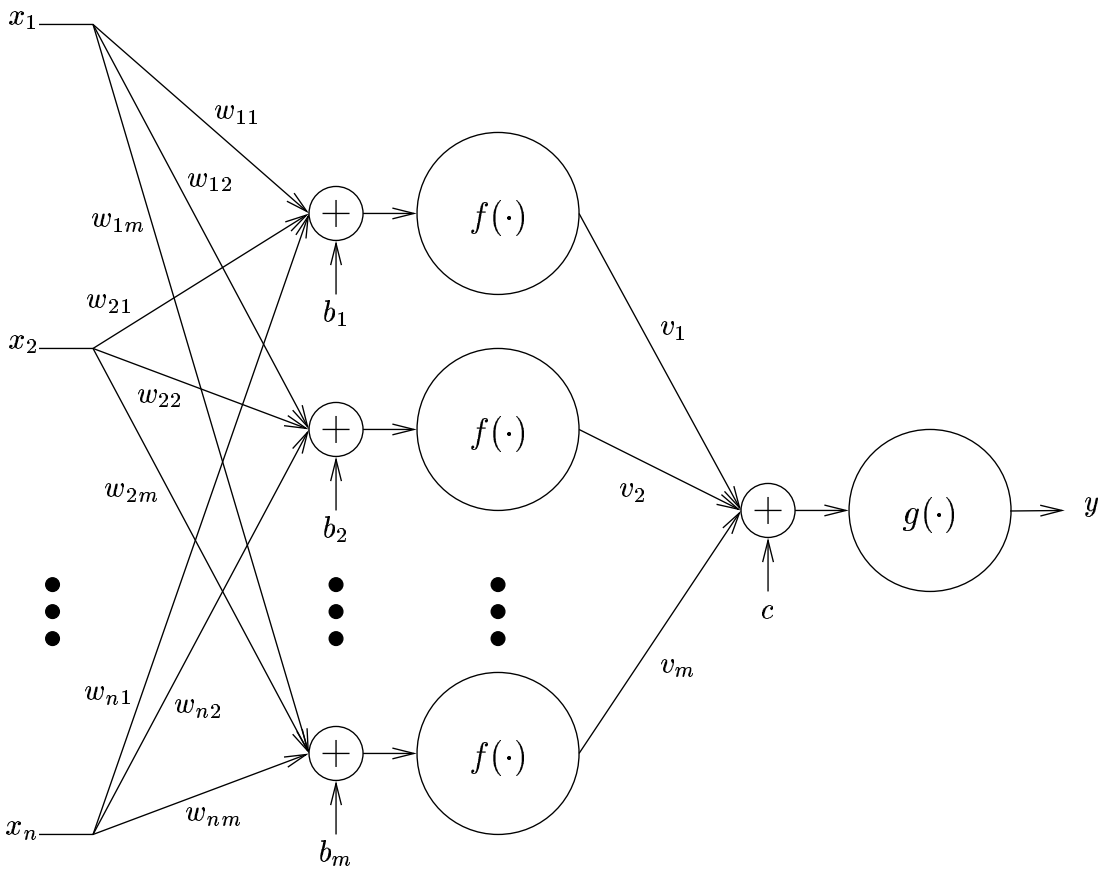

Figure 3-2: A 2-layer feedforward neural net with one output node

where x_i is the ith input, w_i is the weight associated with the ith input, b is the bias, f is the transfer function of the perceptron, and y is the output.

Perceptrons can be combined to form a multilayer network as shown in Fig. 3-2. In Fig. 3-2, x_i is the ith input, n is the number of inputs, w_{ij} is the weight associated with the connection from the ith input to the jth node in the hidden layer, b_i is the bias of the ith node, m is the number of nodes in the hidden layer, f is the transfer function of the perceptrons in the hidden layer, v_i is the weight between the ith node and the output node, c is the bias of the output node, g is the transfer function of the output node, and y is the output. Then,

$$y = g\left(\sum_{j=1}^{m} v_j f\left(\sum_{i=1}^{n} w_{ij}x_i + b_j\right) + c\right) \tag{3.4}$$

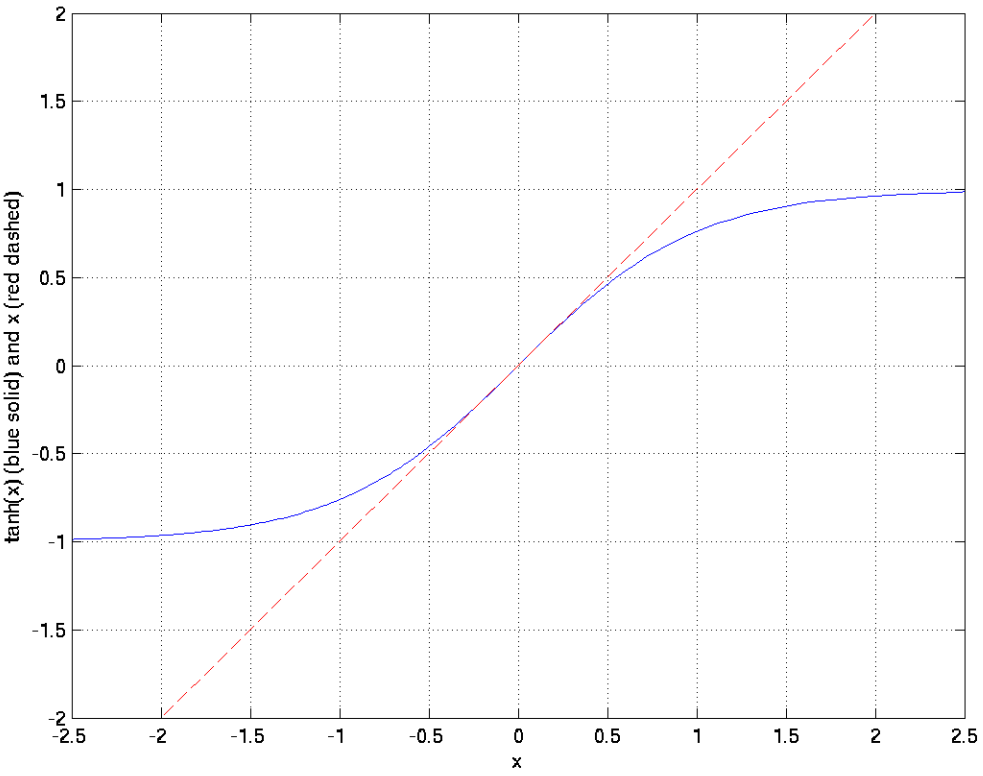

Figure 3-3: Neural net transfer functions

For this thesis, f and g are defined as follows:

$$f(x) = \tanh x = \frac{e^x - e^{-x}}{e^x + e^{-x}} \tag{3.5}$$

$$g(x) = x \tag{3.6}$$

The function $\tanh x$ is approximately linear in the range $-0.6 \leq x \leq 0.6$, and approaches 1 as x goes to ∞ and -1 as x goes to $-\infty$, so it has a nonlinearity that is not too complex (Fig. 3-3).

This neural net topology is good for situations in which one wants to develop a simple nonlinear estimator whose output depends approximately monotonically on each input.

3.2.2 Training Neural Nets

The neural nets for this thesis were trained using the Levenberg-Marquardt training algorithm. Marquardt developed an efficient algorithm (called the Marquardt-Levenberg algorithm in [32]) for nonlinear least-squares parameter estimation [60]. Hagan and Menhaj incorporated this algorithm into a backpropagation training algorithm for feedforward neural nets [32].

The weights of the neural net were initialized using the Nguyen-Widrow method in order to facilitate convergence of the neural net weights during training [64].

The vectors used to train and evaluate the neural nets were divided into three disjoint sets:

- The *training set*, the set used to determine how the weights of the neural net are to be adjusted during the training
- The *validation set*, the set used to determine when the training should stop
- The *testing set*, the set used to evaluate the resulting neural net

These definitions are from [65].

One of the challenges encountered in the course of developing an estimator involved dealing with an output range that covered several orders of magnitude. Chapter 4 describes how this was accomplished.

3.3 Data Fusion

Data fusion is a very broad area involving the combination of information from different sources. A working group set up by the European Association of Remote Sensing Laboratories and the French Society for Electricity and Electronics has adopted the following definition of data fusion [88]:

> "Data fusion is a formal framework in which are expressed means and tools for the alliance of data originating from different sources. It aims at

> obtaining information of greater quality; the exact definition of 'greater quality' will depend upon the application."

Review papers have referred to three levels of data fusion: *measurement*, *feature*, and *decision* [33, 67, 88]. The measurement level is sometimes called the *pixel level* [67]. The algorithm described in Chapter 4 involves the measurement and decision levels. In this thesis, nontrivial uses of data fusion occur only at the measurement level.

Some of the applications of image fusion (or data fusion applied to two-dimensional data) include image sharpening or enhancement [86], feature enhancement, and replacement of missing or faulty data [67]. For this research, nonlinear data fusion is applied to sharpen images. Rosenkranz developed a method for nonlinear geophysical parameter estimation through multiresolution data fusion [68, 69, 70].

Chapter 4

The Precipitation Retrieval Algorithm

This chapter[1] describes the structure and components of the precipitation-rate retrieval algorithm and a history of the development of the the algorithm.

4.1 Structure of the Algorithm

Chapter 2 showed that estimation by a physics-based direct inversion of the data would be difficult because of the highly complex and nonlinear dependence of radiometric observations on atmospheric parameters and properties of any existing hydrometeors. Therefore, a statistics-based method has been employed.

The basic structure of the algorithm includes some signal processing components and a neural net as shown in Fig. 4-1. The signal processing components process the data into forms that characterize the most important degrees of freedom related to precipitation rate such as atmospheric temperature profile, water vapor profile, cloud-top altitude, particle size distribution, and vertical updraft velocity. The neural net is trained to learn the nonlinear dependencies of precipitation rate on these variables. The dependence of precipitation rate on these variables should be monotonic, so the

[1]Permission has been granted by the IEEE to include material from the following paper: F.W. Chen and D.H. Staelin, "AIRS/AMSU/HSB Precipitation Estimates," *IEEE Transactions on Geoscience and Remote Sensing*, vol. 41, no. 2, pp. 410-417, Feb. 2003.

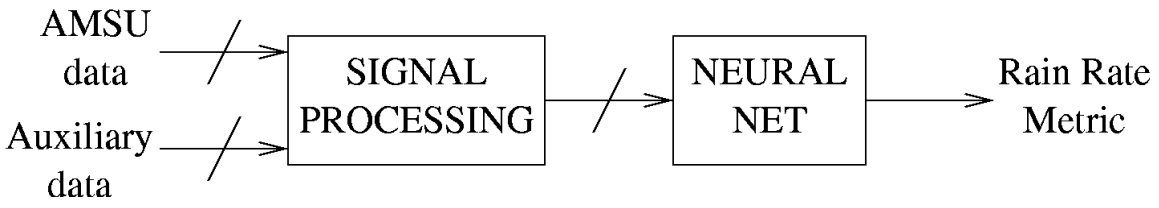

Figure 4-1: Basic structure of the algorithm

neural net does not need to be complicated. A feedforward neural net with one hidden layer of tangent sigmoid nodes (with transfer function $f(x) = \tanh x$) and one linear output node should be sufficient (Fig. 3-2) [58].

The most recent version of the precipitation retrieval algorithm is described in Figs. 4-2 and 4-3. Different stages of the development of the algorithm are presented in [15, 16, 17, 81, 82].

4.2 Signal Processing Components

This section describes the signal processing components which process AMSU data into forms that characterize information about the degrees of freedom most relevant to precipitation rate. An effort has been made to make the inputs to the neural net as insensitive to surface variations as possible so that the algorithm can be applied over land and sea.

4.2.1 Limb-and-Surface Corrections

AMSU observes at angles up to 49° away from nadir. For angles further away from nadir, electromagnetic energy originating from a given altitude and atmospheric state would have to travel longer paths before reaching the radiometer and, therefore, would be subject to more absorption and scattering effects. This results in scan-angle dependent effects in brightness temperature images as shown in Fig. 4-4(a). A limb-and-surface correction method for AMSU-A channels 4-8 brightness temperatures is needed in order to make precipitation-induced perturbations more apparent and for extracting information about atmospheric conditions. AMSU-A channels 4 and 5 will

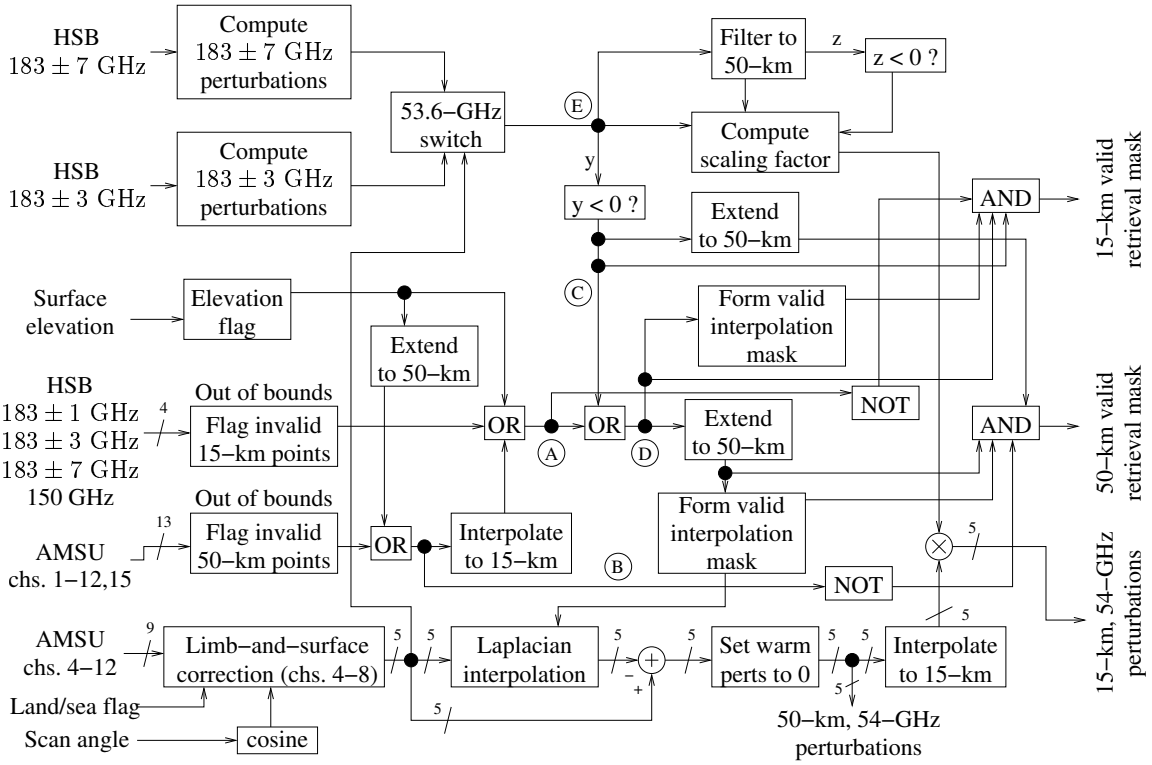

Figure 4-2: Block diagram of the algorithm, part 1

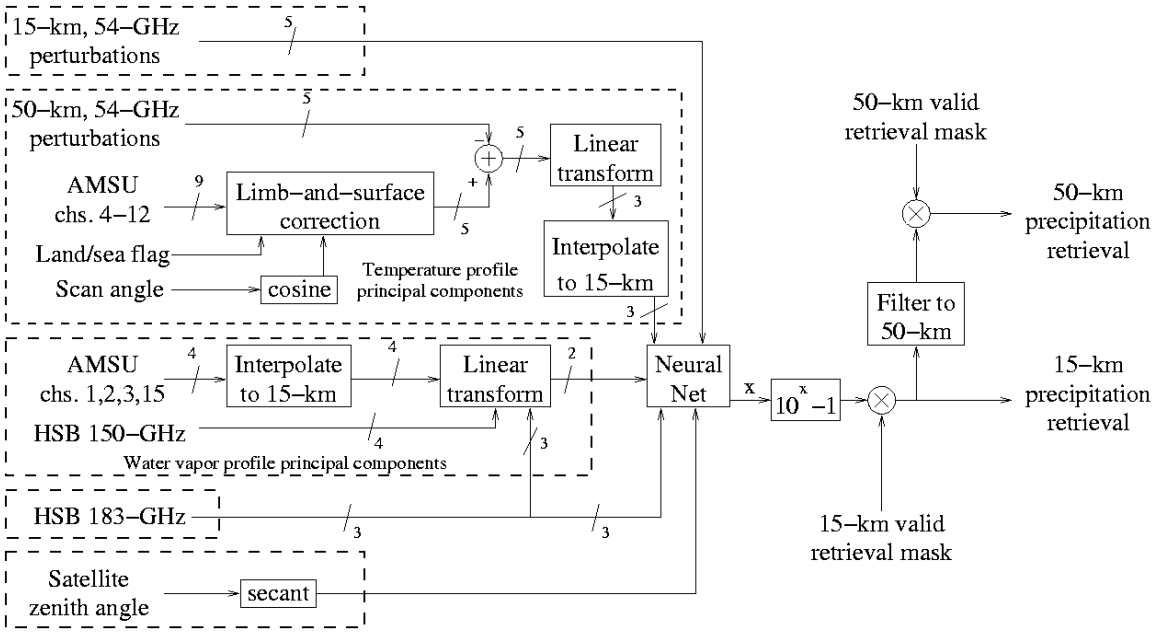

Figure 4-3: Block diagram of the algorithm, part 2

AMSU-A Channel	Inputs used for limb-and-surface correction
4	AMSU-A channels 4-12, land/sea flag, $\cos\phi$
5	AMSU-A channels 5-12, land/sea flag, $\cos\phi$
6	AMSU-A channels 6-12, $\cos\phi$
7	AMSU-A channels 6-12, $\cos\phi$
8	AMSU-A channels 6-12, $\cos\phi$

Table 4.1: Data used in limb-and-surface correction of AMSU-A channels

also be corrected for surface variations since they are sensitive to the surface. For these two channels, brightness temperature for pixels over ocean will be corrected to what might be observed for the same atmospheric conditions over land. AMSU-A channels 9-14 brightness temperatures are not corrected because they are not significantly perturbed by clouds and therefore are not used for anything besides limb-correction.

Limb-and-surface correction was done by training a neural net of the type shown in Fig. 3-2 to estimate nadir-viewing brightness temperatures. For each pixel, the neural net uses brightness temperatures from several channels at that pixel to estimate the brightness temperature seen at the pixel closest to nadir at a nearly identical latitude and at nearly the same time. It is assumed that the temperature field does not vary significantly over one scan. Limb-and-surface correction was done for AMSU-A channels 4 to 8. The data used to correct each of those channels are listed in Table 4.1. No attempt has been made to correct for the scan-angle-dependent asymmetry in the brightness temperatures. These neural nets were trained using data between 55° N and 55° S from seven orbits spaced over one year. Channels 4 and 5 are surface sensitive, so they were trained to estimate brightness temperatures that would be seen over land.

Fig. 4-4 shows a sample of (a) uncorrected and (b) limb-and-surface-corrected 54.4-GHz brightness temperatures. The shapes of precipitation systems over Texas and the Mexico-Guatemala border are more apparent after the limb correction. In Fig. 4-4(a) the difference between brightness temperatures at nadir and the swath edge is as high as 18 K. In Fig. 4-4(b), the angle-dependent variation is less than 3 K.

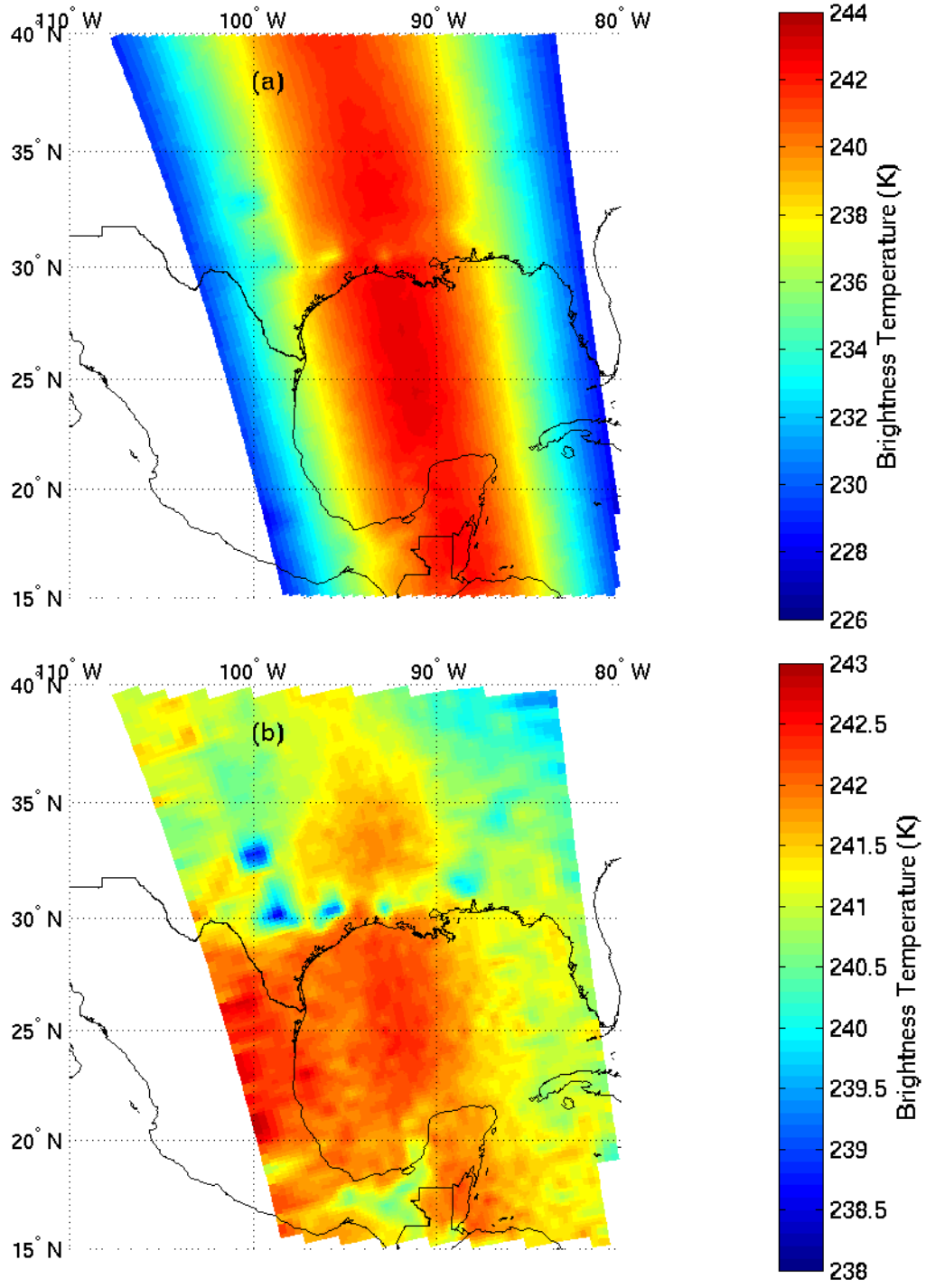

Figure 4-4: NOAA-15 AMSU-A 54.4-GHz brightness temperatures for a northbound track on 13 Sept 2000. (a) Uncorrected, and (b) Limb-and-surface corrected

One limitation of the training is that one cannot really know what the nadir-viewing brightness temperature is supposed to be when there is precipitation.

4.2.2 Precipitation Detection

The 15-km-resolution precipitation-rate retrieval algorithm, summarized in Figs. 4-2 and 4-3, begins with identification of potentially precipitating pixels. Channels used for this purpose should be sensitive to precipitation but should not exhibit large angle-dependent variations and surface variations. Unprocessed brightness temperatures from AMSU-A channels 4-14 are not used directly because they exhibit excessive angle-dependent variations or have weighting functions that peak far above the range of altitudes in which most precipitation exists (Fig. 2-3). AMSU-A channels 1, 2, 3, and 15, and the AMSU-B 89.0-GHz and 150-GHz channels were not used because of their sensitivity to surface variations. The AMSU-B channels ordered by opacity are as follows: 89-GHz (most transparent), 150-GHz, 183 ± 7-GHz, 183 ± 3-GHz, and 183 ± 1-GHz (most opaque) (Fig. 2-3). The 183 ± 7-GHz channel is the least opaque channel that is sensitive to precipitation but does not show excessive surface variations. Fig. 4-5 shows brightness temperatures at 150 GHz and 183 ± 7 GHz over the southern United States and Mexico. This figure shows the varying degrees of sensitivity to the surface of the 150-GHz channel. In this channel, the contrast between land and sea is greatest around the Gulf of California. On the other hand, the 183 ± 7-GHz channel does not show any surface variations while still being sensitive to most of the precipitation seen in the 150-GHz channel.

The 183 ± 7-GHz channel is reasonably good for detecting precipitation also because the angle-dependent variation of precipitation-free brightness temperatures is small when compared to the variation due to precipitation. All 15-km pixels with brightness temperatures at 183 ± 7 GHz that are below a threshold T_7 are flagged as potentially precipitating, where

$$T_7 = 0.667(T_{53.6} - 248) + 252 + 6\cos\theta \tag{4.1}$$

and where θ is the satellite zenith angle and $T_{53.6}$ is the spatially filtered limb-corrected 53.6-GHz brightness temperature obtained by selecting the warmest brightness temperature within a 7×7 array of AMSU-B pixels. It has been seen that the threshold T_7 can vary with atmospheric temperature. This threshold was determined empirically. However, the 183 ± 7-GHz channel can become sensitive to surface variations in very cold, dry atmospheric conditions. Fig. 4-6 shows 183 ± 7-GHz brightness temperatures in such conditions. The edges of the Great Lakes and Hudson Bay are evident in this image. When $T_{53.6}$ is less than 248 K, the 183 ± 3-GHz brightness temperature is compared to a threshold T_3.

$$T_3 = 242.5 + 5 \cos \theta \tag{4.2}$$

The thresholds T_7 and T_3 are slightly colder than a saturated atmosphere would be, implying the presence of a microwave-absorbing or scattering cloud.

It is possible for the 183 ± 3-GHz and the 183 ± 1-GHz channels to be sensitive to surface variations. Fig. 4-7 shows 183 ± 1-GHz brightness temperatures images over the Laptev Sea (Russia) taken $\sim$23.6 hours apart. Inside the black rectangles is a feature that does not move over time. If $T_{53.6}$ is less than 242 K, then the pixel is assumed not to be precipitating.

Pixels with invalid or missing data from AMSU-A channels 1-12, and 15, and AMSU-B channels 2 to 5 are treated as potentially precipitating even though no retrieval will be done over them. Pixels where the altitude is higher than a latitude-dependent threshold $A(\Theta_{lat})$ are also treated as potentially precipitating (Θ_{lat} is in units of degrees and is defined to be positive for the northern hemisphere).

$$A(\Theta_{lat}) = \begin{cases} 2000 \text{ m} & \text{for } \|\Theta_{lat}\| < 60 \\ 1500 \text{ m} & \text{for } 60 \leq \Theta_{lat} < 70 \\ 500 \text{ m} & \text{otherwise} \end{cases} \tag{4.3}$$

These decisions minimize the likelihood that corrupt data will corrupt the computation of cloud-cleared brightness temperatures over pixels without corrupt data.

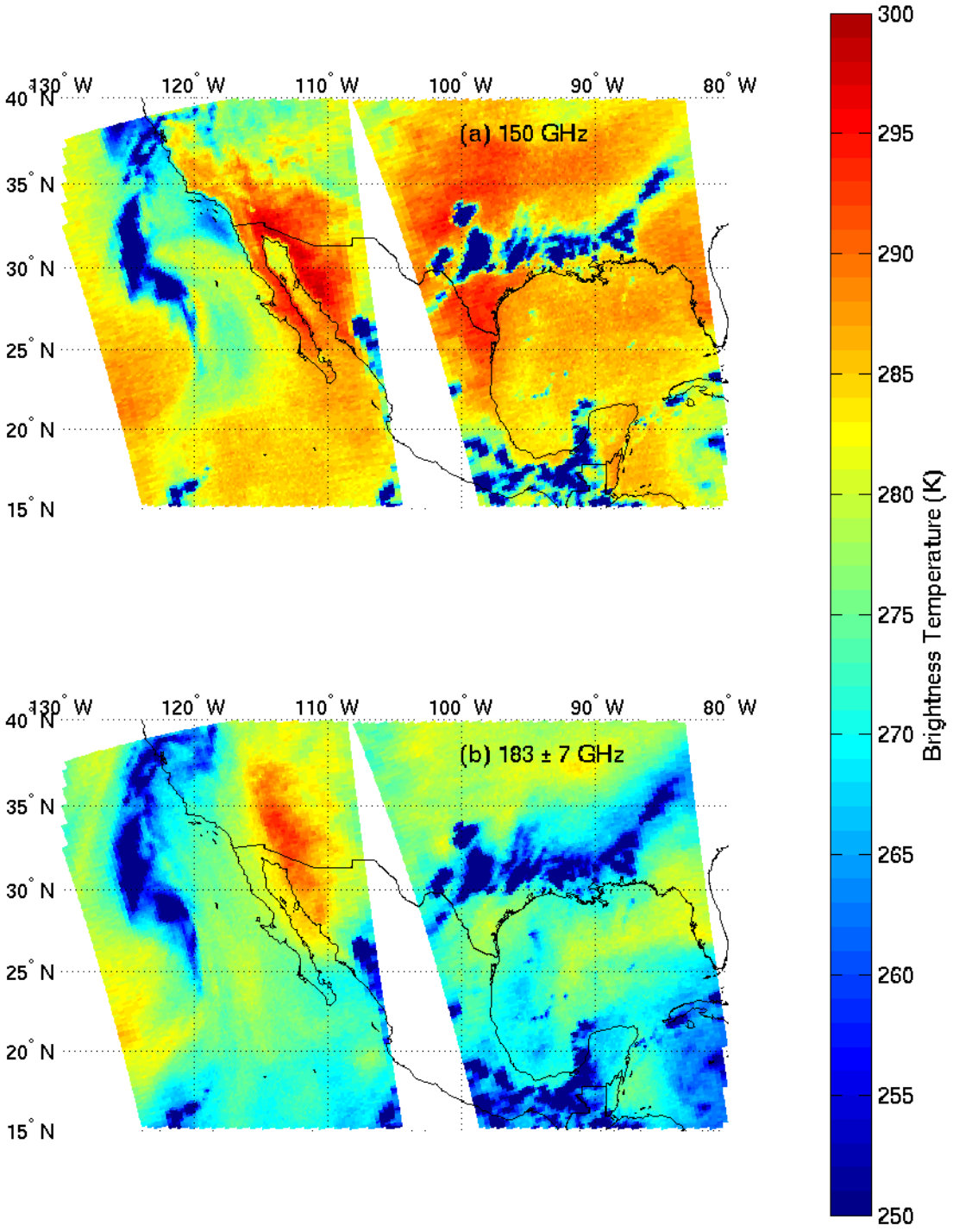

Figure 4-5: NOAA-15 AMSU-B brightness temperatures for northbound tracks on 13 Sept 2000 at (a) 150 GHz, and (b) 183 ± 7 GHz

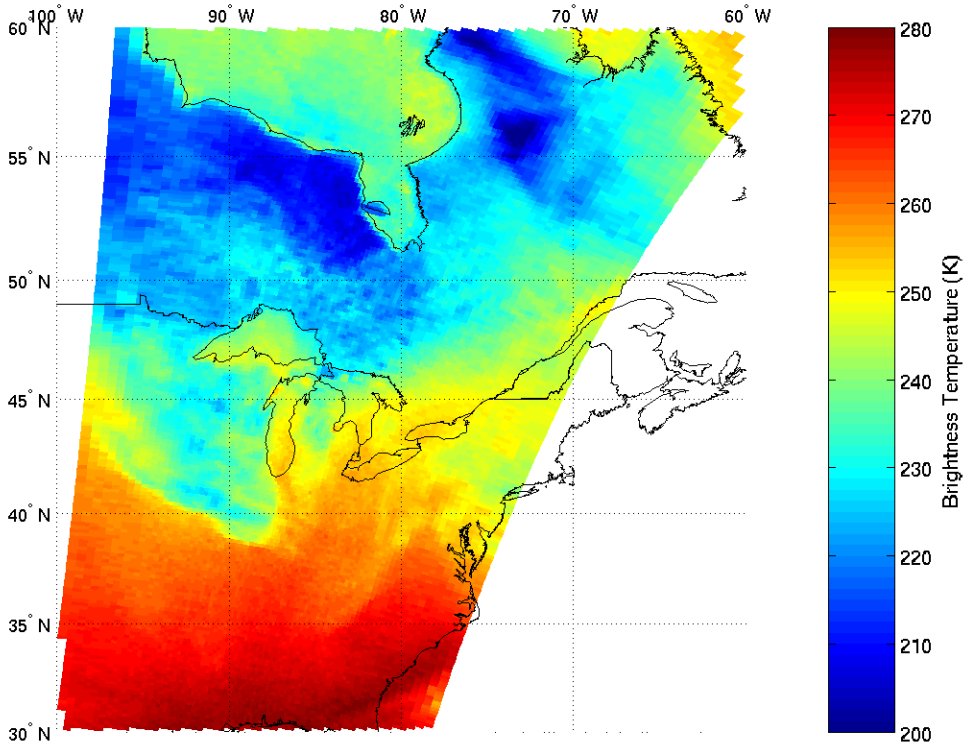

Figure 4-6: NOAA-15 AMSU-B 183 ± 7-GHz brightness temperatures, 20 Jan 2000, 1339 to 1349 UTC

Cloud-clearing is described in Sec. 4.2.3.

4.2.3 Cloud Clearing by Regional Laplacian Interpolation

This algorithm involves spatial processing of data, so the estimate at a pixel could depend not only on the information at that pixel but also on that in some surrounding pixels. This is useful for collecting information about the atmospheric conditions surrounding precipitating regions, such as temperature profile. Sec. 4.2.4 describes the use of temperature-profile principal components in the algorithm.

After the precipitation mask has been computed, it is used to filter the brightness temperature data so that the precipitation-induced signatures do not appear. It has been observed that in the absence of precipitating clouds and surface features, local

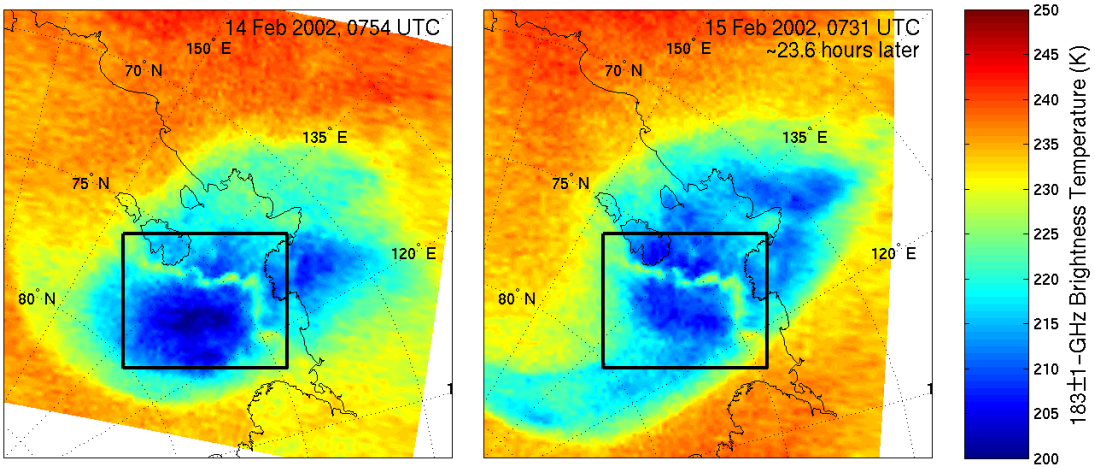

Figure 4-7: NOAA-15 AMSU-B 183 ± 1-GHz brightness temperatures over a dry hole on 14 Feb 2002, 0754 UTC (left), and 15 Feb 2002, 0731 UTC (right)

brightness temperature images approximately satisfy Laplace's equation:

$$\nabla^2 \Phi = 0 \tag{4.4}$$

where Φ is a scalar field (in this case brightness temperatures). This approximation appears to be reasonably valid for our purposes over distances of several hundred km. Precipitation-induced signatures from brightness temperature data are filtered out by forcing data within potentially precipitating regions to satisfy Laplace's equation given boundary conditions determined by the precipitation mask. An example of this is shown in Fig. 4-8. This technique was used in [24].

The Morphology of Precipitation

For each region, before Laplacian interpolation takes place, special processing may be required depending on the morphology and location of the region. For this thesis, pixels flagged as potentially precipitating are divided into disjoint, non-adjacent 4-connected regions[2]. The types of regions that this cloud clearing procedure could

[2] A *4-connected region* is a set of pixels with an ordering of all pixels (possibly with some repetition) such that each pair of consecutive pixels are adjacent vertically or horizontally. For an *8-connected region*, consecutive pixels can be vertically, horizontally, or diagonally adjacent.

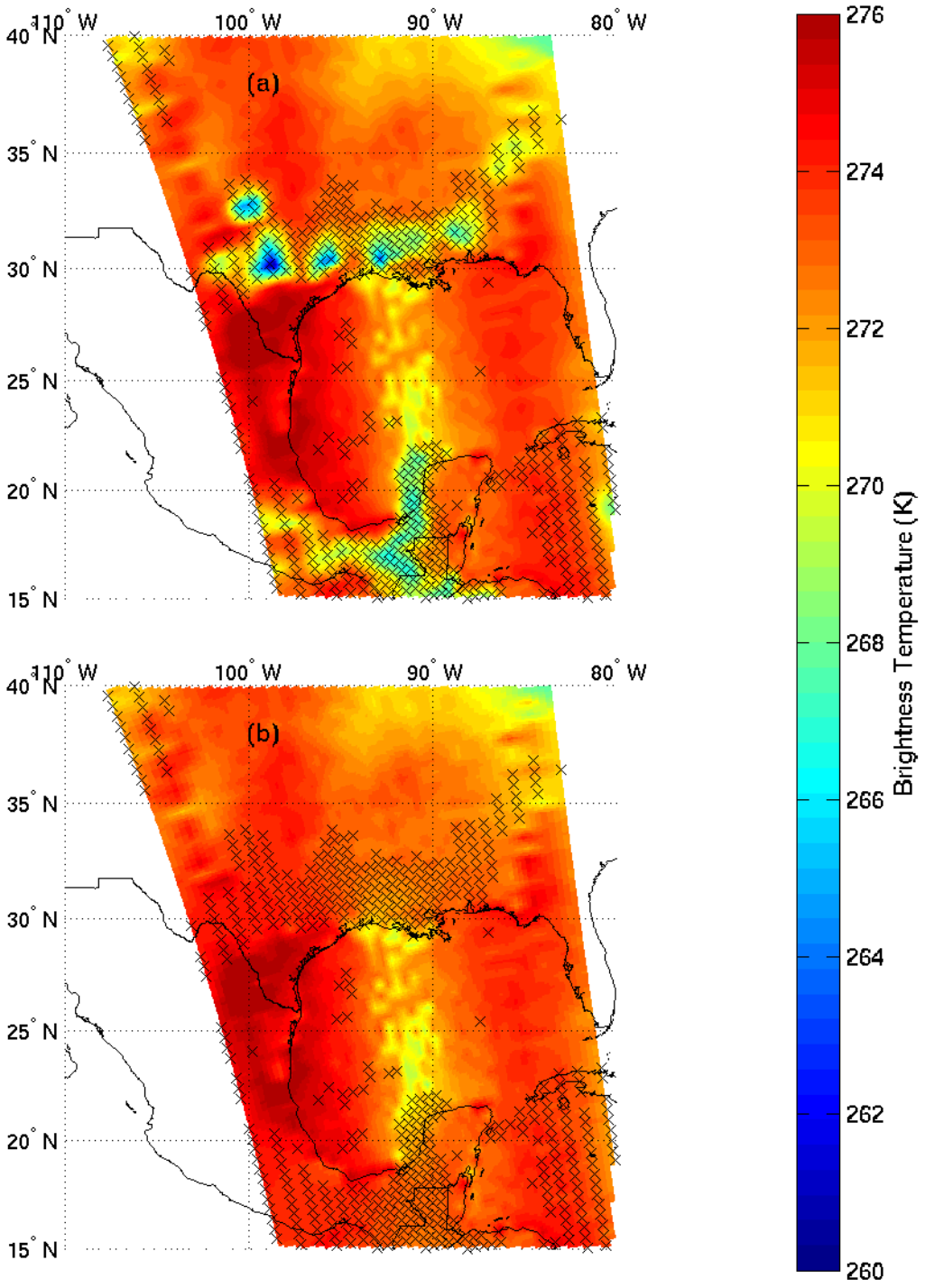

Figure 4-8: NOAA-15 AMSU-A 52.8-GHz brightness temperatures for a northbound track on 13 Sept 2000 (a) before cloud-clearing, and (b) after cloud-clearing using Laplacian interpolation. AMSU-A pixels within potentially precipitating regions are marked with x's.

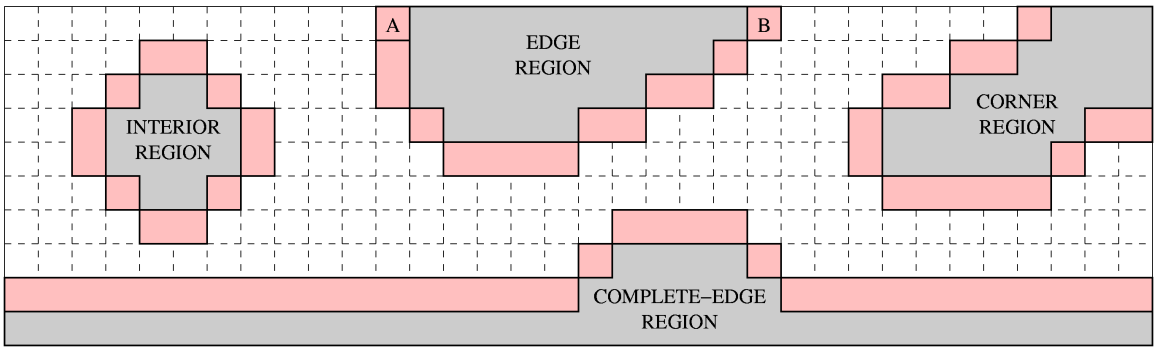

Figure 4-9: Types of regions encountered by the cloud clearing method. Boundary pixels are shaded in red.

encounter can be classified into these four types:

1. *Interior regions*, regions that do not include points at the edge nor the corners of the image being processed

2. *Edge regions*, regions that include points at the edge but not the corner of the image being processed

3. *Vertex regions* (or *corner regions*), regions that include points at any of the corners of the image but not an entire edge

4. *Complete-edge regions*, regions that include all of the pixels along one or more edges

These four types are illustrated in Fig. 4-9. The boundary pixels of each region are found by dilating by one pixel vertically and horizontally. Boundary pixels are not part of the flagged regions.

Interior regions do not require any special processing before Laplacian interpolation because their boundary points lie within the image.

Edge regions require extra steps in order to form a closed boundary over which Laplacian interpolation can be done. The brightness temperatures at pixels along the edge are linearly interpolated based on the boundary points that are at the edge. Then a new set of boundary points is formed that includes the first set of boundary

pixels and the portions of the edges in the edge region, and Laplacian interpolation is done over the edge region without the pixels on the edge using this set of boundary pixels. For example, for the edge region in Fig. 4-9 the cloud-cleared brightness temperatures for the pixels between pixels A and B are assumed to be the linearly interpolated brightness temperature based on those at A and B. Then, Laplacian interpolation is done using the boundary pixels of the edge region along with the pixels between A and B. Laplacian interpolation is not done over the pixels between A and B.

For this thesis, Laplacian interpolation was not done on corner regions. The convexity of the corner regions at corner points prevents interpolation of cloud-cleared brightness temperatures along the portions of the edges that include corner points. However, cloud-cleared brightness temperatures may be computed for some of the pixels in a corner region. A method for processing such regions is described in Appendix A and may be implemented in the future. The amount of precipitation that falls in corner regions is very small for data sets that are large enough. AMSU-A/B data sets typically cover one orbit ($\sim$ 770 AMSU-A scans). Aqua AMSU/HSB granules cover 45 AMSU-A scans, but consecutive granules can be concatenated to reduced the effect of ignoring precipitation in corner regions.

Complete-edge regions can occur when entire scans of data are invalid or missing. Laplacian interpolation can sometimes be done over portions of complete-edge regions. Contiguous sets of rows or contiguous sets of columns that include an edge are excluded from the interpolation process. In Fig. 4-10, the complete edge region becomes an edge region, and linear interpolation can be done on the pixels between pixels C and D before Laplacian interpolation. Some complete-edge regions will become corner regions and therefore will not yield any useful information because the current version of the algorithm ignores corner regions.

Channel-Specific Interpolation Masks

For AMSU-A channel 4 (52.8 GHz) the mask used to do Laplacian interpolation is the one resulting from the precipitation detection method. However, for AMSU-A

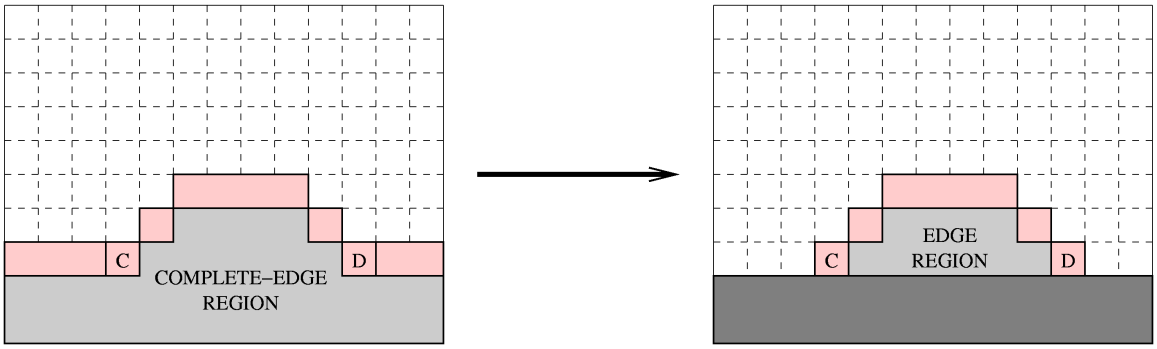

Figure 4-10: Salvaging pixels in a complete-edge region. Eliminating the bottom two rows of the image on the left leaves a portion that can be treated as an edge region.

channels 5-8, the mask used is slightly different. The points selected for Laplacian interpolation do not include those for which the magnitude of the perturbation in channel 4 is less than 1 K. At such pixels, the precipitation signature is assumed to be weak enough that it would not significantly perturb channels 5-8.

4.2.4 Temperature-Profile and Water-Vapor-Profile Principal Components

One important determinant of precipitation is the temperature profile. Warmer atmospheres can hold more water vapor and result in higher vertical updraft velocities. Therefore, inputs to the neural net in Fig. 4-1 should include some that have information about temperature profile. For each of AMSU-A channels 4 to 8, the brightness temperatures were corrected for limb and surface effects and then processed to eliminate precipitation signatures with the methods described in Secs. 4.2.1 to 4.2.3. The corrected brightness temperatures from all five of these channels could have been inputs to the neural net in Fig. 4-1, but it was determined that a more compact representation of these channels was sufficient. PCA was applied to these five channels, and the first three principal components were found to be sufficient for characterizing the temperature profile. Adding the fourth and fifth principal components did not significantly improve the training of the neural net.

Another important determinant of precipitation is the water vapor profile. Higher

concentrations of water vapor can result in higher precipitation rates. The water-vapor principal components are computed using AMSU-A channels 1, 2, 3, and 15, and the AMSU-B 150-, 183 ± 7-, 183 ± 3-, and 183 ± 1-GHz channels. Some of these channels are sensitive to surface variations. Therefore it is necessary to project the vector of these observations onto a subspace that is not significantly sensitive to surface variations. Constrained PCA, which was described in Sec. 3.1.2, was used to compute the water-vapor principal components. A set of pixels without precipitation and with different types of surfaces was selected to computed surface-sensitive eigenvectors using PCA. The surface-sensitive eigenvectors were determined by visual inspection of the pre-constraint principal components for correlation with surface features (e.g. land/sea boundaries). Then, a set of data that also included precipitation was selected. The observations over this set were projected onto a linear subspace that was orthogonal to the subspace spanned by the surface-sensitive eigenvectors. Then, PCA was done on the resulting data set in order to determine the water-vapor principal components. It was found that two water-vapor principal components were adequate for characterizing the eight channels.

4.2.5 Image Sharpening

15-km retrievals are useful. Because of the nonlinear relationship between precipitation and atmospheric conditions, data collected at 50-km resolution can miss or weakly detect smaller rain cells that contribute a significant amount of rainfall.

15-km retrievals require 15-km data. 54-GHz perturbations are calculated at 50-km. The information contained in such images might not be suitable for doing 15-km retrievals. A method for producing 15-km images of 54-GHz perturbations is needed. This step requires some image sharpening.

Within regions flagged as potentially precipitating, strong precipitation is generally characterized by cold cloud-induced perturbations of the AMSU-A tropospheric temperature sounding channels in the range 52.5-55.6 GHz. Examples of 183 ± 7-GHz data and the corresponding 50-km cold perturbations at 52.8 GHz are illustrated in Fig. 4-11(a) and (c). Physical considerations and aircraft data show that convective

cells near 54 GHz typically appear slightly off-center and less extended relative to the 183-GHz image [9, 27]. The small interpolation errors in converting 54-GHz perturbations to 15-km contribute to the total errors and discrepancies discussed in Sec. 4.4. These 50-km-resolution 52.8-GHz perturbations $\Delta T_{50;52.8}$ are then used to infer the perturbations $\Delta T_{15;52.8}$ (Fig. 4-11(d)) that might have been observed at 52.8 GHz with 15-km resolution had those perturbations been distributed spatially in the same way as the cold perturbations observed at either 183±7 or 183±3 GHz, the choice between these two channels being the same as described above. This requires the bilinearly interpolated 50-km AMSU data to be resampled at the HSB beam positions. 50-km perturbations in the 54-GHz band $\Delta T_{50;54}$ are sharpened to 15-km resolution $\Delta T_{15;54}$ by computing the value of $\Delta T_{15;54}$ that will make the ratio of the 15-km perturbation to the 50-km perturbation for the 54-GHz band equal to corresponding ratio for the 183-GHz band.

$$\frac{\Delta T_{15;54}}{\Delta T_{50;54}} = \frac{\Delta T_{15;183}}{\Delta T_{50;183}} \tag{4.5}$$

The perturbation near 183 GHz is defined to be the difference between the observed radiance and the appropriate threshold given by Eq. 4.1 or 4.2. The perturbation $\Delta T_{50;54}$ near 54 GHz is defined to be the difference between the observed radiance and the Laplacian-interpolated radiance based on those pixels surrounding the flagged region [82]. Any warm perturbations in the images of $\Delta T_{15;183}$ and $\Delta T_{50;54}$ are set to zero. Then, these inferred 15-km perturbations can be computed for five AMSU-A channels using the following formula

$$\Delta T_{15;54} = \frac{\Delta T_{15;183}}{\Delta T_{50;183}} \Delta T_{50;54} \tag{4.6}$$

To prevent this computation from becoming unstable, the hyperbolic tangent function is applied to the ratio of the 183-GHz perturbations.

$$\Delta T_{15;54} = 20 \tanh\left(\frac{\Delta T_{15;183}}{20\Delta T_{50;183}}\right) \Delta T_{50;54} \tag{4.7}$$

Given the filter used to filter $\Delta T_{15;183}$ to 50-km resolution, the ratio $\Delta T_{15;183}/\Delta T_{50;183}$

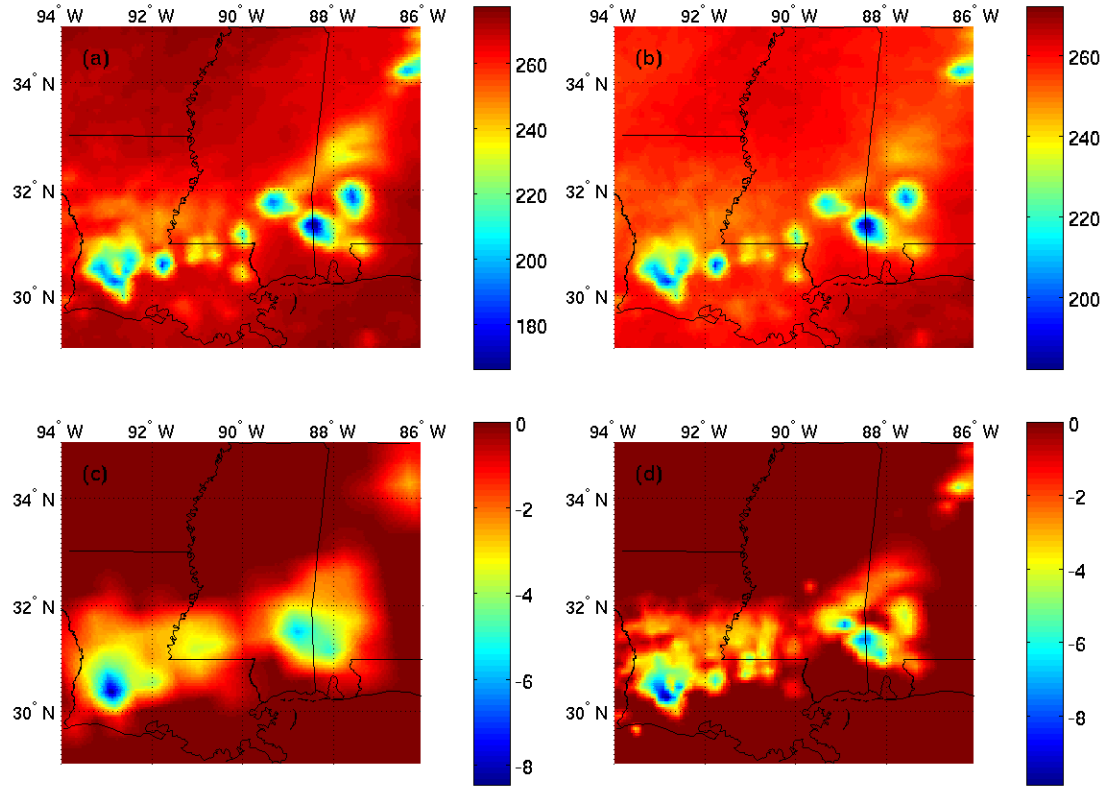

Figure 4-11: Frontal system on 13 Sept 2000, 0130 UTC. (a) Brightness temperatures (K) near 183 ± 7-GHz. (b) Brightness temperatures (K) near 183 ± 3-GHz. (c) Brightness temperature perturbations (K) near 52.8 GHz. (d) Inferred 15-km-resolution brightness temperature perturbations (K) near 52.8 GHz.

should not exceed 7.

Fig. 4-11 shows an example of image sharpening. Fig. 4-11(d) shows $\Delta T_{15;52.8}$ 50-km 52.8-GHz perturbations sharpened to 15-km resolution for a frontal system. Visually, this image appears to be appropriate for use in estimating 15-km precipitation rates.

4.3 Development of the Algorithm

The current AMSU/HSB precipitation retrieval algorithm is based on NOAA-15 AMSU-A/B comparisons with NEXRAD over the eastern United States during 38 or-

16 Oct 1999, 0030 UTC	30 Apr 2000, 1430 UTC
31 Oct 1999, 0130 UTC	14 May 2000, 0030 UTC
2 Nov 1999, 0045 UTC	19 May 2000, 0015 UTC
4 Dec 1999, 1445 UTC	19 May 2000, 0145 UTC
12 Dec 1999, 0100 UTC	20 May 2000, 0130 UTC
28 Jan 2000, 0200 UTC	25 May 2000, 0115 UTC
31 Jan 2000, 0045 UTC	10 Jun 2000, 0200 UTC
14 Feb 2000, 0045 UTC	16 Jun 2000, 0130 UTC
27 Feb 2000, 0045 UTC	30 Jun 2000, 0115 UTC
11 Mar 2000, 0100 UTC	4 Jul 2000, 0115 UTC
17 Mar 2000, 0015 UTC	15 Jul 2000, 0030 UTC
17 Mar 2000, 0200 UTC	1 Aug 2000, 0045 UTC
19 Mar 2000, 0115 UTC	8 Aug 2000, 0145 UTC
2 Apr 2000, 0100 UTC	18 Aug 2000, 0115 UTC
4 Apr 2000, 0015 UTC	23 Aug 2000, 1315 UTC
8 Apr 2000, 0030 UTC	23 Sep 2000, 1315 UTC
12 Apr 2000, 0045 UTC	5 Oct 2000, 0130 UTC
12 Apr 2000, 0215 UTC	6 Oct 2000, 0100 UTC
20 Apr 2000, 0100 UTC	14 Oct 2000, 0130 UTC

Table 4.2: List of rainy orbits used for training, validation, and testing

bits that exhibited significant precipitation and were distributed throughout the year. These orbits are listed in Table 4.2. The primary precipitation-rate retrieval products of AMSU/HSB are 15- and 50-km-resolution contiguous retrievals over the viewing positions of HSB and AMSU, respectively, within 43° of nadir. The two outermost 50-km and six outermost 15-km viewing positions on each side of the swath are omitted due to the potentially excessive limb effects at such angles. After the algorithm architectures for these two retrieval methods are presented below, the derivation of the numerical coefficients characterizing the neural network is described.

The neural net in Fig. 4-3 produces 15-km precipitation-rate estimates using the following inputs:

- Inferred 15-km perturbations at 52.8, 53.6, 54.4, 54.9, and 55.5 GHz (corresponding to AMSU-A channels 4, 5, 6, 7, and 8, respectively)

- 183 ± 1-, 183 ± 3-, and 183 ± 7-GHz 15-km HSB data

- Three principal components characterizing the original five corrected 50-km AMSU-A temperature radiances

- Surface-insensitive principal components that characterize the window channels at 23.8, 31.4, 50, and 89 GHz, plus the four HSB channels.

- $\sec\theta$

The relative insensitivity of these inputs to surface emissivity is important to the success of this technique over land, ice, and snow.

The statistical nature of precipitation must be adequately addressed during the training of the neural net. In addition to minimizing the RMS error between the estimated rain rate and the ground truth, one should also make sure that the estimator provides estimates that closely reflect the type of rain seen by the radiometer. Drizzle can have precipitation rates as low as 0.25 mm/h while tropical downpours can have rates as high as 200 mm/h [87]. Precipitation rates can have a lognormal distribution with a standard deviation that is at least twice the mean [46].

This network was trained to minimize the RMS value of the difference between the logarithms of the (AMSU + 1-mm/h) and (NEXRAD + 1-mm/h) retrievals; use of logarithms reduced the emphasis on the heaviest rain rates, which were roughly three orders of magnitude greater than the lightest rates. Adding 1 mm/h reduced the emphasis on the lightest rain rates which are more noise-dominated. These intuitive choices clearly impact the retrieval error distribution, and therefore further study should enable algorithm improvements. Retrievals with training optimized for low rain rates did not markedly improve that regime, however.

NEXRAD precipitation retrievals with 2-km resolution were smoothed to approximate Gaussian spatial averages that were centered on and approximated the view-angle-distorted 15- or 50-km antenna beam patterns. The accuracy of NEXRAD precipitation observations is known to vary with distance, so only points beyond 30 km but within 110 km of each NEXRAD radar site were included in the data used to train and test the neural nets.

Eighty different networks were trained using the Levenberg-Marquardt algorithm, each with different numbers of nodes and water-vapor principal components (Before experiments using water-vapor principal components were done, it had been determined that the leading three temperature-profile principal components were sufficient for characterizing the atmospheric temperature profile). A network with nearly the best performance over the testing dataset was chosen; it used two surface-blind water-vapor principal components, and only slightly better performance was achieved with five water-vapor principal components with increased surface sensitivity. The final network had one hidden layer with five nodes that used the tanh sigmoid function. These neural networks are similar to those described in [82]. The resulting 15-km-resolution precipitation retrievals are then smoothed to yield 50-km retrievals.

The 15-km retrieval neural network was trained using precipitation data from the 38 orbits listed in Table 4.2. During this period the radio interference to AMSU-B was negligible relative to other sources of retrieval error. Each 15-km pixel flagged as potentially precipitating using 183 ± 7- or 183 ± 3-GHz radiances (see Figs. 4-2 and 4-3) was used either for training, validation, or testing of the neural network. For these 38 orbits over the United States, 15,160 15-km pixels were flagged and considered suitable for training, validation, and testing. Half were used for training, and one quarter were used for each of validation and testing, where the validation pixels were used to determine when the training of the neural network should cease. Based on the final AMSU and NEXRAD 15-km retrievals, approximately 14 and 38%, respectively, of the flagged 15-km pixels appear to have been precipitating less than 0.1 mm/h for the test set.

4.4 Retrieval Performance Evaluation

This section presents three forms of evaluation for this initial precipitation-rate retrieval algorithm:

- Representative qualitative comparisons of AMSU and NEXRAD precipitation-rate images

- Quantitative comparisons of AMSU and NEXRAD retrievals stratified by NEXRAD rain rate

- Representative precipitation images at more extreme latitudes beyond the NEXRAD training zone

4.4.1 Image Comparisons of NEXRAD and AMSU/HSB

Each NEXRAD comparison at 15-km resolution occurred within 8 min of a satellite overpass; such coincidence is needed to characterize single-pixel retrievals because convective precipitation evolves rapidly on this spatial scale. Although comparison with instruments such as TRMM and SSM/I would be useful, their orbits unfortunately overlap those of AMSU within 8 min so infrequently (if ever) that comparisons over precipitation will be too rare to be useful until several years of data have been analyzed. This challenge of simultaneity and the sporadic character of rain have restricted most prior instrument comparisons (passive microwave satellites, radar, rain gauges) to dimensions over 100 km and to periods of an hour to a month [1, 2]. The uniformity and extent of the NEXRAD network offer a unique degree of simultaneity on 15- and 50-km scales and even the ability to match the Gaussian shape of the AMSU antenna beams.

Although these AMSU/HSB-NEXRAD comparisons are encouraging because they involve single pixels and independent physics and facilities, further extensive analyzes are required for real validation. For example, comparisons of precipitation averages and differences over the same time/space units used to validate other precipitation measurement systems (e.g., SSM/I [20], ATOVS, TRMM, rain gauges) will be needed to characterize variances and systematic biases based on precipitation rate, type, location, or season. These biases will include any present in the NEXRAD data used to train the AMSU/HSB algorithm; once characterized, they can be diminished. Any excess variance experienced for rain cells too small to be resolved by AMSU/HSB can also eventually be better characterized, although it is believed to be modest for cells with microwave signatures larger than 10 km. Smaller isolated cells contribute

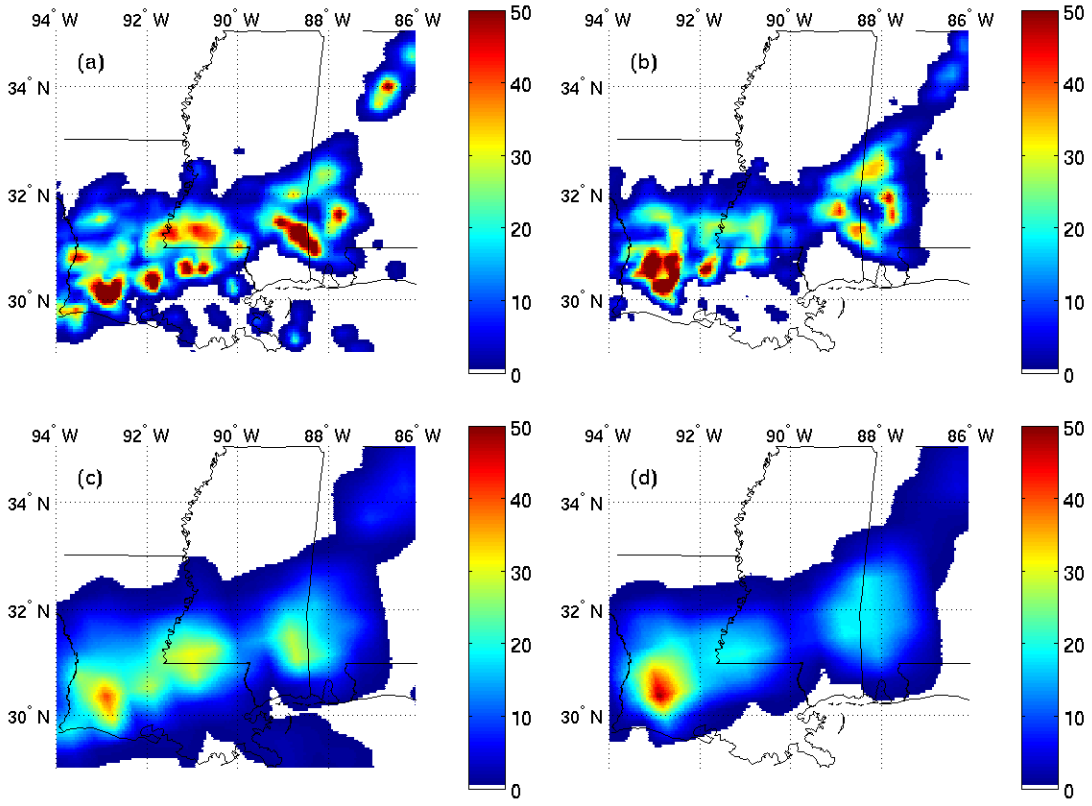

Figure 4-12: Precipitation rates (mm/h) above 0.5 mm/h observed on 13 Sept 2000, 0130 UTC. (a) 15-km-resolution NEXRAD retrievals, (b) 15-km-resolution AMSU retrievals, (c) 50-km-resolution NEXRAD retrievals, and (d) 50-km-resolution AMSU retrievals.

little to total rainfall. Sec. 6.1 presents an attempt to improve the estimator through comparisons with AMSR-E rain rate estimates.

Fig. 4-12(a) and (b) presents 15-km-resolution precipitation retrieval images for September 13, 2000 obtained from NEXRAD and AMSU, respectively. On this occasion, both sensors yield rain rates over 50 mm/h at similar locations and lower rain rates down to 0.5 mm/h over comparable areas. The revealed morphology is thus very similar even though AMSU observes 6 min before NEXRAD, and they sense altitudes that may be separated by several kilometers; rain falling at a nominal rate of 10 m/s takes 10 min to fall 6 km.

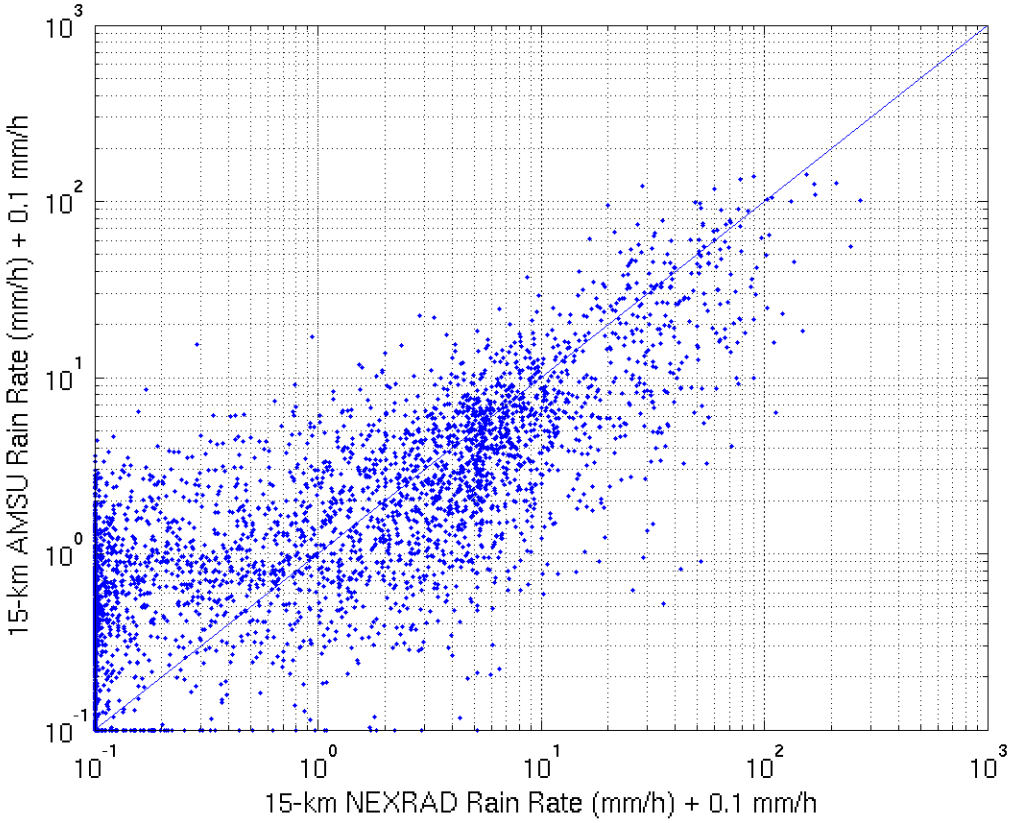

Figure 4-13: Comparison of AMSU and NEXRAD estimates of rain rate at 15-km resolution.

4.4.2 Numerical Comparisons of NEXRAD and AMSU/HSB Retrievals

Fig. 4-13 shows the scatter between the 15-km AMSU and NEXRAD rain-rate retrievals for the test pixels not used for training or validation. Fig. 4-14 shows the scatter between the 50-km AMSU and NEXRAD rain-rate retrievals over all points flagged as precipitating.

The relative sensitivity of AMSU and NEXRAD to light and heavy rain can be seen from Fig. 4-14. In general, these figures suggest that AMSU responds less to the highest radar rain rates, perhaps because AMSU is less sensitive to the bright-band or hail anomalies that affect radar. They also suggest the risk of false rain detections increases for AMSU retrievals below 0.5 mm/h at 50-km resolution, although further

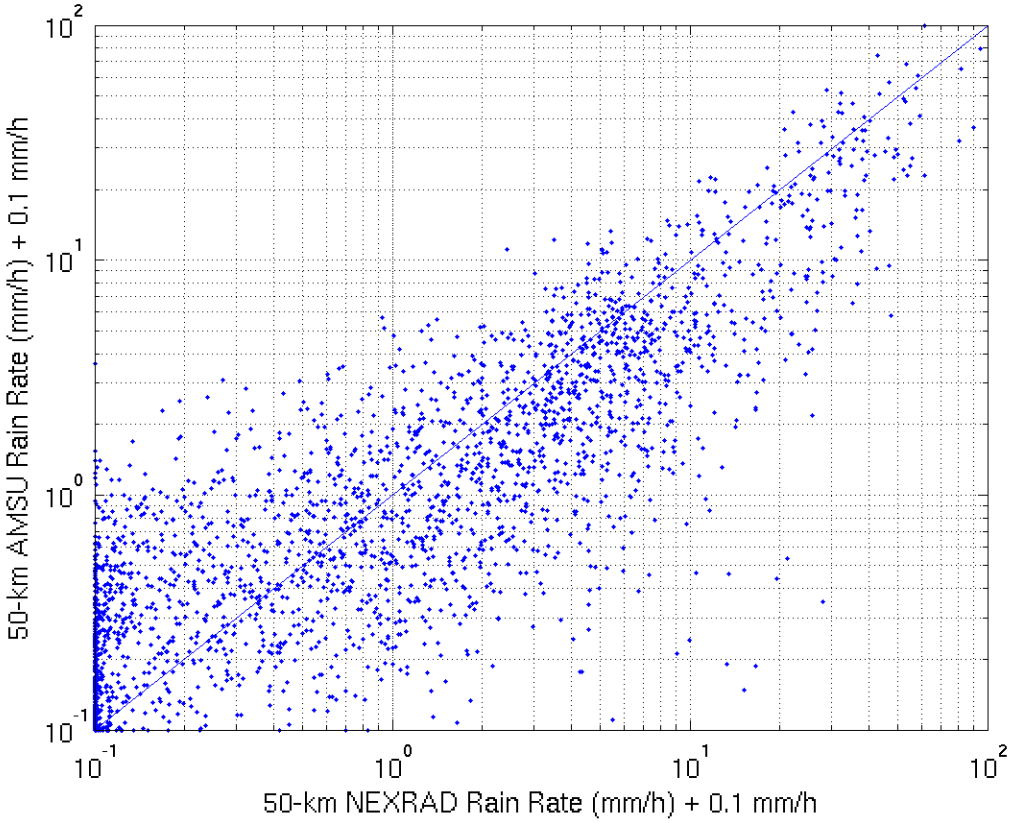

Figure 4-14: Comparison of AMSU and NEXRAD estimates of rain rate at 50-km resolution.

study will be required. Greater accuracy at these low rates will require more space-time averaging and careful calibration. The risk of overestimating rain rate also appears to be limited. Only 3.3% of the total AMSU-derived rainfall was in areas where AMSU saw more than 1 mm/h and NEXRAD saw less than 1 mm/h. Only 7.6% of the total NEXRAD-derived rainfall was in areas where NEXRAD saw more than 1 mm/h and AMSU saw less than 1 mm/h. These percentages can be compared to the total percentages of AMSU and NEXRAD rain that fell at rates above 1 mm/h, which are 94 and 97, respectively. It is also interesting to see to what degree each sensor retrieves rain when the other does not, and how much rain each sensor misses. For example, of the 73 NEXRAD 15-km rain rate retrievals in Fig. 4-13 above 54 mm/h, none were found by AMSU to be below 3 mm/h, and of the 61 AMSU 15-km retrievals above 45 mm/h, none were found by NEXRAD to be below 16 mm/h. Also,

NEXRAD range	15-km resolution		50-km resolution	
	30-110 km	110-230 km	30-110 km	110-230 km
< 0.5 mm/h	1.0	1.4	0.5	0.5
0.5-1 mm/h	2.0	2.6	0.9	1.1
1-2 mm/h	2.3	2.7	1.1	1.5
2-4 mm/h	2.7	3.9	1.8	2.3
4-8 mm/h	3.5	7.4	3.2	5.2
8-16 mm/h	6.9	8.4	6.6	6.5
16-32 mm/h	19.0	17.2	12.9	14.6
> 32 mm/h	42.9	39.2	22.1	21.7

Table 4.3: RMS AMSU/NEXRAD discrepancies (mm/h) at 15-km and 50-km resolution for pixels in the ranges 30-110 km and 110-230 km of NEXRAD radar sites

of the 69 NEXRAD 50-km rain rate retrievals in Fig. 4-14 above 30 mm/h, none were found by AMSU to be below 5 mm/h, and of the 102 AMSU 50-km retrievals above 16 mm/h, none were found by NEXRAD to be below 10 mm/h.

Perhaps the most significant AMSU precipitation performance metric is the RMS difference between the NEXRAD and AMSU rain rate retrievals; these are calculated for AMSU and HSB pixels that are flagged as potentially precipitating and do not have corrupted data. The pixels are grouped by retrieved NEXRAD rain rates in octaves. Only pixels that were from the central 26 AMSU-A scan angles and central 78 AMSU-B scan angles and were from regions between 30 and 110 km of any NEXRAD radar site were included in these evaluations; only the outermost two AMSU-A angles on each side were omitted. These comparisons used all 50-km pixels and only those 15-km pixels not used for training or validation. The results are listed in Table 4.3. The smoothing of the 15-km NEXRAD and AMSU results to nominal 50-km resolution was consistent with an AMSU-A Gaussian beamwidth of 3.33°.

The RMS agreement between these two very different precipitation-rate sensors appears surprisingly good, particularly since a single AMSU neural network is used over all angles, seasons, and latitudes. The 3-GHz radar retrievals respond most strongly to the largest hydrometeors, especially those below the bright band near the freezing level, while AMSU interacts with the general population of hydrometeors in the top few kilometers of the precipitation cell, which may lie several kilometers

above the freezing level. Much of the agreement between AMSU and NEXRAD rain-rate retrievals must therefore result from the statistical consistency of the relations between rain rate and its various electromagnetic signatures. It is difficult to say how much of the observed discrepancy is due to each sensor or to say how well each correlates with precipitation reaching the ground.

This study furthermore provided an opportunity for evaluation of radar data. The RMS discrepancies between AMSU and NEXRAD retrievals were separately calculated over all points at ranges from 110-230 km from any radar. For NEXRAD precipitation rates below 16 mm/h, these rms discrepancies were approximately 40% greater than those computed for test points at 30-110-km range. At rain rates greater than 16 mm/h, the accuracies beyond 110 km were more comparable (Table 4.3). The NEXRAD radar beams that are directed at angles farthest from zenith may miss some low-altitude precipitation for regions further than 110 km away from any NEXRAD site due to factors such as curvature of the earth's surface and surface-based obstructions (e.g. mountains). However, these beams are still able to sense heavy precipitation at high altitudes over the same regions. Most points in the eastern U.S. are more than 110 km from any NEXRAD radar site, and radar is even more sparse in the western half.

4.4.3 Global Retrievals of Rain and Snow

One of the principal Aqua validation activities involves testing and tuning of the precipitation retrievals for climates not well represented in the NEXRAD training dataset. Fig. 4-15 illustrates precipitation-rate retrievals at points around the globe where radar confirmation data is scarce. Fig. 4-15(a) shows precipitation retrievals in the tropics over a mix of land and sea, while Fig. 4-15(b) shows a more intense tropical event. Fig. 4-15(c) illustrates strong precipitation near 72° to 74° N, again over both land and sea. Finally, Fig. 4-15(d) illustrates the March 5, 2001 New England snowstorm that deposited roughly a foot of snow within a few hours: an accumulation somewhat greater than is indicated by the retrieved rain rates of 1.2 mm/h. This applicability of the algorithm to snowfall rate should be expected because

the observed radio emission originates exclusively at high altitudes. Whether the hydrometeors are rain or snow upon impact depends only on air temperatures near the surface, far below those altitudes being probed. For essentially all of the pixels shown in Fig. 4-15, the adjacent clear air exhibited temperature and humidity profiles (inferred from AMSU) within the range of the training set. Nonetheless regional biases are expected and will require evaluation. For example, polar stratiform precipitation is expected to exhibit relatively weaker radiometric signatures in winter when the temperature lapse rates are lower, and snow-covered mountains in cold polar air can produce false detections.

Snow will be further discussed in Chapter 5.

4.5 Post-Development Changes to the Algorithm

Since the development described in this chapter, the following change has been made to the algorithm: In Sec. 4.2.2, the 183 ± 7-GHz channel is not used to detect precipitation if $T_{53.6}$ is less than 248 K. This has been changed to 249 K. Other changes have been made but do not affect the results in this chapter. Such changes have already been incorporated into the previous sections of this chapter. The results presented in the remainder of this thesis reflect these changes.

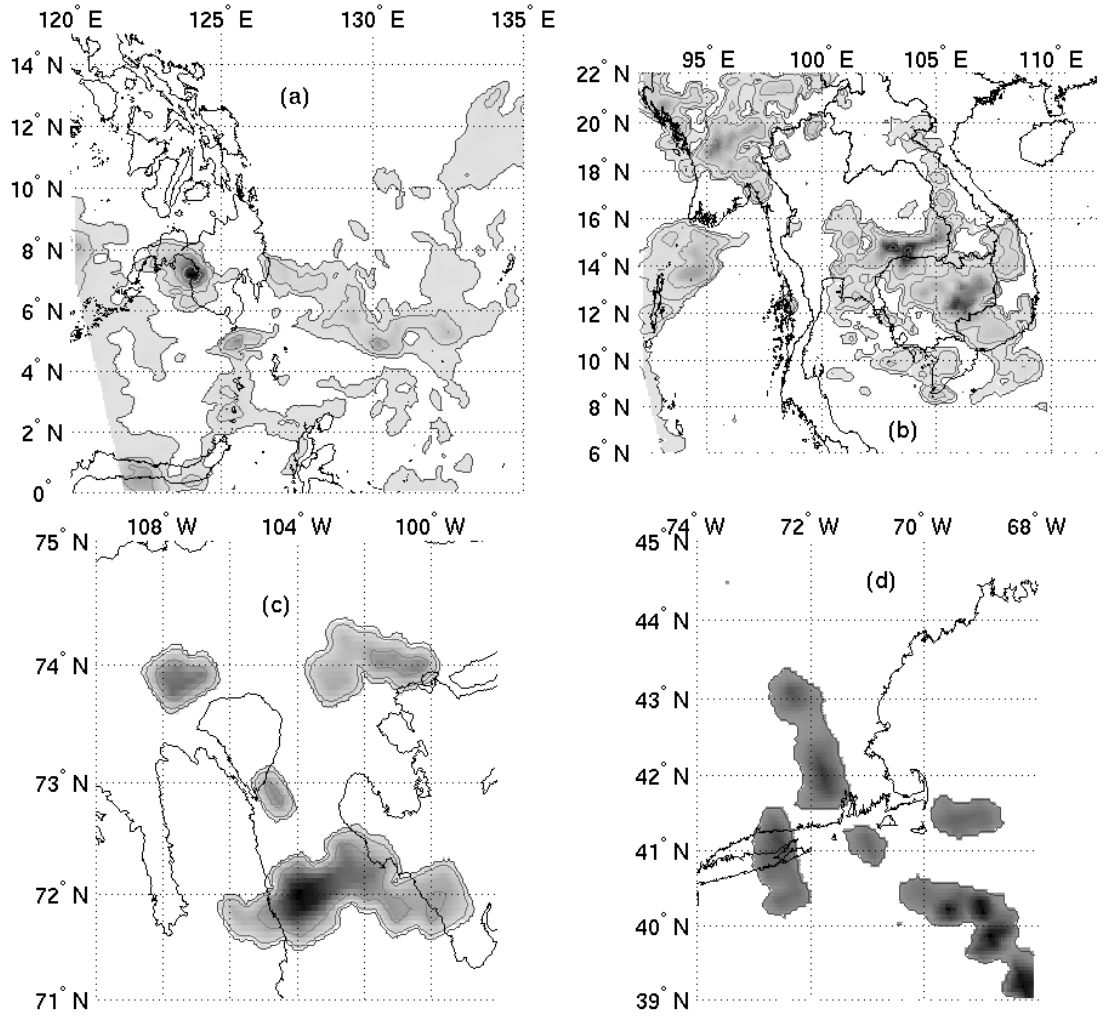

Figure 4-15: AMSU precipitation-rate retrievals (mm/h) with 15-km resolution. (a) Philippines, April 16, 2000, (b) Indochina, July 5, 2000, (c) Canada, August 2, 2000, and (d) New England snowstorm, March 5, 2001. Precipitation rate retrievals exceed 0.5 mm/h in the shaded regions, and contours are drawn for 0.5, 2, 8, 32, and 128 mm/h. The peak retrieved values are 47, 143, 30, and 1.5 mm/h in (a), (b), (c), and (d), respectively.

Chapter 5

Snow and Polar Precipitation

This chapter[1] discusses the remote sensing of snow and polar precipitation using AMSU.

During the course of the research presented in this thesis, AMSU demonstrated the ability to detect not only tropical and mid-latitude rain, but also mid-latitude snow and polar precipitation (Fig. 4-15(d)). AMSU's sensitivity to snow is not surprising because whether precipitation falls as rain or snow depends more on the temperature near the surface of the earth than on the hydrometeors aloft observed by AMSU, which indicate precipitation rate [18, 19]. Other studies also have shown that AMSU is useful for detecting and estimating snow [47, 48, 77, 78]. The algorithm in Chapter 4 is therefore expected to be useful for estimating snowfall rates.

There are several non-definitive ways to detect polar precipitation:

- Morphological evolution over consecutive overpasses
- Motion over consecutive overpasses
- Cold spots in the 54-GHz and 183-GHz bands; spectral characteristics
- Lack of correlation with surface features

[1]Permission has been granted by the IEEE to include material from the following paper: F.W. Chen, A.M. Leckman, and D.H. Staelin, "Passive Microwave Signatures of Arctic Snowstorms Observed from Satellites," *Proceedings of the 2003 IEEE International Geoscience and Remote Sensing Symposium*, vol. 5, pp. 3139-3141, July 2003.

- Sharp features

The NOAA-15, NOAA-16, NOAA-17, and Aqua satellites each pass over the polar regions about once every 100 minutes, so certain regions in the Arctic and Antarctic Circle might be observed up to 15 times a day by a single satellite.

5.1 Examples of Polar Precipitation

5.1.1 Example 1

Fig. 5-1(b) shows an image of brightness temperatures near 183 ± 7-GHz for a polar precipitation event around 71° N, 60° E observed on July 1, 2002. The blue precipitation event ($\sim$ 225 K) is centered on a long east-west ridge of moist air ($\sim$ 260 K). Such 183±7-GHz images are the primary means for detecting potentially precipitating locations. In cold dry atmospheres, however, the 183 ± 7-GHz channel can be sensitive to surface variations. Therefore it is then necessary to check a window-channel brightness temperature image for correlations with surface features. Fig. 5-1(a) shows the 150-GHz image and regions of land ice/snow ($\sim$ 230 K), sea or sea ice ($\sim$ 240 K), moist air over land ($>\sim$ 270 K), and moist air over ocean ($\sim$ 260 K). Since this precipitation event has brightness temperatures below 240 K at 150, 183 ± 7, and 183 ± 3 GHz, this is consistent with the hypothesis that the signature arises from ice/scattering layers above any significant absorption by water vapor. Thus it is reasonable to conclude that the event around 71° N, 60° E is polar precipitation and not a transparent dry pocket of air over a reflective surface.

5.1.2 Example 2

Fig. 5-2(a) shows a 150-GHz image of a polar precipitation event that extends eastward from around 74° N, 10° W to around 74° N, 3° W, and from there extends southward to around 69° N, 3° W. Fig. 5-2(b) shows the corresponding 183 ± 7-GHz image. The cold spots appearing in the 183 ± 7-GHz image are surrounded by water vapor which appears as warm areas (relative to ocean) in the 150-GHz image. The

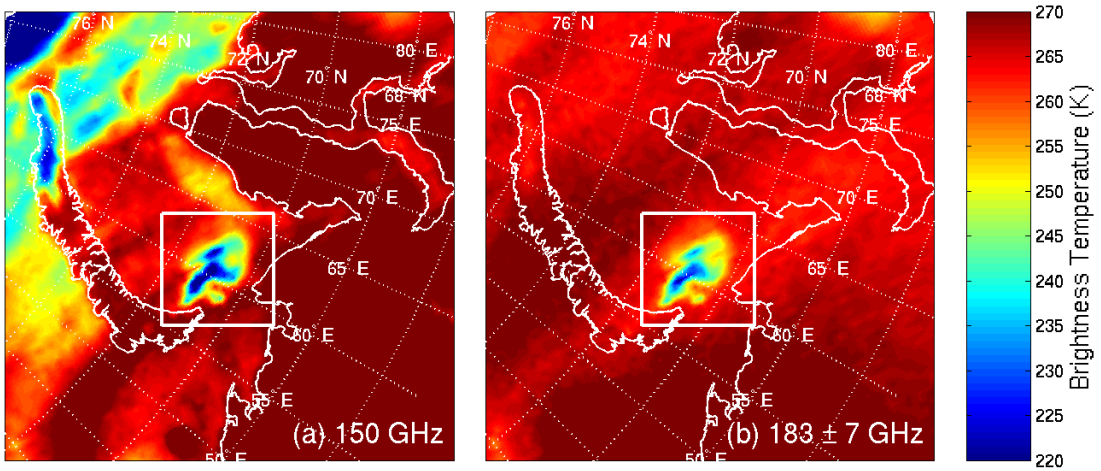

Figure 5-1: NOAA-16 AMSU-B data over the Kara Sea (Northern Russia) on 1 July 2002, 0005 to 0008 UTC, at (a) 150 GHz and (b) 183 ± 7 GHz.

presence of water vapor suggests that the cold spots are the result of presence of precipitation.

5.1.3 Example 3

Fig. 5-3 shows precipitation rate estimates for four consecutive observations inside the Arctic Circle at ∼100-minute intervals on July 20, 2002. The four images in this figure show the evolution of a precipitation system about 200 km wide and 1000 km long with features moving as fast as 100 km/h.

Additional evidence that these images reveal precipitation can be seen in radiometric data from specific channels. For example, in regions seen as precipitating in Fig. 5-3, the 52.8-GHz brightness temperature image exhibits perturbations that cannot be the result of surface features and that suggest convective activity within the cores of some storms (Fig. 5-4). The blue spots in Fig. 5-4 that are not in areas seen as precipitating in Fig. 5-3 are the result of high-elevation regions (Eq. 4.3). Finally, numerical weather predictions of precipitation rate using the MM5 model and initialized with analysis fields produced by the European Center for Medium-Range Weather Forecasting (ECMWF) [5] exhibited excellent morphological agreement with

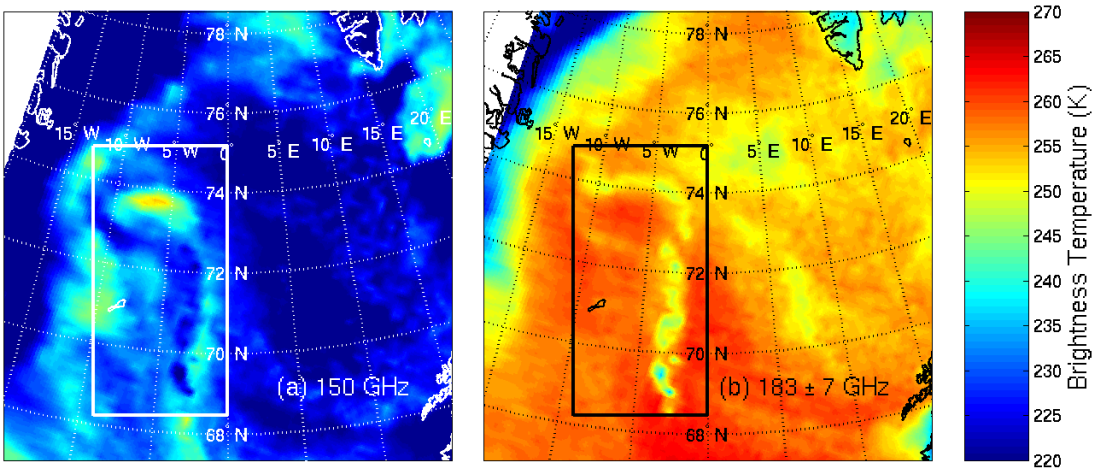

Figure 5-2: NOAA-15 AMSU-B data over the Greenland Sea on 1 Jan 2002, 0816 to 0819 UTC, at (a) 150 GHz and (b) 183 ± 7 GHz.

these microwave observations over several hours as the storm evolved (Figs. 5-3(a) and 5-5). As a result, it can be concluded that the signatures revealed by the observed brightness temperature spectrum are indeed associated with precipitation and are not, for example, due to patches of dry air that reveal low microwave emissivity surfaces. This sort of agreement between numerical predictions and AMSU-based retrievals have been obtained for several polar precipitation examples [5].

5.2 Weaknesses of the Algorithm

The algorithm used in this study was trained using data from the eastern U.S. and has yet to be calibrated for Arctic climates. As a result, it does not produce accurate estimates of rain rate in Arctic conditions. In Fig. 5-3(a), the estimated rain rates from AMSU reached 20 mm/h and much larger than the corresponding rates of ~ 1 mm/h predicted in Fig. 5-5. Typical Arctic temperature and water vapor profiles are not able to yield such high rain rates.

Franquet has done comparisons of AMSU-based precipitation-rate estimates using the algorithm developed for this thesis and estimates from BALTRAD, a ground-based radar network that provides coverage over areas surrouding the Baltic Sea.

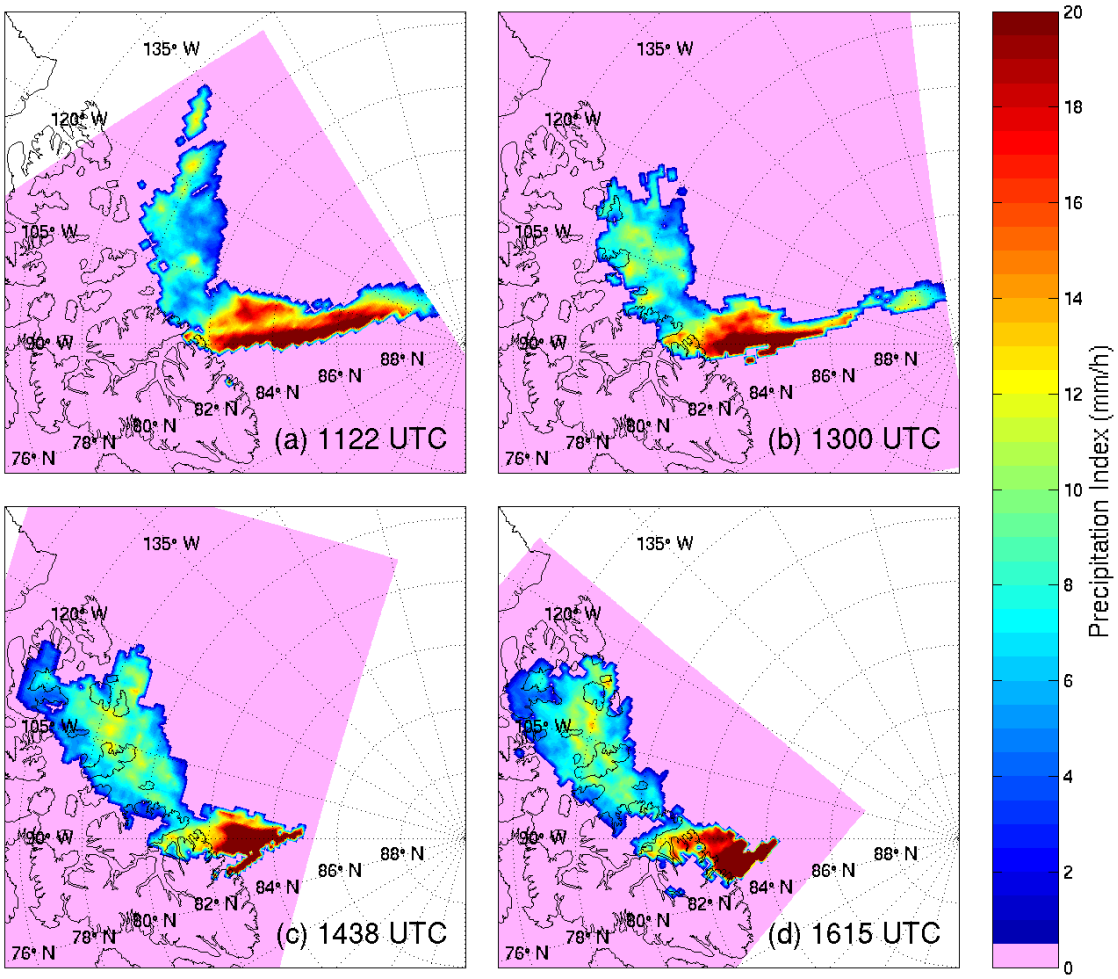

Figure 5-3: Aqua AMSU/HSB rain rate retrievals for four consecutive overpasses by Aqua on 20 July 2002 around (a) 1122 UTC, (b) 1300 UTC, (c) 1438 UTC, and (d) 1615 UTC

AMSU-based estimates tended to be greater than BALTRAD estimates by a factor of ∼5 in the summer while BALTRAD estimates tended to be greater by a factor of ∼3 in the winter [23].

Tuning of the algorithm for other climates is discussed in Chapter 6.1.

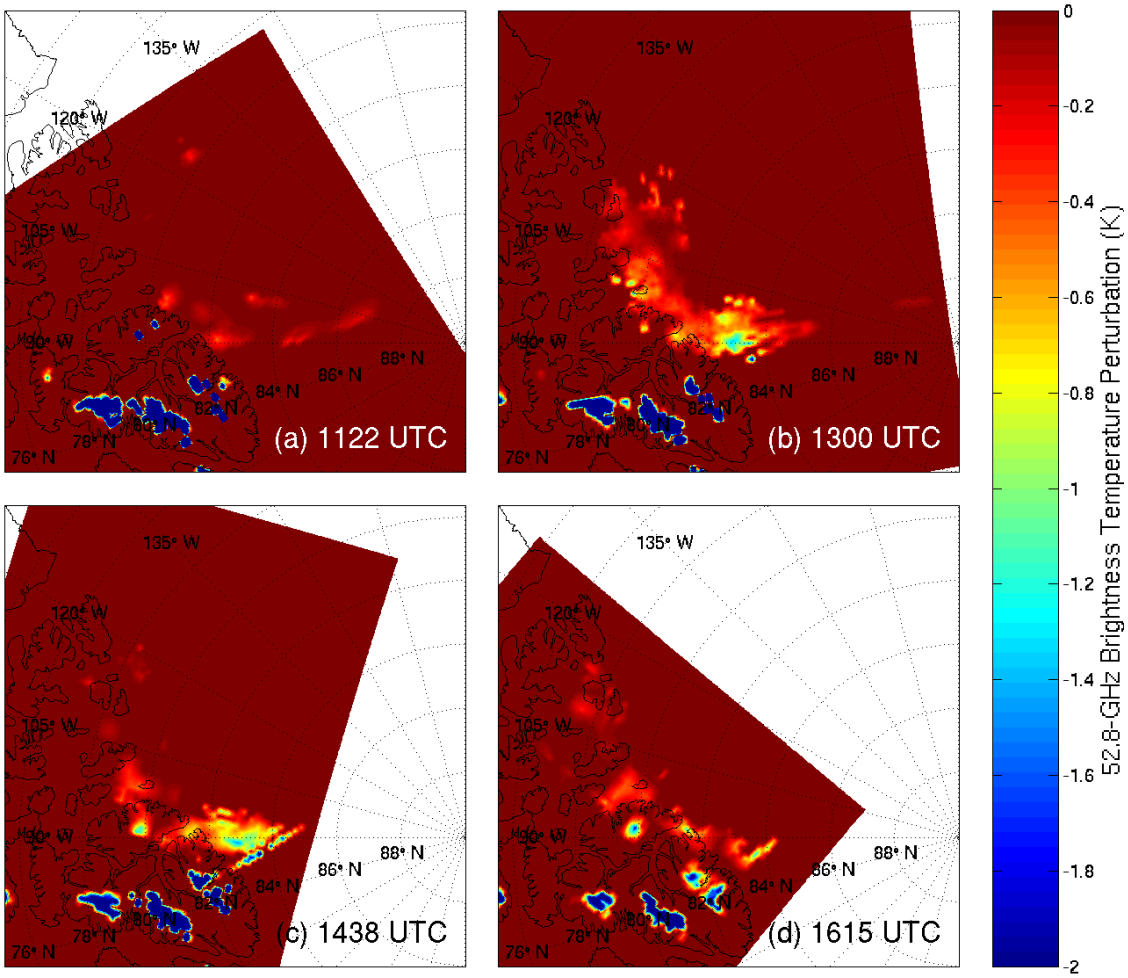

Figure 5-4: Aqua AMSU/HSB precipitation-induced perturbations in the 52.8-GHz channel for four consecutive overpasses by Aqua on 20 July 2002 around (a) 1122 UTC, (b) 1300 UTC, (c) 1438 UTC, and (d) 1615 UTC. The perturbations seen near 75° W are likely to be the result of surface effects

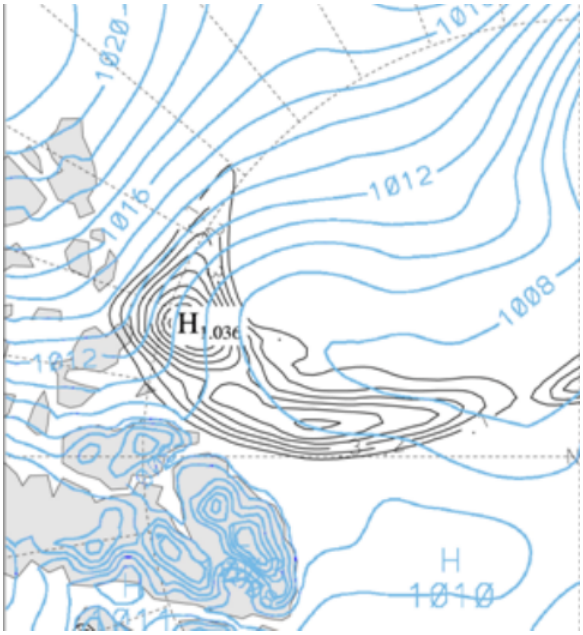

Figure 5-5: MM5 prediction of rain rate (mm/h), 20 July 2002, 1000-1100 UTC. The blue curves over ocean are pressure (mbar) contours, and the black curves are precipitation (mm/h) contours. Precipitation contours are drawn for multiples of 0.1 mm/h. Peak rain rate is ∼1 mm/h. (This image was provided by L. Bai and D.H. Bromwich)

Chapter 6

Precipitation Climatology

In this chapter, the precipitation algorithm developed for this thesis is used to produce climatological results. Such results are useful for getting a sense of the types of climatological variations that can be observed by the algorithm and for validating the algorithm.

6.1 Climatology-Based Correction of the Algorithm

The algorithm was trained on NEXRAD data over the eastern U.S. Because of the geographical limitations of the training data, it will not necessarily be able to produce good estimates globally. Chapter 5 showed the possibility that the algorithm can yield impossibly high rain rates for polar climates.

However, the algorithm can be adjusted using rain rates from another instrument. AMSU/HSB and AMSR-E[1] are both aboard the Aqua satellite and they observe nearly the same regions and at nearly the same times. AMSR-E has a slightly smaller swath width than AMSU/HSB. Therefore, AMSU/HSB and AMSR-E would be a very good pair of independent instruments for adjusting the algorithm.

The adjustment involves training a neural net to estimate a multiplicative correction factor. The correction factor should vary much more slowly than rain rates.

[1]AMSR-E rain rate retrievals were provided by Remote Sensing Systems, Inc., of Santa Rosa, CA (http://www.remss.com/). These rain rate retrievals were computed using a method based on that described in [90].

Therefore, it is best to train the neural net using inputs that vary slowly. Also, the AMSU/HSB rain rate cannot be an input to the neural net because the neural net would be applied to 15-km data while having been trained using data with a coarser resolution. The neural net cannot be trained to estimate AMSR-E rain rates because the range of the outputs of the neural net could be limited by the range of AMSR-E data. The neural net was trained using data averaged over $5^\circ \times 5^\circ$ boxes. The inputs were latitude and temperature-profile principal components. Metrics describing the day of year could have been used as inputs but were not because of the seasonal limitations of the training data. Such inputs may help the neural net learn the seasonal variation of precipitation rate.

The neural net was trained using data from 114 days from 20 August 2002 to 31 January 2003. HSB failed in early February 2003. Only $5^\circ \times 5^\circ$ boxes for which the AMSU/HSB rain rate $\hat{r}_{AMSU,5^\circ}$ was greater than 0.1 mm/h were used for training. The training, validation, and testing sets each had 3579 boxes. Let $r_{AMSR-E,5^\circ}$ be the $5^\circ \times 5^\circ$ AMSR-E rain rates. All of the data were from boxes entirely over ocean since the provided AMSR-E rain rates did not include any for land. The neural net was trained to estimate the $\log_{10}(r_{AMSR-E,5^\circ}/\hat{r}_{AMSU,5^\circ} + 0.1)$.

The neural nets trained have the same structure as that shown in Fig. 3-2, with one hidden layer of nodes with hyperbolic tangent transfer functions followed by a single output node with a linear transfer function. 72 neural nets were trained. Each neural net had 1, 2, or 3 hidden nodes, and used 1, 2, or 3 temperature-profile principal components. The testing set was divided according to AMSR-E rain rate. Categories were created for the following ranges of AMSR-E rain rates: < 0.5, 0.5-1, 1-2, 2-4, and 4-8 mm/h. For each neural net RMS errors between adjusted AMSU/HSB rain rates and AMSR-E rain rates were computed for each category. For each category, the neural nets were ranked by RMS error (1 for the lowest). Then the neural nets were ranked according to the average of its ranks for each of the five categories. Then the neural net with the lowest average ranking and with plausible performance on NOAA-16 AMSU-A/B data from 1 July 2003 (a data set outside the seasonal range of the training, validation, and testing sets) was chosen. Fig. 6-1 shows a scatter plot

of the uncorrected $5^\circ \times 5^\circ$ AMSU/HSB rain rates vs. $5^\circ \times 5^\circ$ AMSR-E rain rates for the testing set. Fig. 6-2 is the same figure except with corrected $5^\circ \times 5^\circ$ AMSU/HSB rain rates. There is a significant reduction in the number of boxes for which the AMSU/HSB rain rate is greater than 2 mm/h and the AMSR-E rain rate is less than 1 mm/h.

Another way to validate the estimator is to compute cumulative distribution curves for the testing set. Of special interest is the quality of the estimates in the polar regions. One question to be addressed is whether the correction fixed the tendency to overestimate in the polar latitudes as was observed in Chapter 5. Fig. 6-3 shows cumulative distribution curves for $5^\circ \times 5^\circ$ boxes between 50° N and 50° S, and Fig. 6-4 shows the corresponding curves for $5^\circ \times 5^\circ$ boxes between 50° N and 70° N and between 50° S and 70° S. In the midlatitude and tropical regions, the correction did not significantly alter the cumulative distribution curves. However, in the polar latitudes, the correction resulted in the estimator underestimating the AMSR-E rain rates by a factor of about 2.

The AMSR-E-based correction was applied to the NEXRAD testing set of Chapter 4. The correction did not radically degrade the performance of the algorithm relative to NEXRAD. However, it would still be good to have the final estimator be able to maintain the quality of the retrievals described in Chapter 4.

One way to achieve the quality of the NEXRAD-trained estimator in the midlatitudes and quality of the AMSR-E-adjusted estimates in the high latitudes is to create a hybrid estimator that relies primarily on the original estimator in the midlatitude and tropical regions, and relies primarily on the AMSR-E-adjusted estimator in the high latitude regions (scaled by a factor of 2 to compensate for the overcorrection shown in Fig. 6-4.

Let $\hat{r}_{AMSU}$ and $\hat{r}'_{AMSU}$ be the NEXRAD-trained and AMSR-E-adjusted estimators (without the scaling factor of 2), respectively. Let k be the weight (between 0 and 1 inclusive) assigned to the AMSR-E-adjusted precipitation estimate. Then, $1 - k$ is the weight assigned to the NEXRAD-trained precipitation estimate.

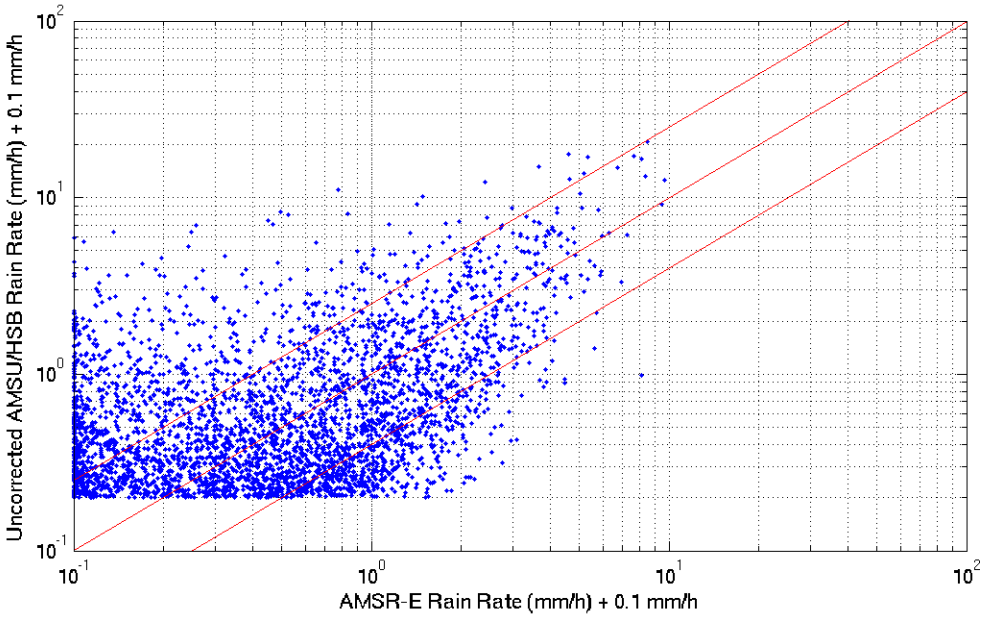

Figure 6-1: Scatter plot of $5° \times 5°$ uncorrected AMSU/HSB rain rates and AMSR-E rain rates. $5° \times 5°$ boxes for which the AMSU/HSB rain rate was less than 0.1 mm/h were excluded from the training, validation, and testing sets

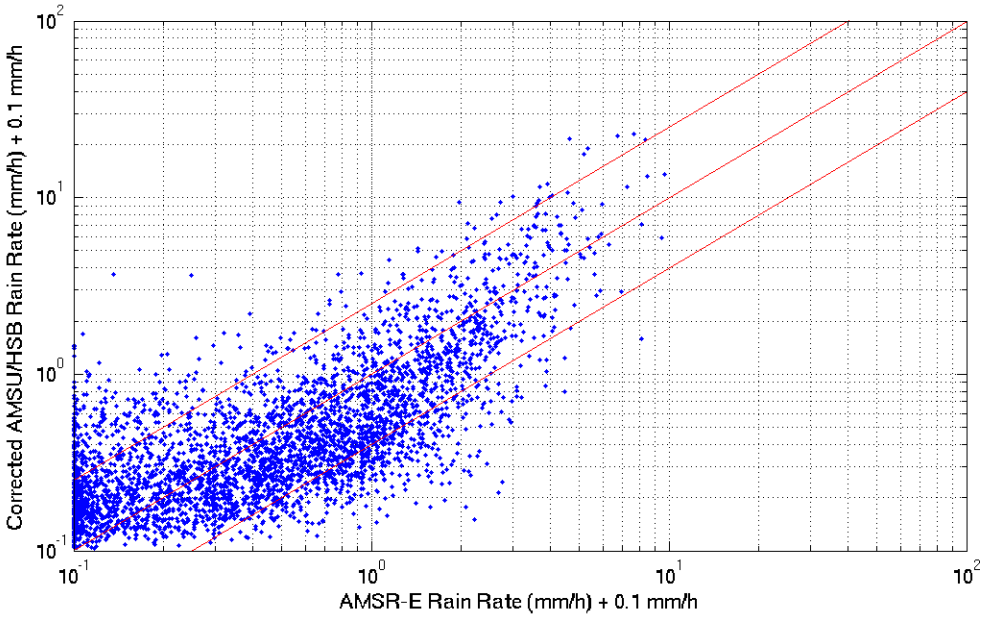

Figure 6-2: Scatter plot of $5° \times 5°$ AMSR-E-adjusted AMSU/HSB rain rates and AMSR-E rain rates

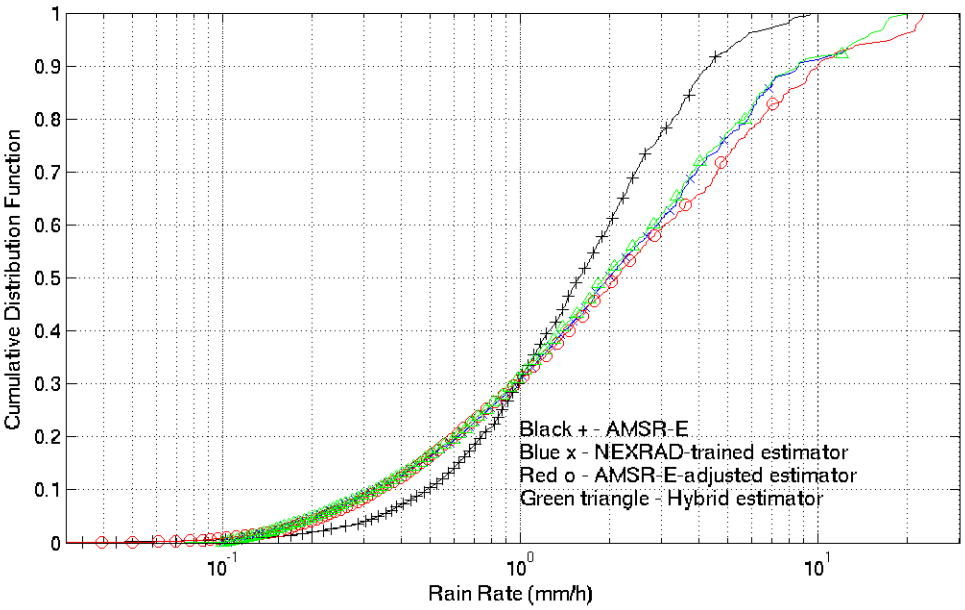

Figure 6-3: Cumulative distribution curves of $5° \times 5°$ AMSU/HSB and AMSR-E rain rates between 50° N and 50° S

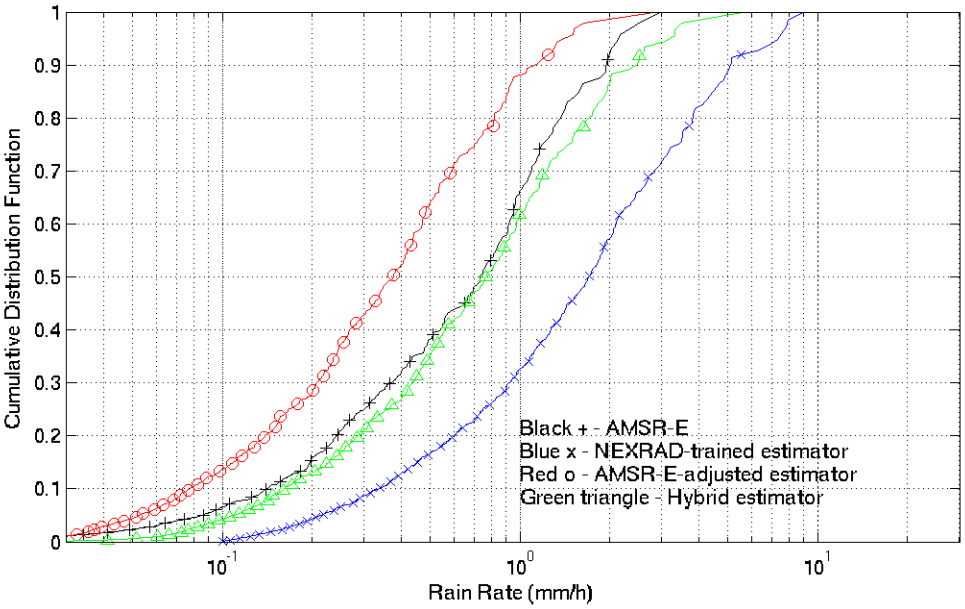

Figure 6-4: Cumulative distribution curves of $5° \times 5°$ AMSU/HSB and AMSR-E rain rates between 50° N and 70° N and between 50° S and 70° S

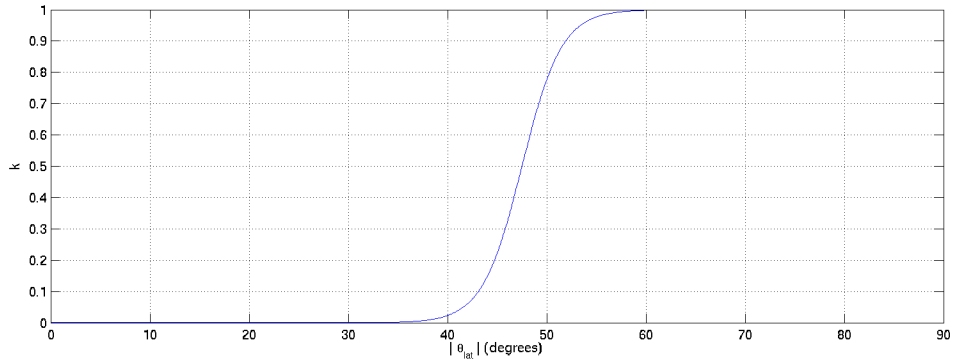

Figure 6-5: Latitude-dependent weights for AMSR-E-adjusted precipitation estimates

$$k = \frac{1}{2}\left[\tanh\left(\frac{\|\theta_{lat}\| - 47.5}{4}\right) + 1\right] \tag{6.1}$$

$$\hat{r} = (1-k)\hat{r}_{AMSU} + 2k\hat{r}'_{AMSU} \tag{6.2}$$

Fig. 6-5 shows the weight assigned to the AMSR-E-adjusted precipitation estimate. This function provides a transition region from $\sim 40°$ N to $\sim 55°$ N and from $\sim 40°$ S to $\sim 55°$ S.

Fig. 6-3 shows that the hybrid estimator does not seem to systematically introduce multiplicative errors in the midlatitude and tropical regions. Fig. 6-4 suggests that the factor of 2 has adequately compensated for the overcorrection.

Fig. 6-6 shows a scatter plot of NEXRAD-trained AMSU-A/B estimates before and after corrections vs. NEXRAD estimates for the NEXRAD-based testing set of Chapter 4, and Fig. 6-7 shows a scatter plot of NEXRAD-trained AMSU/HSB estimates before and after corrections vs. AMSR-E estimates for the testing set of this section. Both figures show that the corrections have preserved the quality of the AMSU/NEXRAD comparison in Chapter 4 and improved the quality of the AMSR-E-based correction for high-latitude regions.

Figs. 6-8 and 6-9 show sample results of applying the hybrid estimator to NOAA-16 AMSU-A/B data on 1 July 2003 and 19 Feb 2003, both of which are beyond the seasonal scope of the training, validation, and testing sets. They show that the hybrid

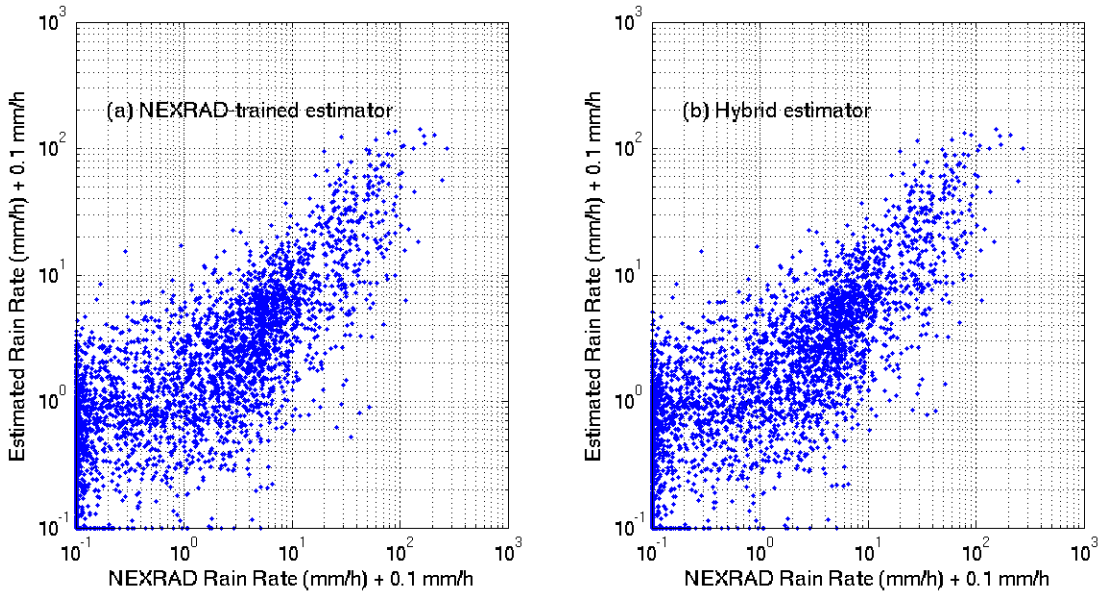

Figure 6-6: Scatter plot of AMSU estimates [(a) NEXRAD-trained and (b) hybrid] vs. NEXRAD estimates for the NEXRAD-based testing set of Chapter 4

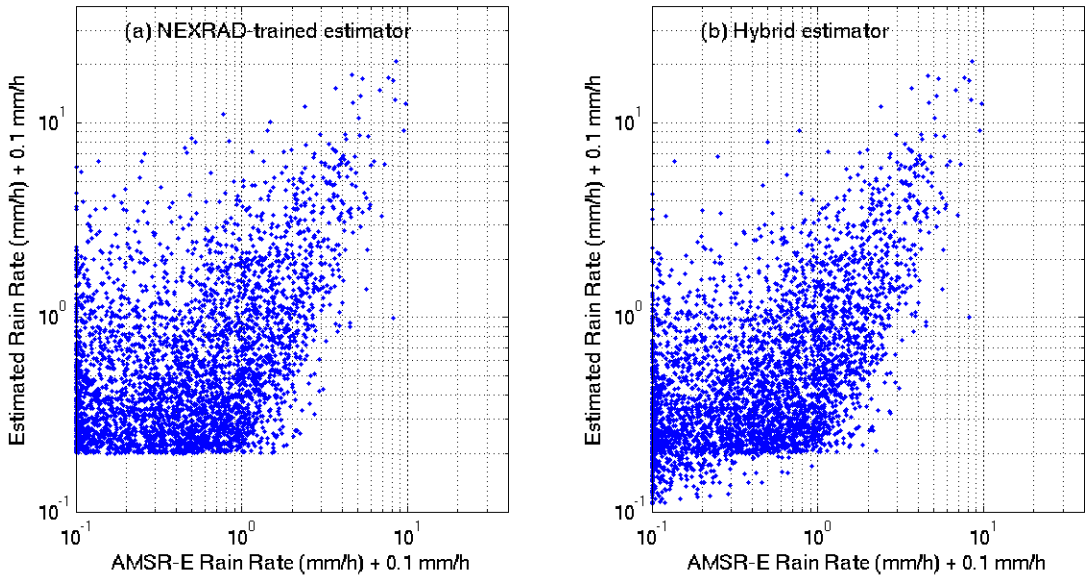

Figure 6-7: Scatter plot of AMSU estimates [(a) NEXRAD-trained and (b) hybrid] vs. AMSR-E estimates for the AMSR-E-based testing set of Sec. 6.1

estimator produces plausible results globally.

All rain rates higher than 100 mm/h are set to 100 mm/h.

6.2 Precipitation Means and Frequencies

Two useful metrics are the mean precipitation rate and precipitation frequency. These quantities are useful for climatological and hydrological purposes. The mean precipitation rate can provide an indication of how much latent heat is released into the atmosphere. Figs. 6-10 and 6-11 show mean rain rates and rain frequencies, respectively, calculated using one year of AMSU-A/B data from NOAA-15, NOAA-16, and NOAA-17. The hybrid algorithm of Sec. 6.1 was used. Precipitation frequency was defined to be the ratio of the number of times a pixel showed rain rates of greater than 0.1 mm/h to the number of times that pixel was observed by any of NOAA-15, NOAA-16, or NOAA-17. Some of the white areas in Figs. 6-10 and 6-11 are high-altitude regions over which the algorithm did not estimate precipitation (e.g. the Himalayas, Greenland, the Andes, and the Rocky Mountains).

Fig. 6-10 appears morphologically consistent with the global annual mean rain rates produced by the Global Precipitation Climatology Project (GPCP) and the Climate Prediction Center Merged Analysis of Precipitation (CMAP) both of which combine satellite-based retrievals and rain gauge measurements [31]. However, the AMSU-A/B-based 1-year mean rain rates exceed those of GPCP, CMAP, and U.S. based rain gauges [6] by large factors. For example, the mean annual rain rate over the southeastern U.S. is around 1 mm/h (or 24 mm/day) for AMSU-A/B while it is between 3 and 5 mm/day for GPCP, CMAP, and U.S. based rain gauges, a difference of a factor between 4.8 and 8.

Despite such a large difference, the AMSU-A/B-based rain rates are within the range of rain rates provided by trusted sources. Specifically, AMSU-A/B-based rain rates tend to average between those of NEXRAD and AMSR-E. The remainder of this section presents a comparison of NEXRAD-trained AMSU-A/B with NEXRAD and NEXRAD-trained AMSU/HSB and AMSR-E estimates. For the re-

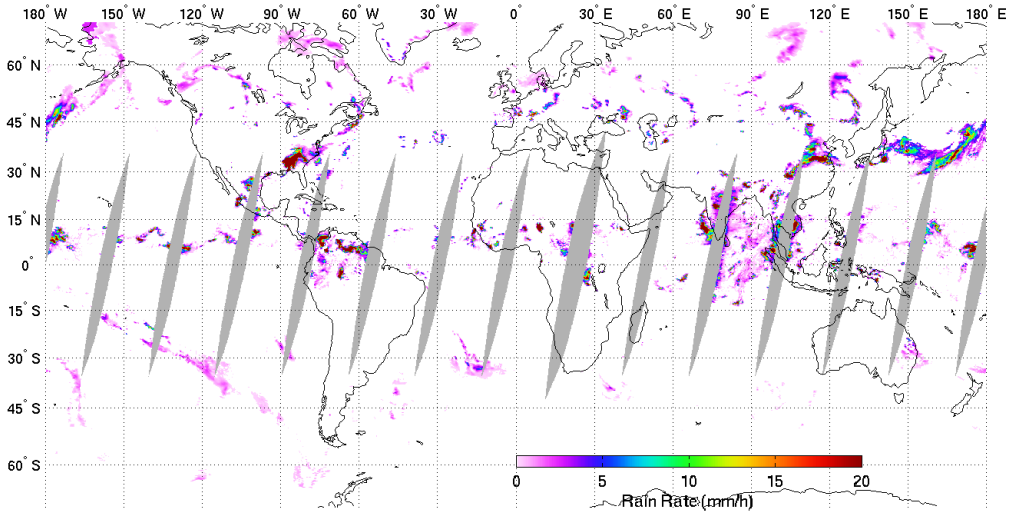

Figure 6-8: Corrected NOAA-16 AMSU-A/B rain rates for descending segments, 1 July 2003, ∼2 AM local time

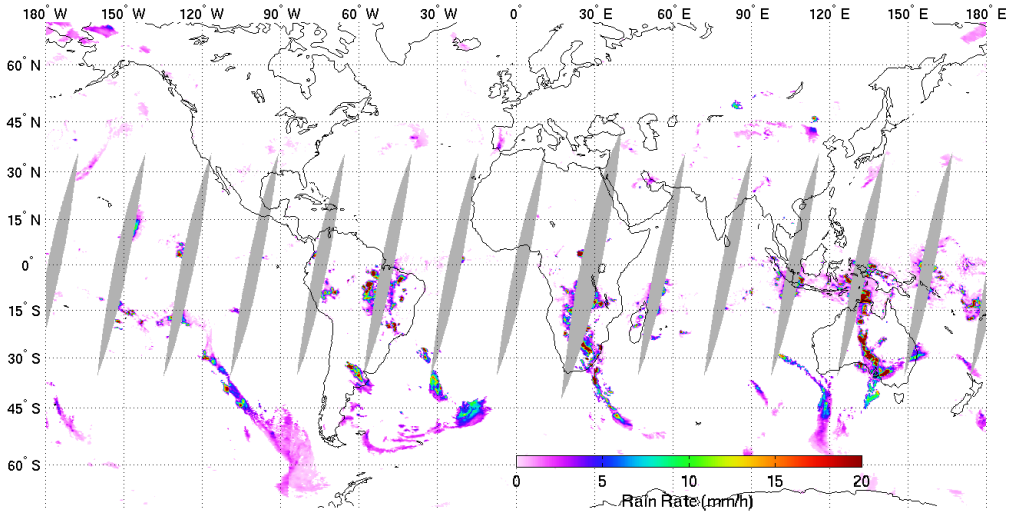

Figure 6-9: Corrected NOAA-16 AMSU-A/B rain rates for descending segments, 19 Feb. 2003, ∼2 AM local time

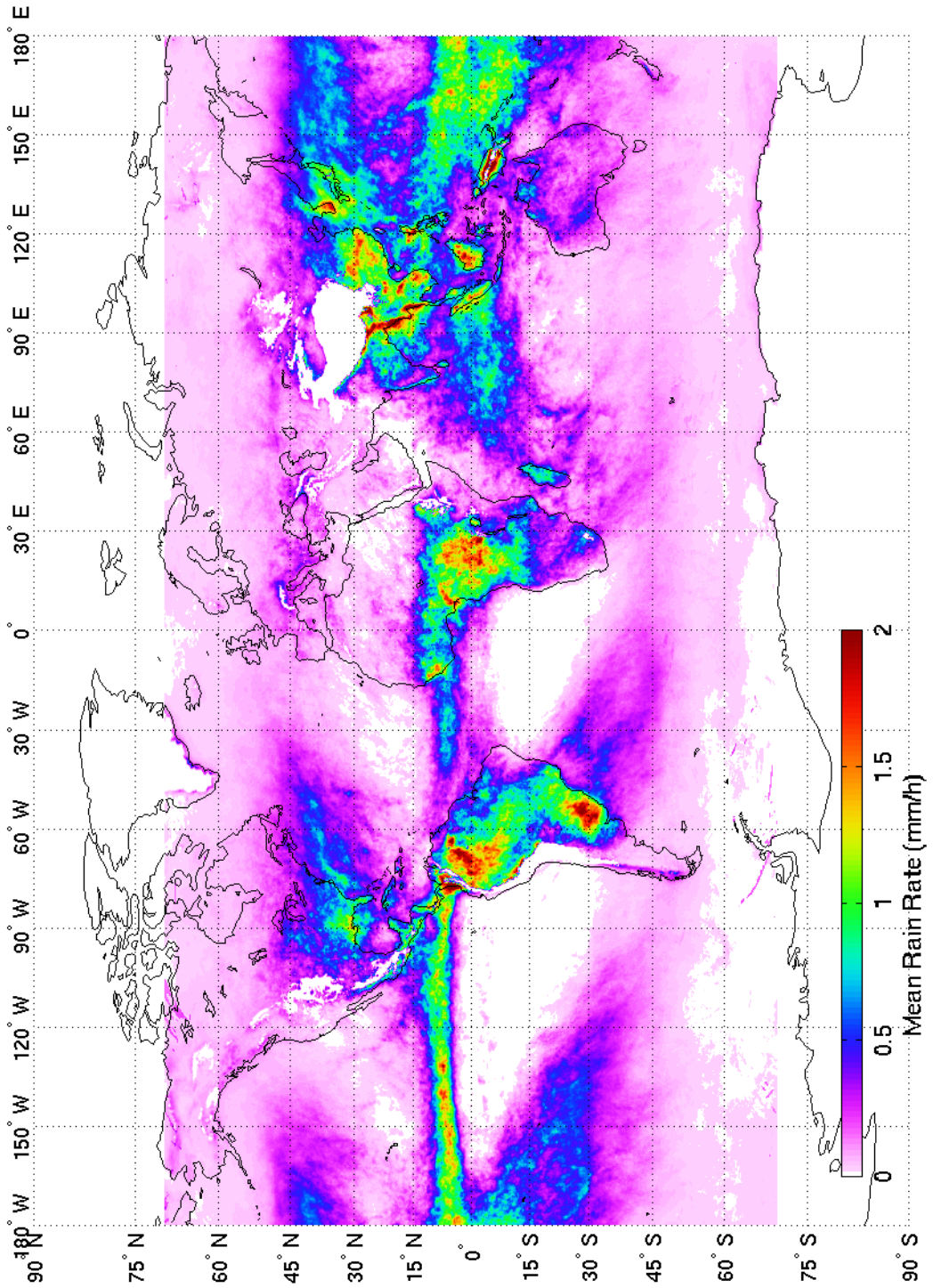

Figure 6-10: 15-km 1-year mean rain rate (mm/h) (July 2002 to June 2003) estimated using AMSU-A/B aboard NOAA-15, NOAA-16, and NOAA-17

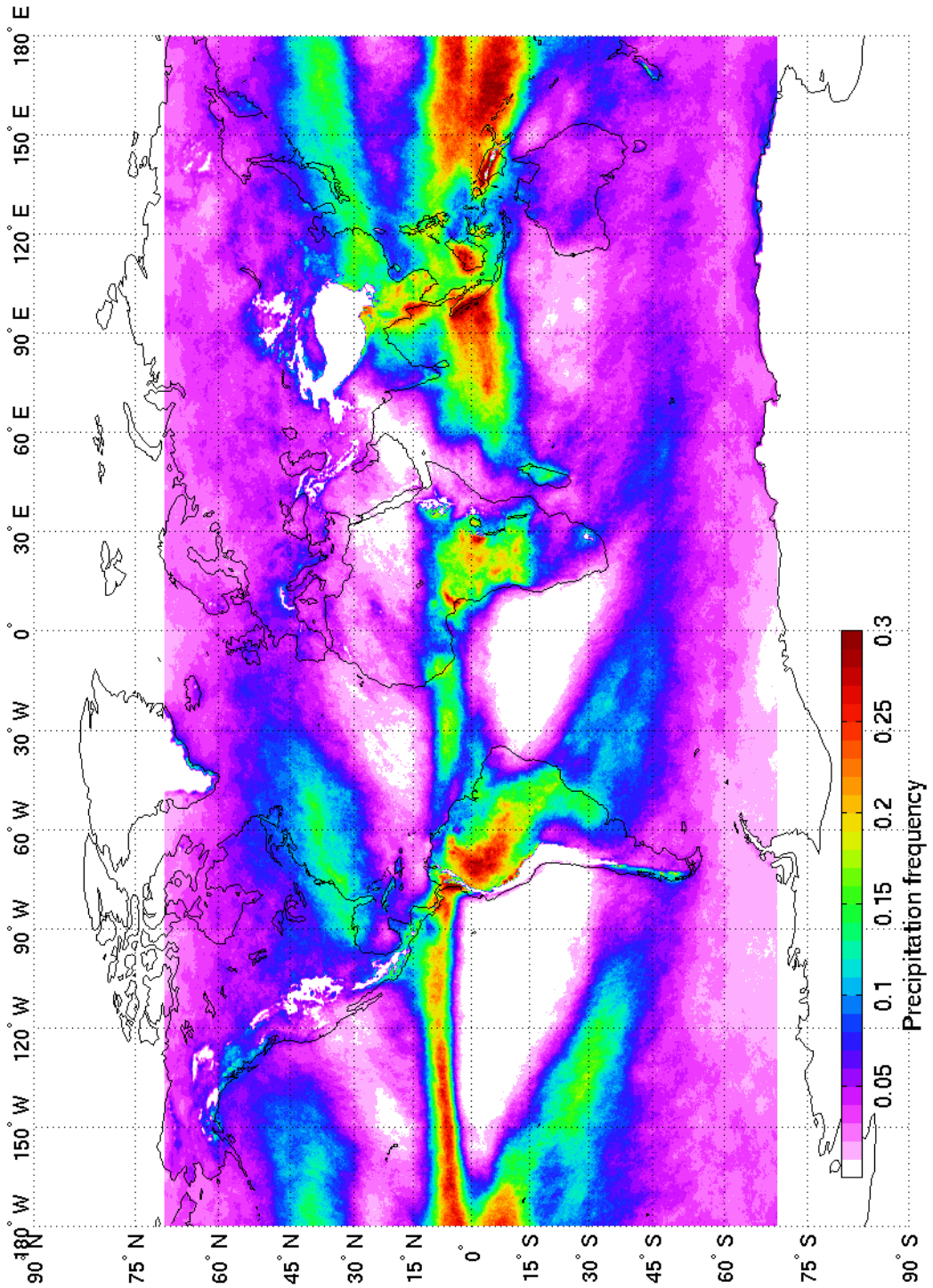

Figure 6-11: 15-km 1-year rain frequency (July 2002 to June 2003) estimated using AMSU-A/B aboard NOAA-15, NOAA-16, and NOAA-17

NEXRAD range	Mean (AMSU - NEXRAD) (mm/h)	RMS (AMSU - NEXRAD) (mm/h)	Mean (AMSU) / Mean (NEXRAD)
< 0.5 mm/h	0.6	1.0	10.3
0.5-1 mm/h	0.8	2.0	2.1
1-2 mm/h	0.7	2.3	1.5
2-4 mm/h	-0.1	2.7	1.0
4-8 mm/h	-1.0	3.5	0.8
8-16 mm/h	-3.1	6.9	0.7
16-32 mm/h	-4.9	19.0	0.8
> 32 mm/h	-25.2	42.9	0.6

Table 6.1: AMSU/NEXRAD comparisons at 15-km resolution for pixels in the range 30-110 km from NEXRAD radar sites. Pixels are categorized by NEXRAD rain rate

mainder of this section, the AMSU-A/B and AMSU/HSB estimates will refer to the NEXRAD-trained estimates without the corrections developed in Sec. 6.1. Tables 6.1 and 6.2 show means of the biases of AMSU estimates relative to NEXRAD, RMS AMSU/NEXRAD differences, and the ratio of the mean AMSU rain rate to the mean NEXRAD rain rate for the testing set of Chapter 4. For Table 6.1, the pixels are categorized by NEXRAD rain rate. For Table 6.2, the pixels are categorized by AMSU rain rate. One noticeable feature of Table 6.2 is that on average the AMSU rain rate is less than the NEXRAD rain rate for the AMSU rain rate categories between 0 and 32 mm/h. Table 6.1 shows that on average the AMSU rain rate is greater than the NEXRAD rain rate for the NEXRAD rain rate categories above 2 mm/h. Over all pixels in the testing set, the ratio of the mean of the NEXRAD rain rates to the mean of the AMSU rain rates is about 1.3. These results show that NEXRAD tends to yield higher rain rates and that one reason for the large difference between the hybrid AMSU-A/B estimator and GPCP is that for midlatitude regions the estimator was trained to a source that yields much higher rain rates than GPCP. NEXRAD tends to be more sensitive to larger particles while AMSU with channels at higher frequencies tends to be more sensitive to smaller particles.

AMSR-E tends to see more light rain and less heavy rain that AMSU/HSB. Tables 6.3 and 6.4 show means of the biases of AMSU/HSB relative to AMSR-E, RMS AMSU/HSB-AMSR-E differences, and the ratio of the mean AMSU/HSB rain rate

AMSU range	Mean (AMSU - NEXRAD) (mm/h)	RMS (AMSU - NEXRAD) (mm/h)	Mean (AMSU) / Mean (NEXRAD)
< 0.5 mm/h	-0.1	1.3	0.6
0.5-1 mm/h	-0.4	3.5	0.6
1-2 mm/h	-0.8	3.5	0.6
2-4 mm/h	-1.5	6.2	0.7
4-8 mm/h	-2.3	9.4	0.7
8-16 mm/h	-5.5	17.9	0.7
16-32 mm/h	-10.9	27.7	0.7
> 32 mm/h	1.2	38.7	1.0

Table 6.2: AMSU/NEXRAD comparisons at 15-km resolution for pixels in the range 30-110 km from NEXRAD radar sites. Pixels are categorized by AMSU rain rate

AMSR-E range	Mean (AMSU/HSB - AMSR-E) (mm/h)	RMS (AMSU/HSB - AMSR-E) (mm/h)	Mean (AMSU/HSB rain rate) / Mean (AMSR-E rain rate)
< 0.5 mm/h	0.3	0.8	2.7
0.5-1 mm/h	-0.05	0.9	0.8
1-2 mm/h	-0.3	1.3	0.8
2-4 mm/h	-0.2	2.0	0.9
4-8 mm/h	0.8	4.4	1.2
8-16 mm/h	5.6	7.1	1.6

Table 6.3: AMSU/HSB vs. AMSR-E comparisons for $5^\circ \times 5^\circ$ averages over ocean. Boxes are categorized by AMSR-E rain rate

to the mean AMSR-E rain rate for the testing set of Sec. 6.1. For Table 6.3, the pixels are categorized by AMSR-E rain rate. For Table 6.4, the pixels are categorized by AMSU/HSB rain rate. Table 6.3 shows that AMSR-E yields rain rates higher than AMSU/HSB for the AMSR-E rain rate categories between 0.5 and 4 mm/h, and Table 6.4 shows that AMSU/HSB yields rain rates that are higher than those from AMSR-E for the categories in which AMSU/HSB rain rates are higher than 1 mm/h. The AMSR-E estimates tend to be more sensitive to warm rain and stratiform rain because it depends on emission signatures while the AMSU/HSB algorithm was trained primarily on data over convective precipitation.

One possibility for future study could involve attempts to reconcile the widely differing annual mean rain rate estimates. The algorithm developed for AMSU-A/B

AMSU/HSB range	Mean (AMSU/HSB - AMSR-E) (mm/h)	RMS (AMSU/HSB - AMSR-E) (mm/h)	Mean (AMSU/HSB rain rate) / Mean (AMSR-E rain rate)
< 0.5 mm/h	-0.2	0.5	0.5
0.5-1 mm/h	-0.01	0.8	0.9
1-2 mm/h	0.4	1.1	1.2
2-4 mm/h	1.2	1.9	1.6
4-8 mm/h	3.0	3.5	2.0
8-16 mm/h	6.3	7.0	2.3

Table 6.4: AMSU/HSB vs. AMSR-E comparisons for $5° \times 5°$ averages over ocean. Boxes are categorized by AMSU/HSB rain rate

and AMSU/HSB does not detect warm rain[2] which can result in warm perturbations in the 54-GHz band. One weakness of rain gauges is that the quality of their measurements can be affected by horizontal wind speed. Also, some of the discrepancy between satellite-based methods and rain gauges might be due to evaporation of falling hydrometeors.

6.3 Diurnal Cycle

Some of the variation of precipitation is diurnal, particularly in the tropics. Let $R(t)$ be the precipitation rate as a function of the local solar time t in hours. $R(t)$ is assumed to have the form of a sinusoid:

$$R(t) = A\cos(\omega t - \psi) + c \tag{6.3}$$

There are three unknowns: the diurnal amplitude A, the phase ψ, and the mean c. Because t is in terms of hours, $\omega = 2\pi/24$. A is assumed to be non-negative so that the solution is unique and the phase is an indication of the time when the average rain rate is maximum. Eq. 6.3 can be rewritten as follows:

$$R(t) = a\cos(\omega t) + b\sin(\omega t) + c \tag{6.4}$$

[2] "Rain formed from a cloud having temperatures at all levels above 0° C (32° F), and resulting from the droplet coalescence process" [28]

where $a = A\cos\psi$, and $b = A\sin\psi$. With the NOAA-15, NOAA-16, and NOAA-17 satellites, there are six equatorial crossing times: 2 AM, 7 AM, 10 AM, 2 PM, 7 PM, and 10 PM whose corresponding values of t are 2, 7, 10, 14, 19, and 22, respectively. It is assumed that any observation done by a satellite in a direction (i.e. northbound or southbound) will have a time of day equal to the corresponding equatorial crossing time of that satellite in that direction, e.g. a pixel observed by NOAA-16 while travelling southward will have a time of day of 2 AM. This assumption does not take into account the differences in solar time for different scan angles. This assumption also does not consider differences due to the time a satellite takes to travel from the North Pole to the South Pole and viceversa.

Diurnal cycles of monthly precipitation averages can be computed using the least-squares approximation method [83]. Let $\mathbf{R}$ be the 6×1 matrix of the values of R at these times, $\mathbf{x}$ be a 3×1 matrix of the values being solved for, and $\mathbf{A}$ be a 6×3 matrix of the terms in $R(t)$ without the coefficients that are being solved for.

$$\mathbf{R} = \begin{pmatrix} R(2) \\ R(7) \\ R(10) \\ R(14) \\ R(19) \\ R(22) \end{pmatrix} \tag{6.5}$$

$$\mathbf{x} = \begin{pmatrix} a \\ b \\ c \end{pmatrix} \tag{6.6}$$

$$\mathbf{A} = \begin{pmatrix} \cos(2 \cdot \frac{2\pi}{24}) & \sin(2 \cdot \frac{2\pi}{24}) & 1 \\ \cos(7 \cdot \frac{2\pi}{24}) & \sin(7 \cdot \frac{2\pi}{24}) & 1 \\ \cos(10 \cdot \frac{2\pi}{24}) & \sin(10 \cdot \frac{2\pi}{24}) & 1 \\ \cos(14 \cdot \frac{2\pi}{24}) & \sin(14 \cdot \frac{2\pi}{24}) & 1 \\ \cos(19 \cdot \frac{2\pi}{24}) & \sin(19 \cdot \frac{2\pi}{24}) & 1 \\ \cos(22 \cdot \frac{2\pi}{24}) & \sin(22 \cdot \frac{2\pi}{24}) & 1 \end{pmatrix} \tag{6.7}$$

One would like to be able to solve the following equation if possible.

$$\mathbf{Ax} = \mathbf{R} \tag{6.8}$$

However, since there are more measurements than equations, the best that one can do is to find the $\mathbf{x}$ that minimizes $\| \mathbf{R} - \mathbf{Ax} \|$. The least-squares approximation method will be used to determine $\mathbf{x}$.

$$\mathbf{x} = (\mathbf{A}^T\mathbf{A})^{-1}\mathbf{A}^T\mathbf{R} \tag{6.9}$$

Then, A and ψ are determined from a and b.

$$A = \sqrt{a^2 + b^2} \tag{6.10}$$

ψ is selected to satisfy the following conditions:

$$\cos\psi = \frac{a}{A} \tag{6.11}$$

$$\sin\psi = \frac{b}{A} \tag{6.12}$$

This method is also used in [12] with SSM/I data.

Fig. 6-12 shows the diurnal variations from one year (July 2002 to June 2003) of AMSU-A/B data from NOAA-15, NOAA-16, and NOAA-17. Large systematic mean-normalized diurnal amplitudes (> 0.4) tend to occur in desert regions (e.g. North Africa, Australia) where the mean rain rate is small (< 0.2 mm/h), and the mean-normalized diurnal amplitudes tend to be smaller in regions where the annual mean

rain rate is large (> 0.8 mm/h). In regions where the mean is less than 0.02 mm/h, the phase of the diurnal variations varies very erraticly as might be expected. Overall, the map shows geophysically plausible variations in mean rain rate, mean-normalized diurnal amplitude, and the phase of the diurnal variation.

Figs. 6-13, 6-14, 6-15, and 6-16 show diurnal variations in the same way as Fig. 6-12 but for the summer, fall, winter, and spring, respectively. Together, these figures show that there are systematic seasonal variations in the diurnal cycle of precipitation rate. For example, for north Africa, the local solar times of maximum precipitation rate are around 2200, 1800, 0100, and 2300, for summer, fall, winter, and spring, respectively.

Similar studies of the diurnal variation of precipitation have also been done by Dai et al. [21] and Chang et al. [12]. Dai et al. computed diurnal variations of precipitation rate over the continental U.S. for 2.5° longitude by 2° latitude boxes using 31 years of hourly precipitation data. There is some agreement in the preferred time of precipitation between the seasonal diurnal variations of AMSU-A/B precipitation rate computed for Figs. 6-13 to 6-16 where the diurnal character is strong. The best agreement occurs during the summer months. Chang et al. computed diurnal variations of precipitation rate over ocean over a $5° \times 5°$ global grid using 4 1/2 years of SSM/I data from two satellites. The SSM/I-based study showed monthly maps of diurnal variations over ocean that were quite noisy. It is possible that the noise could have been mitigated and systematic features could have been more evident if the variations were computed over larger regions and longer time periods.

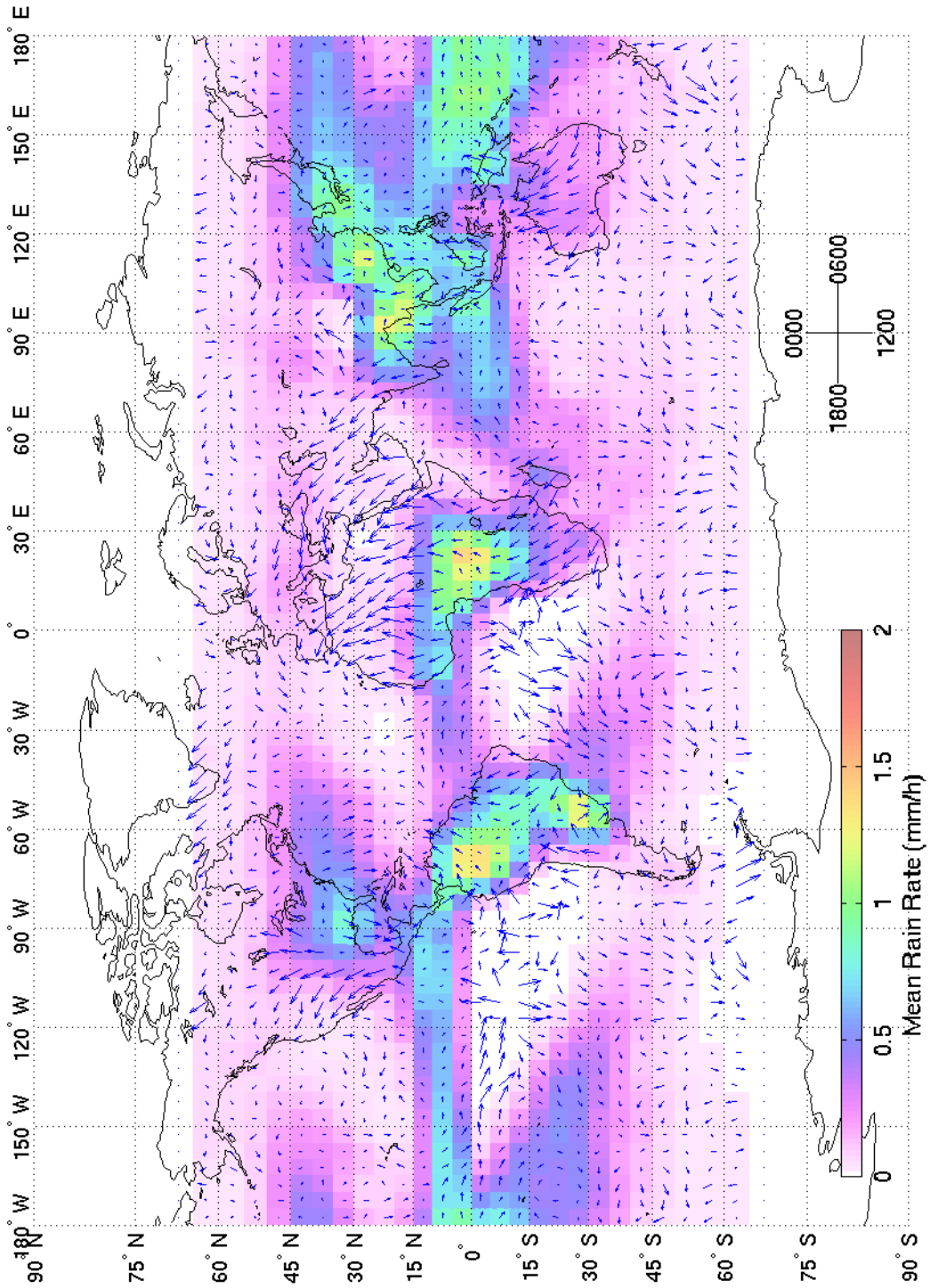

Figure 6-12: Diurnal variations of $10° \times 10°$ precipitation rate over one year (July 2002 to June 2003) of AMSU-A/B data from NOAA-15, NOAA-16, and NOAA-17. The length of an arrow is proportional to the mean-normalized diurnal amplitude values of up to 0.5. The direction of the arrows represent local solar times for maximum rain rate. The background is an image of the annual mean rain rate.

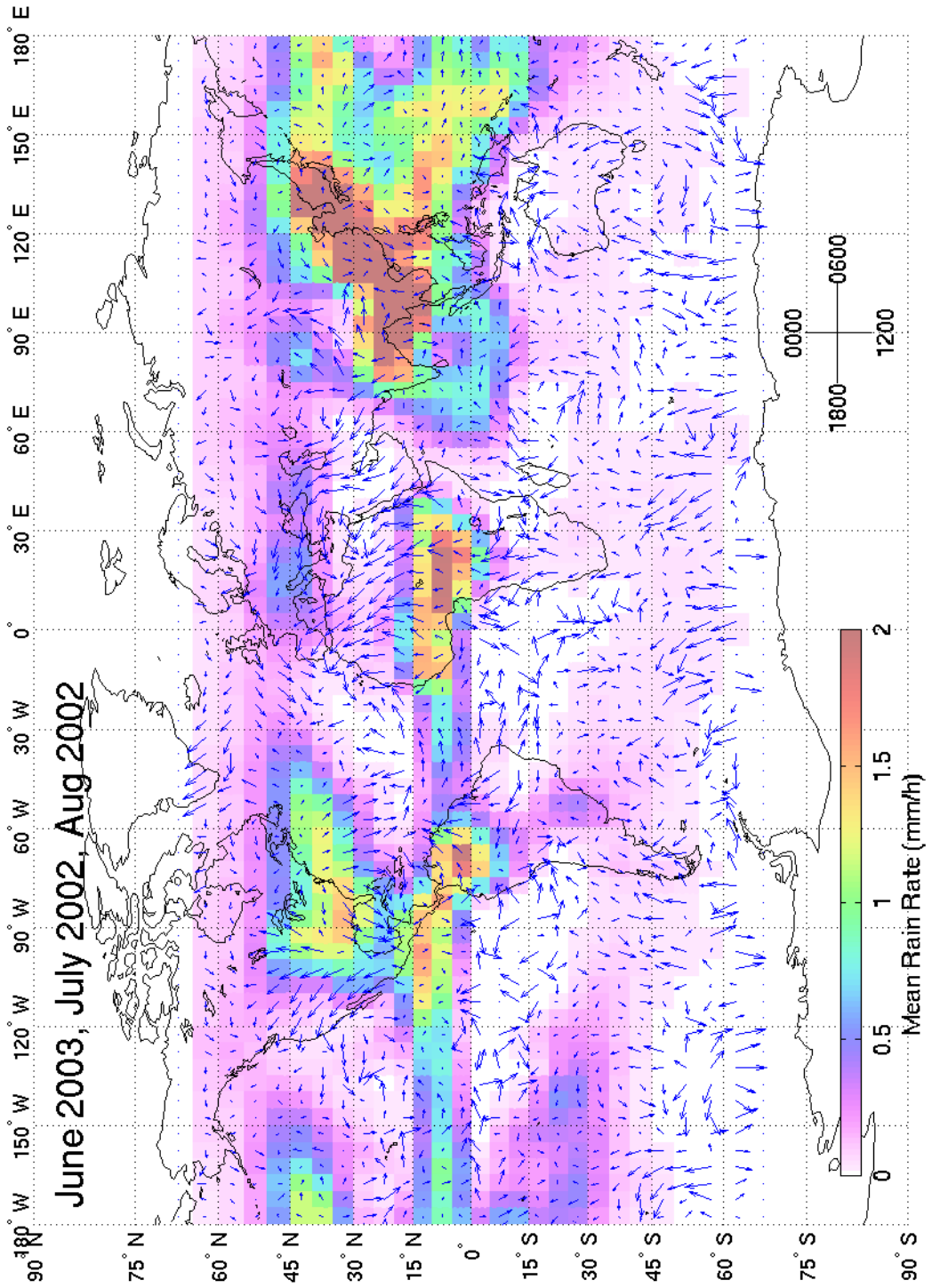

Figure 6-13: Diurnal variations of $10° \times 10°$ precipitation rate (as in Fig. 6-12) during summer months (June 2003, July 2002, and August 2002) of AMSU-A/B data from NOAA-15, NOAA-16, and NOAA-17

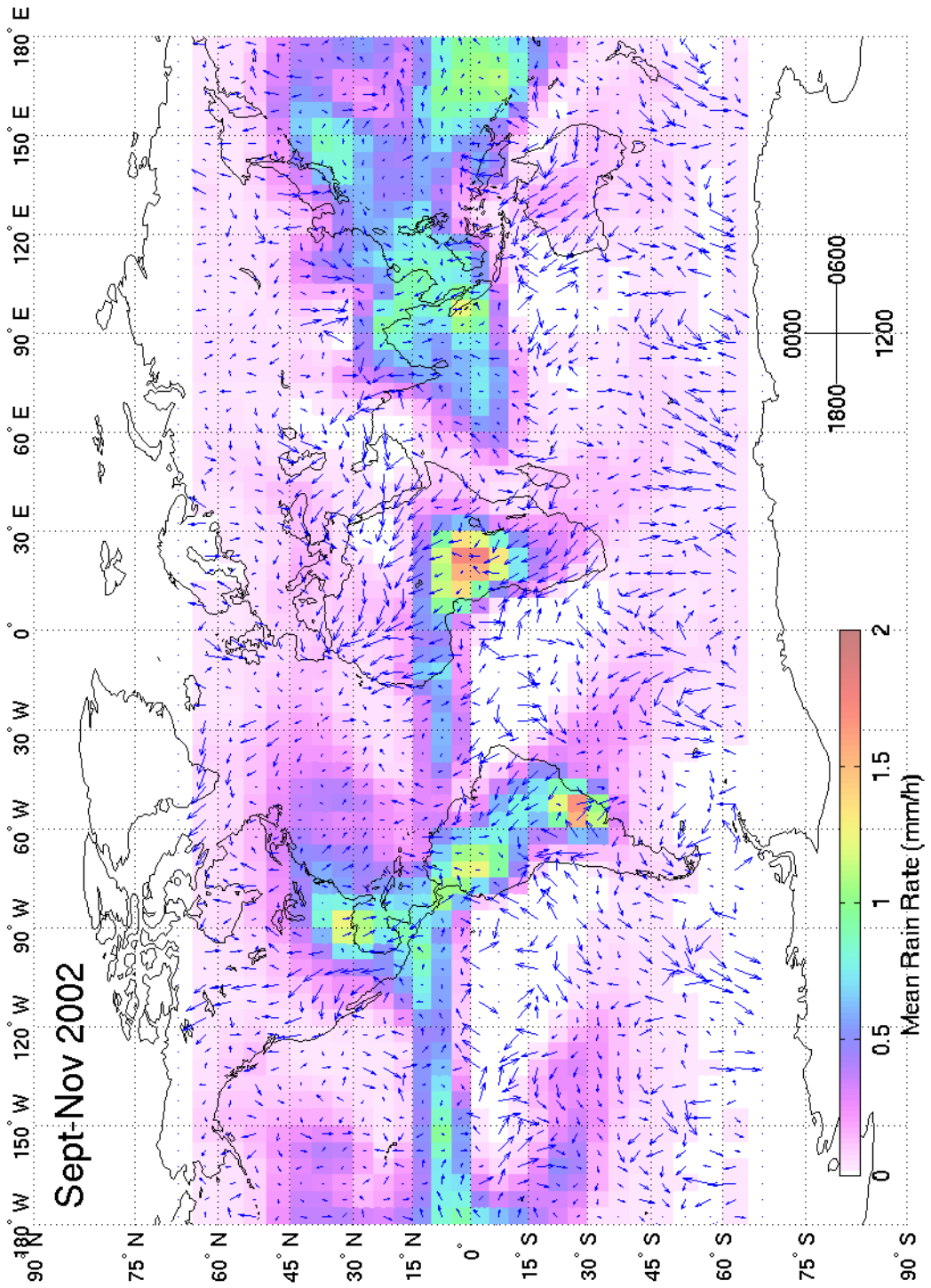

Figure 6-14: Diurnal variations of $10° \times 10°$ precipitation rate (as in Fig. 6-12) during fall (Sept. to Nov. 2002) of AMSU-A/B data from NOAA-15, NOAA-16, and NOAA-17

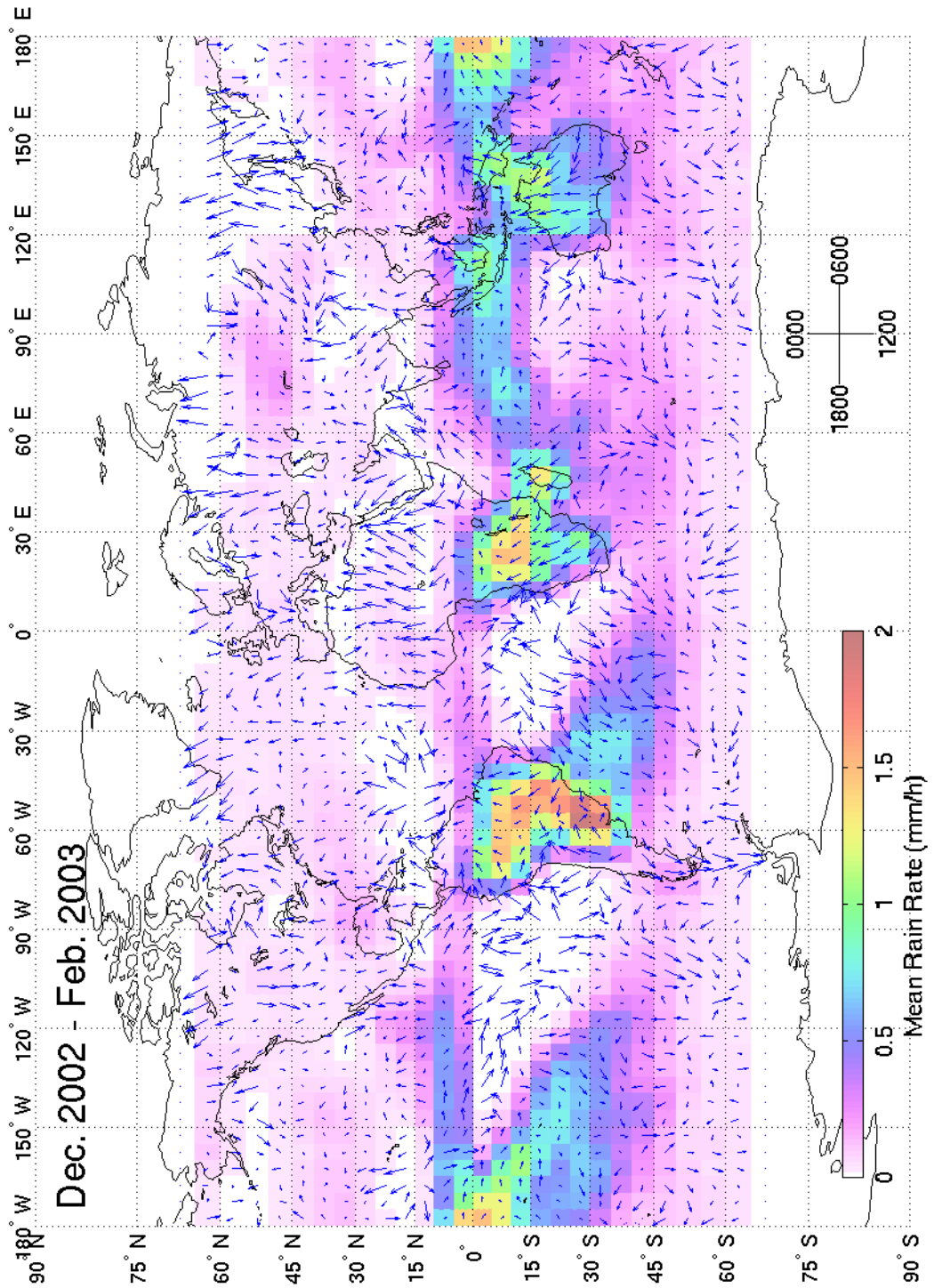

Figure 6-15: Diurnal variations of $10° \times 10°$ precipitation rate (as in Fig. 6-12) during winter (Dec. 2002 to Feb. 2003) of AMSU-A/B data from NOAA-15, NOAA-16, and NOAA-17

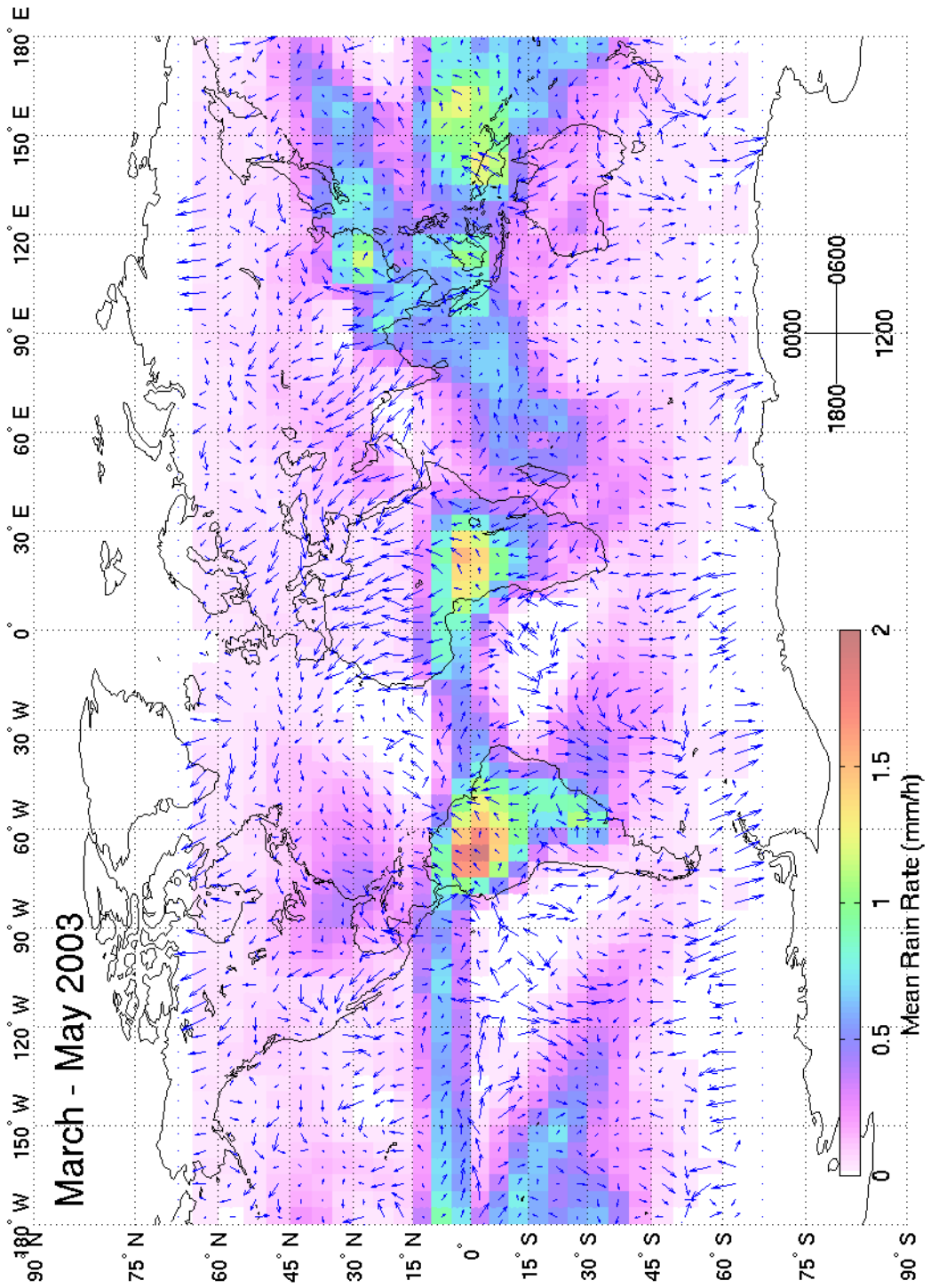

Figure 6-16: Diurnal variations of $10° \times 10°$ precipitation rate (as in Fig. 6-12) during spring (March to May 2003) of AMSU-A/B data from NOAA-15, NOAA-16, and NOAA-17

Chapter 7

Conclusions

7.1 Summary of the Thesis

This thesis has presented a precipitation-rate estimation algorithm that relies primarily on opaque microwave channels in the 54-GHz oxygen and 183-GHz water vapor resonance bands. The algorithm uses spatial filtering, PCA, and data fusion. Spatial filtering is employed in order to compute the precipitation-induced perturbations in AMSU-A channels 4 to 8 (Sec. 4.2.3). PCA is used to create a compact representation of sets of channels that provide information about important variables. Constrained PCA is used to eliminate the signatures of surface variations from water-vapor principal components. A data fusion method was developed for sharpening 50-km brightness temperature perturbation images from AMSU-A to 15-km resolution. The algorithm was evaluated quantitatively by comparisons with NEXRAD data over the eastern U.S. and qualitatively through global precipitation snapshots and climatology, and then adjustments were made by training a neural net to estimate multiplicative correction factors based on AMSR-E estimates.

The algorithm has also demonstrated the ability to detect and estimate precipitation rate due to snow. With the AMSR-E-based adjustments, the estimator was able to produce realistic estimates of precipitation rate in polar climates at latitudes beyond 50° away from the equator.

The algorithm was used to do some precipitation climatology studies. The 15-

km annual mean rain rate showed morphology that is consistent with what has been seen in [31]. Differences in quantitative results were also studied. Global annual and seasonal diurnal variation maps were also produced.

7.1.1 Main Contributions

The results presented in this thesis show that the opaque microwave frequency bands are useful for precipitation-rate retrievals and could be used in addition to the traditional window channels aboard scientific and operational instruments such as AMSU, TMI, SSM/I, AMSR-E, ATMS (the Advanced Technology Microwave Sounder for the National Polar-Orbiting Environmental Satellite System [NPOESS]), SSMIS (Special Sensor Microwave Imager/Sounder), and CMIS (the Conical Scanning Microwave Imager/Sounder for NPOESS). In particular, ATMS will have all of the channels on AMSU-A/B (except the 89.0-GHz channel on AMSU-A and the 150-GHz channel on AMSU-B) and channels at 51.76 GHz, 165.5 GHz, 183 ± 4.5 GHz, and 183 ± 1.8 GHz [76].

7.1.2 Secondary Contributions

This thesis also has demonstrated the utility of spatial filtering and data fusion for image sharpening and precipitation estimation, methods that could be incorporated into future operational algorithms.

While previous algorithms for estimating instantaneous precipitation rate have treated each pixel independently, spatial filtering permitted the calculation of cloud-cleared brightness temperatures and precipitation-induced perturbations in the 54-GHz band (Sec. 4.2.3) which enabled characterization of the temperature profile using PCA (Sec. 4.2.4). Both precipitation-induced perturbations and temperature profile provide information that is useful for estimating precipitation [15].

Multiresolution data fusion made it possible to estimate precipitation rate at 15-km resolution even though some channels provide data only at 50-km resolution. The method developed for this thesis converted data from some 50-km channels into a form

that was useful for 15-km estimation. Multiresolution data fusion could prove useful for precipitation retrievals using ATMS since for each location observed it will measure brightness temperatures using channels that have different spatial resolutions [76].

7.2 Future Work

This section addresses possible improvements to the algorithm described in Chapter 4 and possible future studies. Improvements that could involve changes in the algorithm architecture or concepts in data analysis are considered major improvements while all other improvements are considered minor improvements.

7.2.1 Minor Improvements to the Algorithm

- *Expansion and improvement of the training, validation, and testing sets used to train the neural net.* This could involve including more NEXRAD data or including radar data from instruments outside the U.S. such as BALTEX which makes observations for Scandinavia. Data from other satellites were not used to train the neural net because coincident (or nearly-coincident) observations of AMSU and other satellite-based instruments typically are rare. One exception to this is the pair Aqua AMSU/HSB and Aqua AMSR-E. AMSR-E data was used in Chapter 6. High-resolution (e.g. 2-km) numerical weather prediction models could also be used together with a good radiative transfer model. Comparison with diurnal or seasonal rain gauge data could provide calibration factors.

- *Improving the limb-and-surface correction of the AMSU-A channels.* The method described in Sec. 4.2.1 involved training a neural net to estimate nadir-viewing brightness temperatures and was purely statistical. Goldberg et al. developed a statistical method for correcting AMSU-A that considered physical constraints [29].

- *Extension of the cloud-clearing procedure.* The cloud-clearing procedure in Sec. 4.2.3 did not provide a way to process corner regions. A method for doing this has been developed but because of time constraints will not be incorporated into the algorithm until after the completion of this thesis. This method is described in Appendix A.

- *Use of better signal separation techniques.* One possibility is to use independent component analysis (ICA). PCA transforms random vectors into uncorrelated random variables using second-order statistics. ICA refers to a class of methods that attempt to transform random vectors into variables that are as statistically independent as possible using additional statistics (e.g. kurtosis and entropy) [40, 41, 42] or different frameworks for characterizing degrees of statistical independence [4]. It is possible for ICA to separate signals into a representation that is more useful than PCA for input to the neural network.

7.2.2 Major Improvements to the Algorithm

- *Better use of the window channels.* In this thesis, the window channels were used merely as inputs to a principal-component-based transformation while window-channel-based algorithms intentionally made use of the emission and scattering signatures in nonlinear ways [89].

- *Use of physical models.* The complexity of precipitation prevents a complete characterization by any physical model. However, physical models might still lead to useful characterizations.

- *Use of cloud liquid water profile retrievals and better estimation of warm rain.* Rosenkranz has developed a method for retrieving non-precipitating cloud liquid water mixing ratio profile using Aqua AMSU/HSB [74]. Such information can be used to improve precipitation-rate retrievals, particularly for non-glaciated precipitation or warm rain. The algorithm developed for this thesis was trained primarily on convective cells that produce ice particles. The algorithm relies in

part on cold brightness temperature perturbations in the 54-GHz band. Warm rain might not appear in the perturbation images. Although detected by the precipitation detection method in Sec. 4.2.2, warm rain probably will not be accurately estimated. The AMSU-B 150-GHz could prove useful for this purpose. The more opaque 183 ± 7-GHz channel was favored for precipitation detection because the 150-GHz tends to be sensitive to surface variations. A future version of the algorithm could involve the 150-GHz channel in precipitation detection.

- *Improved detection and estimation of stratiform precipitation.* The method presented in this thesis was trained primarily on convective precipitation. More studies will be needed to determine how to make it more suitable for stratiform precipitation.

- *Regional storm-by-storm retrievals.* This thesis demonstrated a method for estimating instantaneous precipitation rate at each pixel. It might be useful also to estimate regionally integrated precipitation-rates on a storm-by-storm basis since geometrical properties and regional statistics can provide useful information about the intensity of a convective storm. This has been done in [24, 57, 59, 81].

7.2.3 Future Studies

- *Comparison with NEXRAD climatology.* NEXRAD provides estimates of precipitation rate over most of the U.S. approximately every 15 minutes. This frequency may be useful in for validating precipitation climatology based on AMSU.

- *Snow.* Although the algorithm has shown promise for the remote sensing of snowfall, validation of the estimates still remains to be done.

- *Comparison with rain gauges and other sensor systems and numerical weather prediction models.* The final AMSU-A/B estimator of Chapter 6 was found to yield precipitation-rate estimates that were on average between those of

NEXRAD and AMSR-E, and therefore substantially above rain gauge averages. Further comparisons with these and other instruments and model may help to improve the estimator.

- *Post-calibration application to important meteorological questions.* After calibration with rain gauges, radars, other satellite-based instruments, the algorithm can be used for hydrological and climatological applications. Climatological applications might include a study of the modes of variation of precipitation, e.g. yearly, seasonal, monthly, weekly, diurnal, and semidiurnal. Yearly, seasonal, and diurnal variations were addressed in Chapter 6. Hydrological applications might include studies related to agriculture or the contribution of runoff to rivers.

Appendix A

Improved Cloud-Clearing at Image Corners

The cloud-clearing method in Sec. 4.2.3 did not provide a way to process corner regions because there is no information that would enable one to estimate the cloud-free brightness temperatures at a cloud-perturbed corner of a brightness temperature image; this is unlike edge regions for which brightness temperatures along an edge can be interpolated using the boundary pixels that surround the edge. This could result in a significant amount of information about precipitation being lost. Region I in Fig. A-1 is one such example. Using the current version of the cloud-clearing procedure, all of the pixels in region I will be ignored despite the fact that a simple interpolation between pixels A and B would be able to salvage an overwhelming majority of the pixels. This requires a new way of thinking about corner regions.

Previously, for each region the following question was considered: Is there enough information to do cloud-clearing over all of the pixels? To salvage information in corner regions, the question will be changed to the following: For what pixels is there enough information to do cloud-clearing? The second question has already been incorporated into the cloud-clearing method to an extent. The procedure for processing complete-edge regions addresses this questions.

Interpolation of data at a point is possible when that point lies inside a polygon determined by some set of points where the value of the data field has already been

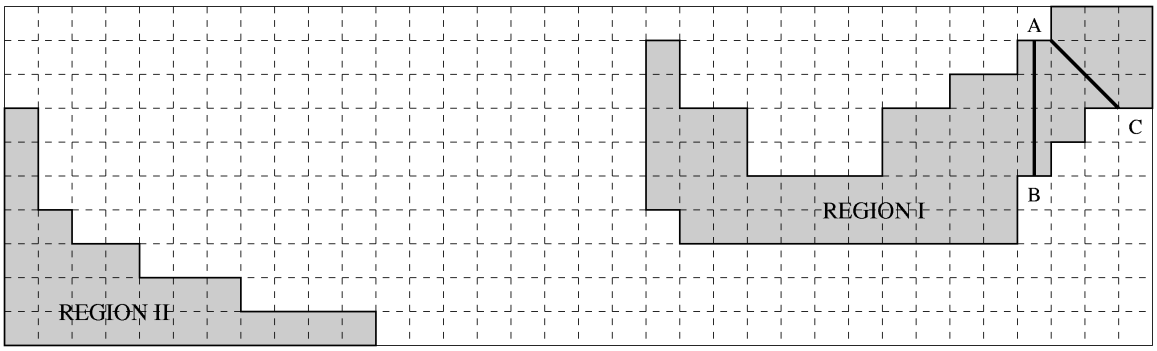

Figure A-1: Corner region and methods for salvaging pixels.

given. Therefore, the set of points over which cloud-clearing can be done is the set of points inside or on the smallest convex polygon containing all of the non-precipitating pixels in the brightness temperature image. In Fig. A-1, this polygon includes the line segment connecting pixels A and C. After the convex polygon has been determined, a method for interpolating brightness temperatures along the edges of the polygon where there is precipitation will be needed.

Sometimes it is not possible to salvage data from any portion of a corner region. Region II in Fig. A-1 is one such example. Because the border between the corner region and the non-precipitating region is not convex relative to the corner, it is not possible to interpolate brightness temperatures at any of the pixels in the corner region.

Bibliography

[1] R.F. Adler, C. Kidd, G. Petty, M. Morissey, and H.M. Goodman, "Intercomparison of Global Precipitation Products: The Third Precipitation Intercomparison Project (PIP-3)," *Bulletin of the American Meteorological Society*, vol. 82, no. 7, pp. 1377-1396, July 2001.

[2] P.A. Arkin and P. Xie, "The Global Precipitation Climatology Project: First Algorithm Intercomparison Project," *Bulletin of the American Meteorological Society*, vol. 75, no. 3, pp. 401-420, 1994.

[3] H.H. Aumann, M.T. Chahine, C. Gautier, M.D. Goldberg, E. Kalnay, L.M. McMillin, H. Revercomb, P.W. Rosenkranz, W.L. Smith, D.H. Staelin, L.L. Strow, J. Susskind, "AIRS/AMSU/HSB on the Aqua Mission: Design, Science Objectives, Data Products, and Processing Systems," *IEEE Transactions on Geoscience and Remote Sensing*, vol. 41, no. 2, pp. 253-264, Feb. 2003.

[4] F.R. Bach and M.I. Jordan, "Kernel Independent Component Analysis," *Proceedings of the 2003 IEEE International Conference on Acoustics, Speech, and Signal Processing*, vol. 4, pp. 876-879, 2003.

[5] L. Bai and D.H. Bromwich, personal communication, 2003.

[6] J.L. Baldwin, *Climatic Atlas of the United States*, National Oceanographic and Atmospheric Administration, Washington, DC, 1983.

[7] T. Bellerby, M. Todd, D. Kniveton, and C. Kidd, "Rainfall Estimation from a Combination of TRMM Precipitation Radar and GOES Multispectral Satellite

Imagery through the Use of an Artificial Neural Network," *Journal of Applied Meteorology*, vol. 39, pp. 2115-2128, Dec. 2000.

[8] W.J. Blackwell, "Retrieval of Cloud-Cleared Atmospheric Temperature Profiles from Hyperspectral Infrared and Microwave Observations," Sc.D. thesis, Massachusetts Institute of Technology, Department of Electrical Engineering and Computer Science, June 2002.

[9] W.J. Blackwell, J.W. Barrett, F.W. Chen, R.V. Leslie, P.W. Rosenkranz, M.J. Schwartz, and D.H. Staelin, "NPOESS Aircraft Sounder Testbed-Microwave (NAST-M): Instrument Description and Initial Flight Results," *IEEE Transactions on Geoscience and Remote Sensing*, vol. 39, no. 11 pp. 2444-2453, Nov. 2001.

[10] W.J. Blackwell, "Retrieval of Atmospheric Temperature and Moisture Profiles from Hyperspectral Sounding Data Using a Projected Principal Components Transform and a Neural Network," *Proceedings of the 2003 IEEE International Geoscience and Remote Sensing Symposium*, vol. 3, pp. 2078-2081, July 2003.

[11] C.R. Cabrera-Mercader, "Robust Compression of Multispectrtal Remote Sensing Data," Ph.D. thesis, Massachusetts Institute of Technology, Department of Electrical Engineering and Computer Science, 1999.

[12] A.T.C. Chang, L.S. Chiu, and G. Yang, "Diurnal Cycle of Oceanic Precipitation from SSM/I Data," *Monthly Weather Review*, vol. 123, pp. 3371-3380, Nov. 1995.

[13] A.T.C. Chang, L.S. Chiu, C. Kummerow, J. Meng, and T.T. Wilheit, "First Results of the TRMM Microwave Imager (TMI) Monthly Oceanic Rain Rate: Comparison with SSM/I," *Geophysical Research Letters*, vol. 26, pp. 2379-2382, 1999.

[14] F.W. Chen, "Characterization of Clouds in Atmospheric Temperature Profile Retrievals," M. Eng. thesis, Massachusetts Institute of Technology, Department of Electrical Engineering and Computer Science, June 1998.

[15] F.W. Chen and D.H. Staelin, "Millimeter-Wave Observations of Precipitation Using AMSU on the NOAA-15 Satellite," *Proceedings of the 2001 IEEE International Geoscience and Remote Sensing Symposium*, vol. 3, pp. 1044-1045, 9-13 July 2001.

[16] F.W. Chen and D.H. Staelin, "Global Millimeter-Wave Observations of Precipitation Using AMSU on the NOAA-15 Satellite," *Proceedings of the 2002 IEEE International Geoscience and Remote Sensing Symposium*, vol. 1, pp. 460-462, 24-28 June 2002.

[17] F.W. Chen and D.H. Staelin, "AIRS/AMSU/HSB Precipitation Estimates," *IEEE Transactions on Geoscience and Remote Sensing*, vol. 41, no. 2, pp. 410-417, Feb. 2003.

[18] F.W. Chen, A.M. Leckman, and D.H. Staelin, "Satellite Observations of Polar Precipitation Using Aqua," *7th Conference on Polar Meteorology and Oceanography and Joint Symposium on High-Latitude Climate Variations* (American Meteorological Society), May 2003 (preprint).

[19] F.W. Chen, A.M. Leckman, and D.H. Staelin, "Passive Microwave Signatures of Arctic Snowstorms Observed from Satellites," *Proceedings of the 2003 IEEE International Geoscience and Remote Sensing Symposium*, vol. 5, pp. 3139-3141, July 2003.

[20] M.D. Conner and G.W. Petty, "Validation and Intercomparison of SSM/I Rain-Rate Retrieval Methods over the Continental U.S.," *Journal of Applied Meteorology*, vol. 37, no. 7, pp. 679-700, 1998.

[21] A. Dai, F. Giorgi, and K.E. Trenberth, "Observed and Model-Simulated Diurnal Cycles of Precipitation over the Contiguous United States," *Journal of Geophysical Research*, vol. 104, no. D6, pp. 6377-6402, 27 Mar 1999.

[22] D. Deirmendjian, *Electromagnetic Scattering on Spherical Polydispersions*, American Elsivier Publishing Co., New York, NY, 1969.

[23] S. Franquet, "Contribution à l'étude du cycle hydrologique par radiométrie hyperfréquence: algorithmes de restitution (réseaux de neurones) et validation pour la vapeur d'eau (instruments AMSU, SAPHIR) et les précipitations (AMSU, radars au sol BALTRAD)," Ph.D. thesis, École Polytechnique (France), 2003.

[24] A. Fuentes-Loyola, "Precipitation Measurements Using 54- and 183- GHz AMSU Satellite Observations," M.Eng. thesis, Massachusetts Institute of Technology, Department of Electrical Engineering and Computer Science, June 1999.

[25] A.J.T. Gasiewski, "Atmospheric Temperature Sounding and Precipitation Cell Parameter Estimation Using Passive 118-GHz O_2 Observations," Ph.D. thesis, Department of Electrical Engineering and Computer Science, December 1988.

[26] A.J. Gasiewski, "Microwave Radiative Transfer in Hydrometeors," *Atmospheric Remote Sensing by Microwave Radiometry* (edited by M.A. Janssen), John Wiley & Sons, Inc., New York, NY, 1993.

[27] A.J. Gasiewski, D.M. Jackson, J.R. Wang, P.E. Racette, D.S. Zacharias, "Airborne Imaging of Tropospheric Emission at Millimeter and Submillimeter Wavelengths," *Proceedings of the 1994 IEEE International Geoscience and Remote Sensing Symposium*, vol. 2, pp. 663-665, 8-12 Aug. 1994.

[28] T.S. Glickman (ed.), *Glossary of Meteorology*, American Meteorological Society, Boston, MA, 2000.

[29] M.D. Goldberg, D.S. Crosby, and L. Zhou, "The Limb Adjustment of AMSU-A Observations: Methodology and Validation," *Journal of Applied Meteorology*, vol. 40, pp. 70-83, Jan. 2001.

[30] N. Grody, F. Weng, and R. Ferraro, "Application of AMSU for Obtaining Hydrological Parameters," *Microwave Radiometry and Remote Sensing of the Earth's Surface and Atmosphere* (edited by P. Pampaloni and S. Paloscia), pp. 339-351, 2000.

[31] A. Gruber, X. Su, M. Kanamistu, and J. Schemm, "The Comparison of Two Merged Rain Gauge-Satellite Precipitation Datasets," *Bulletin of the American Meteorological Society*, vol. 81, no. 11, Nov. 2000.

[32] M.T. Hagan and M.B. Menhaj, "Training Feedforward Networks with the Marquardt Algorithm," *IEEE Transactions on Neural Networks*, vol. 5, no. 6, pp. 989-993, Nov. 1994.

[33] D.L. Hall and J. Llinas, "An Introduction to Multisensor Data Fusion," *Proceedings of the IEEE*, vol. 85, no. 1, pp. 6-23, January 1997.

[34] S. Haykin, *Neural Networks: A Comprehensive Foundation*, Macmillian College Publishing Co., New York, NY, 1994.

[35] T.J. Hewison and R. Saunders, "Measurements of the AMSU-B Antenna Pattern," *IEEE Transactions on Geoscience and Remote Sensing*, vol. 34, no. 2, pp. 405-412, March 1996.

[36] J.P. Hollinger, "SSM/I Instrument Evaluation," *IEEE Transactions on Geoscience and Remote Sensing*, vol. 28. no. 5, pp. 781-790, Sept. 1990.

[37] J. Houghton, *The Physics of the Atmospheres*, Cambridge University Press, New York, NY, 2002.

[38] R.A. Houze, *Cloud Dynamics*, Academic Press, Inc., New York, NY, 1993.

[39] G. Hufford, "A Model for the Complex Permittivity of Ice at Frequencies Below 1 THz," *International Journal of Infrared and Millimeter Waves*, Vol. 12, No. 7, 1991.

[40] A. Hyvärinen, "Fast and Robust Fixed-Point Algorithms for Independent Component Analysis," *IEEE Transactions on Neural Networks*, vol. 10, no. 3, pp. 626-634, May 1999.

[41] A. Hyvärinen, "Independent Component Analysis: Algorithms and Applications," *Neural Networks*, vol. 13, pp. 411-430, June 2000.

[42] A. Hyvärinen, J. Karhunen, and E. Oja, *Independent Component Analysis*, John Wiley & Sons, Inc., New York, NY, 2001.

[43] J. Ikai and K. Nakamura, "Comparison of Rain Rates over the Ocean Derived from TRMM Microwave Imager and Precipitation Radar," *Journal of Atmospheric and Oceanic Technology*, vol. 20, pp. 1709-1726, Dec. 2003.

[44] I.T. Joliffe, *Principal Component Analysis*, Springer-Verlag New York, Inc., New York, NY, 2002.

[45] T. Kawanishi, T. Sezai, Y. Ito, K. Imaoka, T. Takeshima, Y. Ishido, A. Shibata, M. Miura, H. Inahata, and R.W. Spencer, "The Advanced Microwave Scanning Radiometer for the Earth Observing System (AMSR-E), NASDA's Contribution to the EOS for Global Energy and Water Cycle Studies," *IEEE Transactions on Geoscience and Remote Sensing*, vol. 41, no. 2, pp. 184-194, Feb. 2003.

[46] B. Kedem, H. Pavlopoulos, X. Guan, D.A. Short, "A Probability Distribution Model for Rain Rate," *Journal of Applied Meteorology*, vol. 33, no. 12, pp. 1486-1493, Dec. 1994.

[47] M. Kim, G. Skofronick-Jackson, J.A. Weinman, and D. Chang, "Spaceborne Passive Microwave Measurement of Snowfall over Land," *Proceedings of the 2003 IEEE International Geoscience and Remote Sensing Symposium*, vol. 5, pp. 3163-3165, July 2003.

[48] C. Kongoli, P. Pellegrino, R.R. Ferraro, N.C. Grody, and H. Meng, "A New Snowfall Detection Algorithm over Land Using Measurements from the Advanced Microwave Sounding Unit (AMSU)," *Geophysical Research Letters*, vol. 30, no. 14, 1756, doi:10.1029/2003GL017177, 2003.

[49] C. Kummerow and L. Giglio, "A Passive Microwave Technique for Estimating Rainfall and Vertical Structure Information from Space. Part I: Algorithm Description," *Journal of Applied Meteorology*, vol. 33, pp. 3-18, Jan. 1994.

[50] C. Kummerow, W. Barnes, T. Kozu, J. Shiue, and J. Simpson, "The Tropical Rainfall Measuring Mission (TRMM) Sensor Package," *Journal of Atmospheric and Oceanic Technology*, vol. 15, pp. 809-817, June 1998.

[51] B.H. Lambrigtsen, "Calibration of the AIRS Microwave Instruments," *IEEE Transactions on Geoscience and Remote Sensing*, vol. 41, no. 2, pp. 369-378, Feb. 2003.

[52] J. Lee, "Blind Noise Estimation and Compensation for Improved Characterization of Multivariate Processes," Ph.D. thesis, Massachusetts Institute of Technology, Department of Electrical Engineering and Computer Science, March 2000.

[53] J. Lee and D.H. Staelin, "Iterative Signal-Order and Noise Estimation for Multivariate Data," *IEE Electronics Letters*, vol. 37, no. 2, pp. 134-135, 18 January 2001.

[54] R.V. Leslie, W.J. Blackwell, P.W. Rosenkranz, and D.H. Staelin, "183-GHz and 425-GHz Passive Microwave Sounders on the NPOESS Aircraft Sounder Testbed-Microwave (NAST-M)," *Proceedings of the 2003 IEEE Int'l Geoscience and Remote Sensing Symp.*, Vol. 1, pp. 506-508, July 2003.

[55] R.V. Leslie, J.A. Loparo, P.W. Rosenkranz, and D.H. Staelin, "Cloud and Precipitation Observations with the NPOESS Aircraft Sounder Testbed-Microwave (NAST-M) Spectrometer Suite at 54/118/183/425 GHz," *Proc. 2003 IEEE Int'l Geoscience and Remote Sensing Symp.*, Vol. 2, pp. 1212-1214, July 2003.

[56] R.V. Leslie, et al., "NPOESS Aircraft Sounder Testbed-Microwave (NAST-M) Observations of Clouds and Precipitation at 54, 118, 183, and 425 GHz," *IEEE Transactions on Geoscience and Remote Sensing*, submitted.

[57] R.V. Leslie, "Geophysical Parameter Estimation at 54/118/183/425 GHz," Sc.D. thesis, Massachusetts Institute of Technology, Department of Electrical Engineering and Computer Science, to be completed in 2004.

[58] R.P. Lippmann, "An Introduction to Computing with Neural Nets," *IEEE Acoustics, Speech, and Signal Processing Magazine*, vol. 4, no. 2, pp. 4-22, April 1987.

[59] J.A. Loparo, "Storm-Wide Precipitation Retrievals," S.M. thesis, Massachusetts Institute of Technology, Department of Electrical Engineering and Computer Science, to be completed in June 2004.

[60] D.W. Marquardt, "An Algorithm for Least-Squares Estimation of Nonlinear Parameters," *Journal of the Society for Industrial and Applied Mathematics*, vol. 11, no. 2, pp, 431-441, June 1963.

[61] T. Mo, "AMSU-A Antenna Pattern Corrections," *IEEE Transactions on Geoscience and Remote Sensing*, vol. 37, no. 1, pp. 103-112, Jan. 1999.

[62] A. Mueller, "Iterative Blind Seperation of Gaussian Data of Unknown Order," M.Eng. thesis, Massachusetts Institute of Technology, Department of Electrical Engineering and Computer, June 2003.

[63] A. Mueller and D.H. Staelin, "Blind Separation of Noisy Gaussian Multivariate Signals," *IEEE Transactions on Signal Processing*, submitted.

[64] D. Nguyen and B. Widrow, "Improving the Learning Speed of 2-Layer Neural Networks by Choosing Initial Values of the Adaptive Weights," Proceedings of the International Joint Conference on Neural Networks, vol. 3, pp. 21-26, 1990.

[65] *Neural Network Toolbox User's Guide*, The MathWorks, Inc., 1998.

[66] C.L. Parkinson, "Aqua: An Earth-Observing Satellite Mission to Examine Water and Other Climate Variables," *IEEE Transactions on Geoscience and Remote Sensing*, vol. 41, no. 2, pp. 173-183, Feb. 2003.

[67] C. Pohl, and J.L. van Genderen, "Multisensor Image Fusion in Remote Sensing: Concepts, Methods, and Application," *International Journal of Remote Sensing*, vol. 19, no. 5, pp. 823-854, 1998.

[68] P.W. Rosenkranz, "Inversion of Data from Diffraction-Limited Multiwavelength Remote Sensors, 1. Linear Case," *Radio Science*, vol. 13, no. 6, pp. 1003-1010, Nov.-Dec. 1978.

[69] P.W. Rosenkranz, "Inversion of Data from Diffraction-Limited Multiwavelength Remote Sensors, 2. Nonlinear Dependence of Observables on the Geophysical Parameters," *Radio Science*, vol. 17, no. 1, pp. 245-256, Jan.-Feb. 1982.

[70] P.W. Rosenkranz, "Inversion of Data from Diffraction-Limited Multiwavelength Remote Sensors, 3. Scanning Multichannel Microwave Radiometer Data," *Radio Science*, vol. 17, no. 1, pp. 257-267, Jan.-Feb. 1982.

[71] P.W. Rosenkranz, "Improved Rapid Transmittance Algorithm for Microwave Sounding Channels," *Proceedings of the 1998 IEEE International Geoscience and Remote Sensing Symposium*, vol. 2, pp. 728-730, July 1998.

[72] P.W. Rosenkranz, "Retrieval of Temperature of Moisture Profiles From AMSU-A and AMSU-B Measurements," *IEEE Transactions on Geoscience and Remote Sensing*, vol. 39, no. 11, pp. 2429-2435, Nov. 2001.

[73] P.W. Rosenkranz, "Rapid Radiative Transfer Model for AMSU/HSB Channels," *IEEE Transactions on Geoscience and Remote Sensing*, vol. 41, no. 2, pp. 362-368, Feb. 2003.

[74] P.W. Rosenkranz, "Cloud Liquid Water Retrievals from Aqua AMSU/HSB," *Proceedings of the 2003 IEEE International Geoscience and Remote Sensing Symposium*, vol. 2, pp. 1142-1144, July 2003.

[75] L. Shi, "Retrieval of Atmospheric Temperature Profiles from AMSU-A Measurement Using a Neural Network Approach," *Journal of Atmospheric and Oceanic Technology*, vol. 18, pp. 340-347, March 2001.

[76] J.C. Shiue, "The Advanced Technology Microwave Sounder, a New Atmospheric Temperature and Humidity Sounder for Operational Polar-Orbiting Weather Satellites," *Proceedings of the SPIE*, vol. 4540, pp. 159-165, 2001.

[77] G.M. Skofronick-Jackson, J.A. Weinman, and D. Chang, "Observation of Snowfall over Land by Microwave Radiometry from Space," *Proceedings of the 2002 IEEE International Geoscience and Remote Sensing Symposium*, vol. 3, pp. 1866-1868, June 2002.

[78] G.M. Skofronick-Jackson, M. Kim, J.A. Weinman, and D. Chang, "A Physical Model to Determine Snowfall over Land by Microwave Radiometry," *IEEE Transactions on Geoscience and Remote Sensing*, vol. 42, no. 5, pp. 1047-1058, May 2004.

[79] R.W. Spencer, "A Satellite Passive 37-GHz Scattering-based Method for Measuring Oceanic Rain Rates," *Journal of Climate and Applied Meteorology*, vol. 25, no. 6, pp. 754-766, June 1986.

[80] M.S. Spina, M.J. Schwartz, D.H. Staelin, and A.J. Gasiewski, "Application of Multilayer Feedforward Neural Networks to Precipitation Cell-Top Altitude Estimation," *IEEE Transactions on Geoscience and Remote Sensing*, vol. 36, no. 1, pp. 154-162, Jan. 1998.

[81] D.H. Staelin, F.W. Chen, A. Fuentes, "Precipitation Measurements Using 183-GHz AMSU Satellite Observations," *Proceedings of the 1999 IEEE International Geoscience and Remote Sensing Symposium*, vol. 4 , pp. 2069-2071, 28 June-2 July 1999.

[82] D.H. Staelin and F.W. Chen, "Precipitation Observations Near 54 and 183 GHz Using the NOAA-15 Satellite," *IEEE Transactions on Geoscience and Remote Sensing*, vol. 38, no. 5, pp. 2322-2332, Sept. 2000.

[83] G. Strang, *Introduction to Linear Algebra*, Wellesley-Cambridge Press, Wellesley, MA, 1993.

[84] D. Tsintikidis, J.L. Haferman, E.N. Anagnostou, W.F. Krajewski, and T.F. Smith, "A Neural Network Approach to Estimating Rainfall from Spaceborne

Microwave Data," *IEEE Transactions on Geoscience and Remote Sensing*, vol. 35, no. 5, pp. 1079-1093, Sept. 1997.

[85] Tropical Rainfall Measuring Mission, http://trmm.gsfc.nasa.gov/

[86] V.J.D. Tsai, "Frequency-Based Fusion of Multiresolution Images," *Proceedings of the 2003 IEEE International Geoscience and Remote Sensing Symposium*, vol. 6, pp. 3665-3667, July 2003.

[87] F.T. Ulaby, R.K. Moore, and A.K. Fung, *Microwave Remote Sensing: Active and Passive*, Addison-Wesley Pub. Co., Reading, MA, 1981.

[88] L. Wald, "Some Terms of Reference in Data Fusion," *IEEE Transactions on Geoscience and Remote Sensing*, vol. 37, no. 3, pp. 1190-1193, May 1999.

[89] F. Weng, L. Zhao, R.R. Ferraro, G. Poe, X. Li, and N.C. Grody, "Advanced Microwave Souding Unit Cloud and Precipitation Algorithms," *Radio Science*, vol. 38, no. 4, 8068, doi:10.1029/2002RS002679, 2003.

[90] F.J. Wentz and R.W. Spencer, "SSM/I Rain Retrievals within a Unified All-Weather Ocean Algorithm," *Journal of the Atmospheric Sciences*, vol. 55, no. 9, pp. 1613-1627, May 1998.

[91] T.T. Wilheit, A.T.C. Chang, M.S.V. Rao, E.B. Rodgers, and J.S. Theon, "A Satellite Technique for Quantitatively Mapping Rainfall Rates over the Oceans," *Journal of Applied Meteorology*, vol. 16, no. 5, pp. 551-560, May 1977.

[92] T. Wilheit, C.D. Kummerow, and R. Ferraro, "Rainfall Algorithms for AMSR-E," *IEEE Transactions on Geoscience and Remote Sensing*, vol. 41, no. 2, pp. 204-213, Feb. 2003.